Fiber crystal growth of cerium doped calcium scandate, strontium yttrium oxide, and tristrontium silicate

vorgelegt von
Diplom-Mineraloge
Jan Philippen
Hilden

von der Fakultät II - Mathematik und Naturwissenschaften
der Technischen Universität Berlin
zur Erlangung des akademischen Grades
Doktor der Naturwissenschaften
Dr.rer.nat.

genehmigte Dissertation

Promotionsausschuss

Vorsitzender: Prof. Dr. Peter Strasser
Berichter: Prof. Dr. Martin Lerch
Berichter: PD Dr. habil. Detlef Klimm

Tag der wissenschaftlichen Aussprache: 24.09.2013

Berlin 2013

D83

Abstract

An experimental approach to three new materials crystallized with laser-heated pedestal growth and micro-pulling-down method is given. Calcium scandate, strontium yttrium oxide, and tristrontium silicate are related high-melting oxides, which have been investigated as light phosphors in the last decade. In this work cerium doped single crystalline fibers are fabricated. Their luminescence properties and possible application as laser materials are investigated. Differences between both fiber growth techniques are revealed with respect to the mass flow and steady state conditions. Phase relations are determined by thermal analysis and X-ray diffraction. They provide boundary conditions for the growth experiments and reveal the hitherto unknown phase system calcium oxide–scandium oxide. Thermodynamic equilibrium calculation of the growth conditions gives further information on suitable growth parameters. Calculated fugacities of evaporating species are confirmed by high-temperature mass spectrometry, inductively coupled plasma optical emission spectrometry, and energy-dispersive X-ray spectroscopy. The evaporation can be minimized by a reasonable choice of growth parameters and atmosphere. Moreover, the atmosphere influences the cerium valence. This dependency is thermodynamically calculated and experimentally demonstrated by optical spectroscopy. Fibers crystallized in nitrogen atmosphere show the best results with respect to the crystal quality and cerium luminescence. Calcium scandate, doped with trivalent cerium, is promising for laser applications. Steady state conditions, influenced by segregation and evaporation, are focused with respect to the different materials and growth techniques. The micro-pulling-down method is suitable for crystallization of tristrontium silicate. Calcium scandate will show superior quality, if crystallized with the laser-heated pedestal growth technique. Transmission electron microscopy, optical spectroscopy, and high-resolution X-ray diffraction confirm an assumed model for the cerium incorporation into calcium scandate. Single crystal structure determination of tristrontium silicate is performed. During laser-heated pedestal growth, the steady state is limited by oscillatory thermocapillary convection. Preliminary numerical investigation reveals a possible correlation of evaporation and oscillatory thermocapillary convection.

Contents

Chapter 1

Introduction

1.1 An approach to new materials

This work is an approach to introduce three new materials, namely cerium doped calcium scandate ($CaSc_2O_4$:Ce), strontium yttrium oxide (SrY_2O_4:Ce), and tristrontium silicate (Sr_3SiO_5:Ce). In the following the abbreviations CS2:Ce, SY2:Ce, and TSS:Ce are used synonymously for cerium doped calcium scandate, strontium yttrium oxide, and tristrontium silicate. Calcium scandate will be presented as a potential candidate for solid-state laser applications. Two related materials, the isostructural strontium yttrium oxide and tetragonal tristrontium silicate, are fabricated as reference materials. All three oxides have melting points above 2100 °C and similar luminescence properties. Because of the high melting points evaporation will be a critical phenomenon to be controlled. The origin of this work is motivated by two developments: the research of new crystalline laser materials in the wavelength range of green light and the investigation of phosphors for light-emitting diodes (LEDs).

In collaboration with the Institute of Laser Physics (ILP, University of Hamburg, Germany) the material calcium scandate was chosen for crystal growth investigation. In principle, a cerium doped calcium scandate laser is possible. This is explained in Matthias Fechners' thesis (ILP) [39]. Solid state laser materials have to fulfill several requirements, such as a high thermal conductivity, a high gain coefficient, a high emission cross section, a sufficient hardness, and high transparency in the laser wavelength region [45, 70]. Advantages of solid state lasers are high density of laser-active centers ($\approx 10^{19}\,\mathrm{cm}^{-3}$), optical pumping with arc lamps or laser or LED, high pulse power, and long-term durability [37]. Although more than 575 single crystals for solid state laser applications have been investigated [70], a green solid state laser with a high efficiency and power output is still desirable [90]. Stimulated emission in the green light region can be generated in cerium doped YAG ($Y_3Al_5O_{12}$), however, strong excited state absorption (ESA) excludes suitable laser output. As of this writing, only cerium doped fluorides with laser in the UV wavelength region are established [17]. Fechner found out that in cerium doped calcium scandate ESA is significantly reduced, and therefore, laser radiation possible [39]. The second motivation is the light phosphor investigation for color conversion in LEDs. These phosphors are required to fabricate white LEDs with a high coloring index, since gallium nitride based blue LEDs have been developed [94]. Two material systems being used for LEDs are indium gallium nitride (In,Ga)N and aluminum

indium gallium phosphide (AlInGaP). Both of these semiconductor systems have lower efficiencies in the green, yellow, and amber spectral ranges than in the blue spectral range [109]. Therefore, light phosphors that absorb blue light and emit in the longer wavelength region are required for white LEDs. Setlur gives an overview of the modern phosphor research for LED-based solid state lighting [109]. All three materials in this work have been in the scientific scope of phosphor research: Calcium scandate as a green light phosphor [113], europium doped strontium yttrium oxide as red light phosphor [124], and cerium doped tristrontium silicate as yellow light phosphor [97].

Jia et al. demonstrated the significance of crystal growth to the investigation of light phosphors [67]. We want to fabricate high-quality single crystalline fibers (SCFs). Therefore, a suitable growth technique is required. The laser-heated pedestal growth method (LHPG), based on the work of Eickhoff and Gürs [38], fits the requirements for cerium doped calcium scandate. The crucible-free float zone, the possibility to adjust atmospheres of different chemical nature, the rapid growth rates and the Marangoni dominated convection qualify the LHPG method for crystal growth of calcium scandate. To point out these advantages and to discuss drawbacks, the micro-pulling-down method (mPD) is used as a reference technique. This method was developed at Fukuda Laboratory (Tohoku University, Japan) in 1992 [123]. Precise information about the phase relations of $CaSc_2O_4$:Ce are important for the understanding and control of the crystallization process. Therefore, the phase system CaO-Sc_2O_3 that has not been published yet is investigated. Phase relations will be used for installing suitable crystal growth conditions. The phase systems SrO-Sc_2O_3 and SrO-SiO_2 have already been investigated [118, 63]. The investigation of the phase relations will be supported by thermodynamic equilibrium calculation. Thus, phenomena affecting the crystal growth process can be predicted and controlled. One of the main challenges will be the incorporation of trivalent cerium into the crystal hosts. A suitable choice of the growth atmosphere and growth parameters has to be figured out. Strontium yttrium oxide and calcium scandate crystallize in $CaFe_2O_4$ structure [92]. Tristrontium silicate is tetragonal [26]. The doping mechanism and the influence of the dopant on the host lattice will be a focus of this work. Crystallized fibers will be investigated regarding their homogeneity, crystal quality on macroscopic and atomic scale, composition, and spectroscopic properties.

1.2 Structure of the work

This work might be useful for those who are interested in the fabrication of fiber crystals with LHPG and mPD techniques. To anyone who intends to investigate either of the three materials calcium scandate, strontium yttrium oxide, and tristrontium silicate, this work might provide useful information. Finally, anyone who is investigating new and uncommon materials and or using uncommon crystal growth methods might find some advice within this work. Each of the following chapters include a short introduction that explains content and purpose of the chapter.

This work summarizes experimental research. Therefore, the theoretical background, chapter 2, is kept as concise as possible. Information on fiber crystal growth and thermodynamics are given to understand the purpose of this work. The laser and luminescence materials section introduces calcium scandate, strontium yttrium

oxide, tristrontium silicate, and cerium as a dopant. The experimental setup is explained in chapter 3 with focus on calculation, conditions, preparation, growth setup, and growth parameters. The characterization methods are introduced. I omit comprehensive explanations of the methods and refer to further information in the relevant literature. The focus is laid on boundary conditions. Results and discussion are presented in chapters 4 and 5. In chapter 4, the investigation of the phase relations using high-temperature thermal analysis (DTA, DSC, TG) and X-ray diffraction (XRD) are discussed. Chapter 5 is based upon chapter 4 and includes all experimental work, and thermodynamic calculations, concerning the fiber crystal growth. The calculation of the growth conditions (with Factsage™) and high-temperature mass spectrometry (HTMS) provide information for growth parameters optimization. The phase analysis of SCFs is performed using XRD, scanning electron microscopy (SEM). In combination with elemental analysis via energy-dispersive X-ray spectroscopy (EDX) and inductively coupled plasma optical emission spectrometry (ICP-OES) the composition shift and segregation effects will be explained. The crystal quality is analyzed using high-resolution XRD, transmission electron microscopy (TEM). Additionally, TEM-EDX and single crystal structure refinement provide information about the doping process. Laser fluorescence and their lifetime determination in combination with transmission and absorption measurements will open a discussion on the application as potential laser materials. The last chapters will conclude this work (chapter 6) and critically discuss the outcome with reference to future work (chapter 7). A part of this work is published in [101].

Chapter 2

Background and materials

This section gives a short introduction into the fiber crystal growth and the crystallization process (2.1). The differences between laser-heated pedestal growth and micro-pulling-down are pointed out with respect to fundamentals, application and steady state conditions. The second part deals with thermodynamics and equilibrium conditions (2.2). These fundamentals are important for the investigation of the phase system CaO-Sc_2O_3 in chapter 4. Introduction into the investigated materials and into cerium-based luminescence and laser materials (section 2.3) integrate the main issues of this work into a materials research concept.

2.1 Fiber crystal growth

Fabrication and investigation of single crystalline fibers (SCF) became more important in the past decades. This development is associated with research in laser and luminescence materials, scintillators, and semiconductors. With a typical diameter range from μm to mm they offer unique properties because of their nearly one-dimensional geometry [41]. Major contribution to the field of fiber crystal research and especially the development of the micro-pulling-down method was made by Fukuda, Rudolph, and Uda [47]. The concept of modern laser-heated crystal growth was made by Fejer et al. and Feigelson [42, 40]. The variety in growing shaped fiber crystals is demonstrated in [34, 105, 46]. Fiber crystal growth methods are fast and cost-efficient. Only small amounts are required for growth experiments. Therefore, they are suitable for the investigation of new and uncommon materials. Because fibers can remove heat very efficiently (short distance between the pumped region and the surrounding metal coolant), they are suitable in experimental laser setups. It is possible to use as-grown SCFs for laser experiments [64].

Although both, LHPG and mPD, are fiber growth techniques, they differ in one fundamental aspect: Whereas the micro-pulling-down technique is a direct-from-the-melt crystallization that can be compared to CZ growth, the LHPG is a crucible-free zone leveling process. This difference is striking, because segregation and evaporation directly affect the crystallization process. Section 2.1.5 compares both techniques with respect to the growth experiments in this work. Section 5.5 discusses the different mass transport and the resulting differences in fiber quality and properties.

2.1.1 Crystallization and crystal defects

This work solely deals with crystallization from the liquid (melt and solution). Is is noteworthy that also crystallization from the gas phase (e.g. metal organic vapor phase epitaxy) and from the solid state (e.g. recrystallization) are conceived within the field of crystal growth science. Crystallization is a first-order phase transformation into the solid state from the solid, liquid or vapor state [27]. In perfect thermodynamic equilibrium no crystallization can occur, because the free energy is at a minimum. As a driving force for crystallization a disturbance is required that shifts the system slightly apart the equilibrium state. This could be achieved by change in temperature, pressure, strain, electrochemical potential, electric or magnetic field. The process can be parted in three fundamental steps [27]: 1. The achievement of supercooling or supersaturation, 2. Nucleation, 3. Nuclei growth.

Every crystal has characteristic defects that arise from the growth method, the growth parameters, and the crystallized material itself. To conceive the variety of crystal defects, it is useful to define an ideal crystal. The latter can be considered as homogeneously condensed matter in perfect crystal structure [74]. Because of deviations from a perfect crystal structure (that arise from thermodynamics) such an ideal crystal cannot exist [16]. For instance, every surface of a crystal is a disorder of a perfect crystal structure. Crystal defects can be summarized as [16]: 1. Internal stress, phonons and other defects that do not substantially disturb the lattice. 2. point defects, solid solutions, inhomogeneities, clusters, inclusions, dislocations, planar defects (e.g. stacking faults), grain boundaries, and interfaces.

2.1.2 Zone melting and segregation

Modern zone melting has its origin in the zone refining process, developed by Pfann at Bell Laboratories [99]. State-of-the-art optical floating zone technique (OFZ) is used for a variety of materials including metals, oxides, and semiconductors [27]. Especially the crystallization of incongruently melting materials and high melting oxides with evaporating species can be undertaken by this technique. The basic concepts of optical floating zone and laser-heated pedestal growth techniques differ in the heating system. While an optical light source (e.g. halogen lamps) is used to establish a melt zone in OFZ, the melt zone in LHPG furnace is heated with an infrared laser. In both techniques, two rods are contacted to each other at the focal point of the heating source. The upper seed rod either holds a seed crystal or a polycrystalline ceramic of the starting material. The lower feed rod holds a ceramic material with the same composition.

With equal translation rates of the rods and, if evaporation can be neglected, the Pfann relation describes the segregation of a component in the crystal [100]:

$$C_{s,i}(z) = C_{0,i} \cdot \left[1 - (1 - k_{\text{eff}}) \exp\left(-\frac{k_{\text{eff}} \cdot z}{l}\right)\right] \tag{2.1}$$

with $C_{s,i}(z)$ and $C_{0,i}$ as concentration of the dopant i in the growing crystal and the feed rod, z the crystal axis, l the zone length and k_{eff} the effective distribution coefficient. If there is only minor evaporation of components, the melt zone will be enriched with or depleted of the dopant for $k_{\text{eff}} < 1$ or $k_{\text{eff}} > 1$, respectively, until $C_{s,i}(z)$ equals $C_{0,i}$ (ideal steady state). If there is evaporation of the dopant from the melt zone, $C_{s,i}(z) < C_{0,i}$ (case $k_{\text{eff}} < 1$) for all z. However, $C_{s,i}(z)$ will reach a

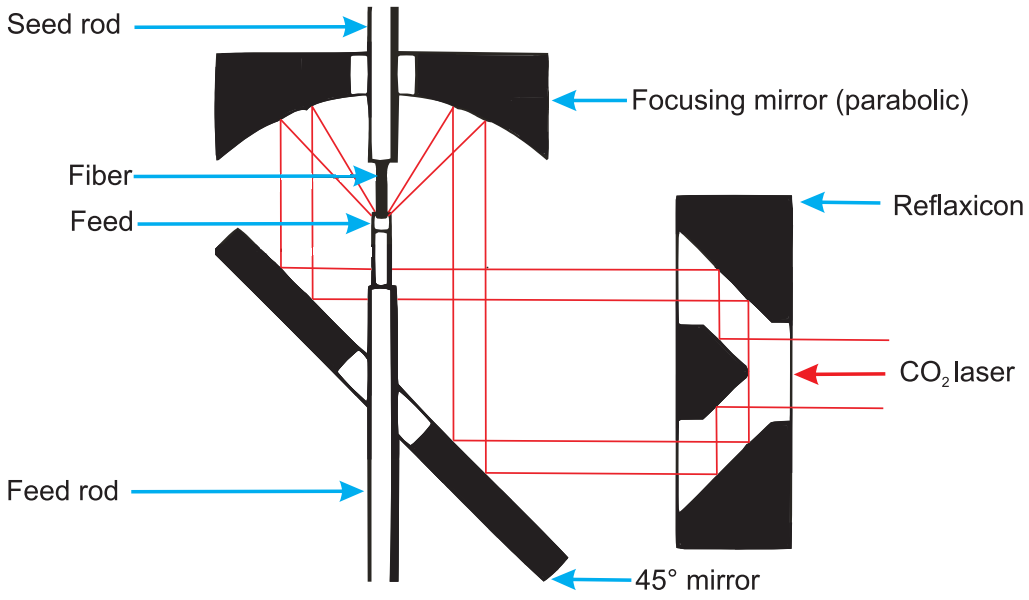

Figure 2.1: Schematic setup of the LHPG technique (after [42]).

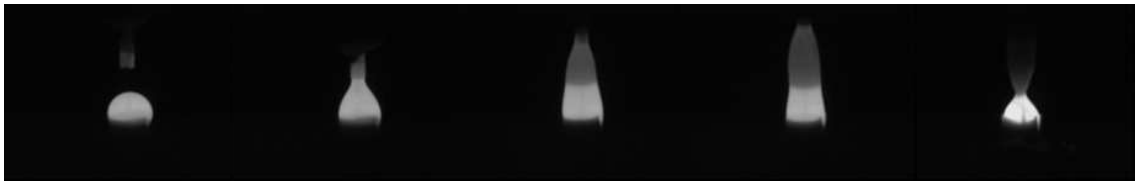

Figure 2.2: Different stages of the LHPG crystallization process (from left to the right): pre-heating, seeding, diameter alignment, steady state growth, and separating.

constant value in quasi-steady state. The discussion of the mass flows in LHPG and mPD growth (section 5.5.4) gives a concept for the understanding of steady state in both crystal growth techniques.

2.1.3 Laser-heated pedestal growth

This section describes the general concept and theoretical background of the LHPG process. The experimental setup, parameters, and characteristics of the system used in this work are given in section 3.2.2 on page 32. Typical for LHPG growth is a laser beam size (in the focal point) in the range of the fiber diameter [40]. Because of the extremely steep temperature gradients (several 10^3 K/cm in axial direction [7]) rapid growth rates can be established (several mm/min). Analysis of the temperature field and numerical investigation (3.2.2, 5.7) will show that the temperature gradient exceeds 4000 K/cm for the investigated growth setup. Note, that the gradient reaches these high values only in a range of a few mm. By using rapid crystallization rates incongruent melting compounds can be crystallized [43] as well as metastable phases [116]. Because of the small volume of the melt the Marangoni convection is the dominant driving force for convection [108]. Through rapid growth rates and fast Marangoni convection high dopant concentrations can be achieved. In addition, small diameter SCFs will usually contain fewer defects if

compared to bulk material [41]. An important challenge is the control of diameter or dopant fluctuations that can be minimized by careful control of temperature, aspect ratio (melt height/fiber diameter), translation rates, feed preparation, and fiber orientation [40].

The basic concept of the LHPG technique is presented in figure 2.1: A CO_2 laser (IR, 10.6 μm) produces a primary beam with a circular cross section. The primary beam is guided through a ZnSe window that expands the beam size (not shown here). A set of two conical mirrors (reflaxicon) transforms the extended beam into a cylindrical shell. The beam is guided to a parabolic mirror (focusing mirror) and focused. In its center the focusing mirror has a hole to avoid mirror degeneration by evaporating species. The feed rod is translated into the focal point of the laser. The different stages of the crystallization process are shown in figure 2.2: The ceramic feed rod of the material that will be crystallized is heated up to the melting point (pre-heating). A spherical melt droplet is generated at the top of the feed rod. Its shape depends on the surface tension, viscosity, and density of the material. With a slow velocity the seed rod is translated into the focal point and contacted with the (static) feed rod (seeding). Immediately after the seeding both rods are moved in upward direction. By adjusting different translation rates, the diameter of the crystallizing fiber can be altered (diameter alignment). At the end of the crystallization process the feed rod is stopped and the fiber is pulled out of the melt zone (separating).

Fundamentals

The dimensional stability of a growing fiber requires that the zone length and melt volume are kept constant [40]. Under the assumption that evaporation and segregation influences are minor, the fiber radius of a growing fiber is:

$$r_{\mathrm{scf}} = r_{\mathrm{feed}} \sqrt{\frac{\rho_{\mathrm{feed}} \upsilon_{\mathrm{feed}}}{\rho_{\mathrm{scf}} \upsilon_{\mathrm{scf}}}} \tag{2.2}$$

where r_{scf}, ρ_{scf}, υ_{scf}, r_{feed}, ρ_{feed}, υ_{feed} are radius, density, and pulling rate of the crystallizing fiber and ceramic feed rod, respectively (the density of the ceramic depends on the preparation method, section 3.2.1) [27]. The stability of the molten zone also depends on a steady state heat flow at the solid-liquid interface [47]:

$$Q_{\mathrm{scf}} = Q_{\mathrm{f}} + Q_{\mathrm{m}} = A \kappa_{\mathrm{scf}} (\delta T / \delta z)_{\mathrm{scf}} = \text{const.}, \tag{2.3}$$

where Q_{scf} is the heat flux into the crystal fiber away from the growth interface, Q_{f} the latent heat of crystallization, Q_{m} is the heat flux from the melt toward the interface, A is the interface area, κ_{scf} is the thermal conductivity of the fiber material, and $(\delta T/\delta z)_{\mathrm{scf}}$ the temperature gradient in the growing fiber. If both equations are fulfilled, the fiber will grow with constant meniscus angle ϕ=ϕ_0 (ϕ_0: growth angle). In this case, steady state is established with respect to the dimensional stability. Deviations, i.e. perturbations in zone length or volume that arise from evaporation or oscillation lead to diameter variations [5]:

$$\delta r_{\mathrm{scf}} / \delta t = \upsilon_{\mathrm{scf}} \tan(\phi - \phi_0) \neq 0. \tag{2.4}$$

A two-dimensional simulation of the heat transfer and interface shape for YAG has been done by Chen [21, 22]. Through modeling of the stream equation, equation

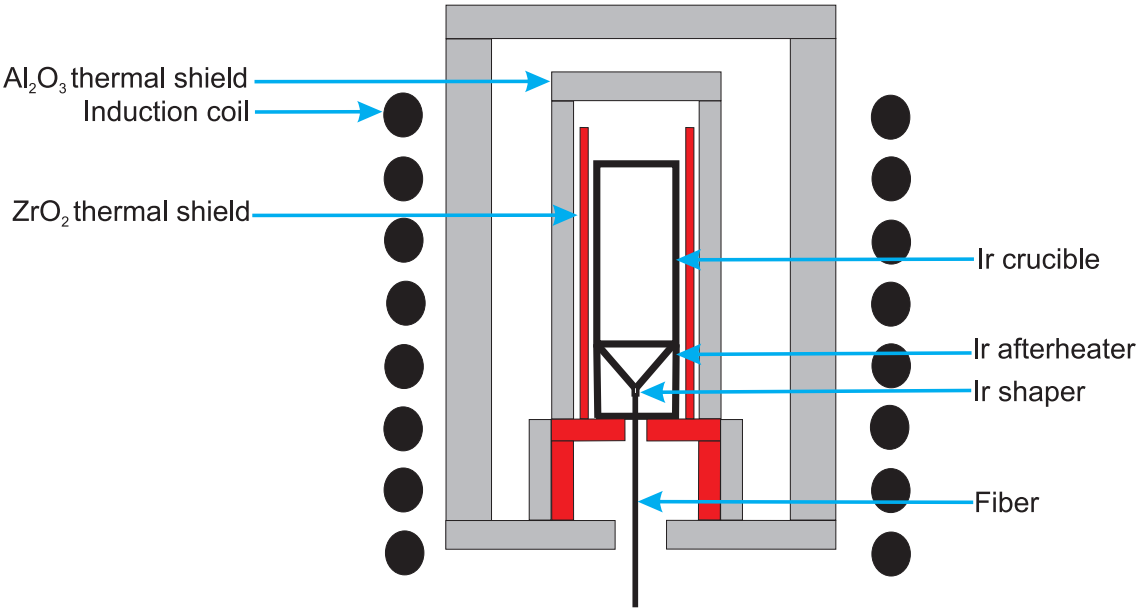

Figure 2.3: Schematic sketch of the mPD setup (after [47]).

Figure 2.4: Different stages of the mPD crystallization process (from left to the right): pre-heating, seeding, diameter alignment, and steady state growth.

of motion, energy equation and mass-transfer equation (adjusted for LHPG setup) Chen calculated the interface and streams for this material. A theoretical model for the dopant incorporation of titanium into a single crystal Al_2O_3 fiber is given in [111]. This model regards the loss of dopant by evaporation. By adapting an evaporation constant τ_{ev} (time in which the dopant concentration in the melt decreases by the factor e^{-1}) the dopant distribution that is affected by segregation and evaporation can be predicted. The discussion of the composition shift and segregation (section 5.5) will show that this model cannot be used for the materials that are discussed in work. The evaporation of the main components and dependency of the fugacities from the composition would demand a more complex model that is yet desirable.

2.1.4 Micro-pulling-down method

Since 1992, the application of SCF growth by the micro-pulling-down method has been developed [47]. mPD was introduced by Yoon and Fukuda in 1994 [123], who described the crystallization of lithium niobate, $LiNbO_3$, using this new technique. mPD is originated in the inverted Stepanov technique for drawing silicon sheets from non-wetting silica [47]. The mPD setup is depicted in figure 2.3. This setup was used for all mPD growth experiments described in this work: An iridium crucible with a crystal shaper at the bottom contains the feed material. The shaper with its

	LHPG	mPD
Fiber radius	μm-mm	μm-mm
Fiber length	Limited by feed size	Limited by melt volume
T maximum	Limited by laser power	Limited by crucible
Axial T gradient	Up to 10^4 K/cm	Up to 10^3 K/cm
Radial T gradient	Up to 10^2 K/cm	Up to 10^2 K/cm
Crystallization rate	several mm/min	several mm/min
Atmosphere	Limited by mirror	Limited by crucible
Interfaces	Two	One
Steady state	Limited by evaporation	Limited by segregation

Table 2.1: Comparison between LHPG and mPD techniques with respect to the growth setup that has been used within this work. A general comparison is presented by Lebbou et al. in [47]. The parameters of the growth conditions are given in section 3.2.2.

0.5 mm orifice is surrounded by an iridium afterheater. ZrO_2 and Al_2O_3 thermal shields protect the induction coil. The water cooled copper coil, connected to a RF generator, (inductively) heats up the crucible until the feed is fully melted and a liquid droplet forms at the orifice of the shaper (2.4). With an (oriented) seed crystal or iridium wire the melt droplet is connected (seeding). By slowly increasing the downwards translation rate of the seed rod and temperature control the fiber diameter can be aligned. In steady state conditions a SFC can be pulled from the crucible throughout the shaper.

The fundamentals of growth dynamics of the mPD method are presented by Uda in et al. [47]. Within this work the micro-pulling-down technique is used as reference growth setup (to the LHPG). In contrast to the LHPG method, during the mPD crystallization the whole feed material is liquid. This fact causes the main differences between LHPG and mPD, as described in the next section.

2.1.5 LHPG vs. mPD

The major difference between LHPG and mPD is caused by the interaction between feed material, liquid phase and crystallized phase. Whereas in LHPG growth only a small fraction of the material is liquid (melt zone), during mPD crystallization all feed material is liquid. Therefore, a comparison is not only a crucible-free versus crucible technique, but rather a zone leveling versus pulling from the melt. In other words, despite of the crystal size, LHPG and floating zone (FZ) technique are more similar to each other. On the other hand, mPD can be compared to a reverse Czochralski (CZ) or inverted Stepanov growth method. The fiber radius (table 2.1) for LHPG SCFs depends on the seed and feed rod translation rates. If strong evaporation occurs, it also depends on the induced laser power. In mPD growth the fiber diameter is a function of the melt meniscus and the pulling rate. If the melt is overheated above the melting point, the surface tension of the material is lowered. This dependency is valid for most materials. As a result, the melt meniscus at the bottom of the crucible will increase in height and diameter. The fiber length is limited by the ceramic feed size (LHPG) and the melt reservoir (mPD). Obviously, both systems are limited by the translation system. In principle, the maximum temperature that can be used in laser-heated pedestal growth is limited

only by the laser power. However, possible degeneration of the mirror surfaces through a formation of reactive gaseous species (e.g. NO_x) must be considered. The Iridium crucible (melting point $\approx$ 2440°) sets the limitation for mPD growth. If reactive compounds (e.g. alkaline earth metal ion containing oxides) are melted, the temperature must remain considerably below the melting point of Iridium. A simplified overview about the axial and radial temperature gradients points out that the gradients in LHPG are about one order of magnitude higher [40, 47]. It is noteworthy that the temperature gradients across the crystal axes are non-linear. The values given in the table are only valid within the region of the melt zone that is typically only a few mm in size. Because of the gradients slightly higher crystallization rates can be established in LHPG growth. The only interface in mPD growth is the crystallization front between the SCF and the melt meniscus. In LHPG two interfaces separate the melt zone from the feed rod and the SCF, respectively.

Capillary stability

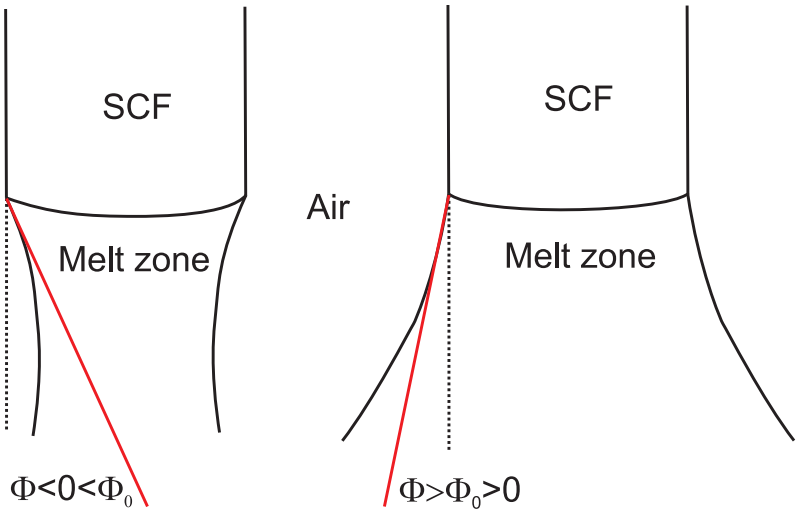

Figure 2.5: Schematic drawing of the solid-liquid-vapor tri-junction point and the meniscus angle (after [89]). A fiber will decrease in diameter, if the meniscus angle Φ is smaller than the growth angle Φ_0 and increase vice versa (if $\Phi_0 > 0$).

Rudolph describes the capillary stability of fiber crystals [105]. A SCF will crystallize with constant radius, if $\Phi = \Phi_0$ (figure 2.5). Deviations of the actual meniscus angle Φ from Φ_0 by perturbations of the meniscus height or radius lead to non-stationary variations of the fiber diameter [5]. Kim et al. studied the maximum stable zone length at float-zone growth of small diameter sapphire and silicon crystals [71]. They concluded that the zone height is primarily limited by the surface tension because of small Bond numbers. This can be applied to LHPG growth as well because of the small melt volume. A stable LHPG growth of oxides occurs for a maximum zone length l_{max} of [47]

$$l_{\max} = 3/2(r_{\mathrm{scf}} + r_{\mathrm{feed}}). \tag{2.5}$$

For the mPD case the maximum meniscus height h_{max} can be determined as [47]

$$h_{\max} = 2\gamma/p_{\mathrm{hydro}} \tag{2.6}$$

with γ as surface tension and p_{hydro} as the hydrostatic pressure of the surrounded melt.

Steady state

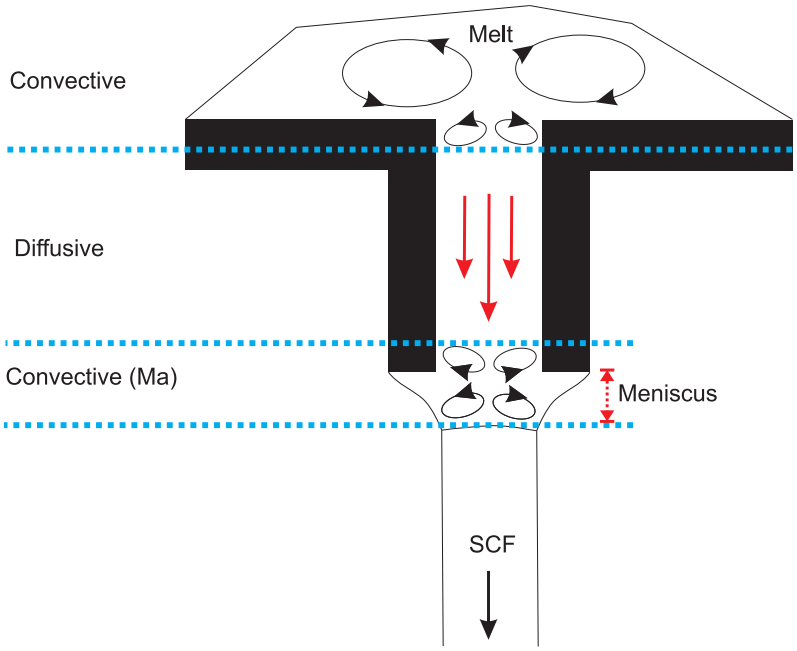

Figure 2.6: Flow patterns in mPD setup under steady state conditions [46].

The term steady state includes dimensional stability (section 2.1.3) on the one hand. On the other hand, it also includes the mass flows, which take evaporation and segregation into account. The steady state conditions in LHPG and mPD techniques depend on a complex interplay of segregation, evaporation, and mass transfer. In LHPG, the onset of steady state condition is strongly affected by the evaporation of species. Because of the higher surface-to-volume ratio, when compared to mPD, the evaporation has more influence on the melt composition. If no evaporation occurs, a LHPG SCF will eventually incorporate exactly the same composition as the feed (steady state). The melt zone has a different composition and is enriched ($k_{\text{eff}} < 1$) or depleted ($k_{\text{eff}} > 1$). In this case, LHPG is rather solution growth than melt growth. If evaporation occurs, the ideal steady state will not be established. But a quasi-steady state will be established, if the composition of the melt zone and the crystallized fiber do not change with time. The melt convection in steady state growth will be discussed in section 5.7.

In principle, consumption of the melt is small during fiber growth by the mPD method [47]. Therefore, a quasi-steady state is attainable even for non-unity segregation coefficients ($k_0 << 1 \vee k_0 >> 1$). Epelbaum describes the flow patterns in mPD setup under steady state conditions [46] (figure 2.6). Within the capillary (crystal shaper) the flow is dominated by diffusion, whereas the Marangoni convection dominates the melt meniscus. When steady state conditions are fulfilled, fibers can be pulled with effective distribution coefficients close to one ($k_{\text{eff}} \approx 1$). The ICP-OES results will show the dependencies of the steady state conditions on the growth parameter with respect to the dopant (section 5.5.1) and the main elements (section 5.5.2).

2.2 Thermodynamics and phase relations

A fundamental requirement for every crystallization process is the achievement of supercooling or supersaturation [27]. Therefore, thermodynamic studies are essential for the understanding of the crystal growth process. This section will introduce the basic thermodynamic phenomena with respect to crystal growth processes. The application of phase diagrams and thermodynamic calculations for improvements of the fiber crystal growth experiments are demonstrated in chapter 4. It is useful to define following terms prior to the basic concept of thermodynamics:

System

A system is described by its extensive properties volume V and mass m, and by its intensive properties pressure p and temperature T. Whereas intensive properties do not change if two identical systems are united (in equilibrium), the values of V and m depend on the system size. A system will be regarded as open, if matter and energy exchange from the system to the surrounding is possible. Furthermore it can be closed (energy exchange only) or isolated (neither energy nor mass exchange) [9]. mPD and LHPG will be considered as open, if crystal growth is performed in fluent atmosphere, or closed (constant atmosphere).

Component

A component is a chemically independent constituent of the system. The number of components C in a system is the minimum number of independent species necessary to define the composition of all the phases P within a system [9].

Phase

A homogeneous state of matter that is uniform in chemical composition and physical state. In general, the scales of a phase P are large compared with atoms. Within a crystal growth system (from the melt) there are typically one gas phase, one liquid melt phase (in case of non-mixing two liquids can occur), and a crystalline phase. Solid compounds often form a separate phase with a specific crystal structure. On the other hand, they may intermix within a solid solution. This requires similar or identical crystal structures and similar crystal chemistry parameters (e.g. valence, atomi radii).

2.2.1 Gibbs energy and equilibrium

The extensive Gibbs energy of a system is defined as [9]:

$$G = H - TS, \tag{2.7}$$

with H as enthalpy, and S as entropy. A system at constant temperature and pressure will always approach a state of minimal G. This state is the equilibrium state of a system [98]. G can be transformed into a intensive state variable $G/n = g$, the molar Gibbs energy, where n is the amount of substance. The partial molar Gibbs energy of an ideal gas can be written as [9]:

$$g_i = g_i^0 + RT \ln(p_i). \tag{2.8}$$

g_i^0 is the standard molar Gibbs energy (at standard pressure), p_i is the partial pressure, R is the ideal gas constant (8.314 J/(K×mol)). For chemical reactions the Gibbs energy of a system will be [98]:

$$\mathrm{d}G/\mathrm{d}n = \Delta G^0 + RT\ln(p_i) = \Delta G, \tag{2.9}$$

with ΔG^0 and ΔG as standard Gibbs energy change and Gibbs energy change of the reaction. If $\Delta G < 0$, then a reaction will proceed to the right side to minimize G. In equilibrium state, where $\Delta G = 0$, the standard Gibbs energy change is therefore [98]:

$$\Delta G^0 = -RT\ln(K), \tag{2.10}$$

with K as the equilibrium constant of the regarded reaction, which expresses the partial pressures, fugacities or activities of a treated reaction [9]:

$$K = (\prod_i (f_i^{v_i}), \tag{2.11}$$

with f_i as fugacity of a component i and v_i as its stoichiometric number. A fugacity can be treated as effective pressure and contains the deviation of the real gas pressure from the ideal gas pressure [9]. Based on equation 2.10 predominance diagrams can be constructed. One example is the calculated diagram 5.4 on page 56 that contains fugacities f_i instead of partial pressures p_i. Constructions of predominance diagrams depend on the mentioned minimization of the Gibbs energy and the phase rule [95]:

$$F = C - P + 2, \tag{2.12}$$

that is a general relation between the variance F of a system with its phases P and components C in the equilibrium case. For example, in a two-component system, as discussed for the CaO-$CaSc_2O_4$ relation in figure 4.13, the liquidus line is univariant. This implies, either the temperature or the chemical composition can be varied. The phase rule for this line can be formulated as F=C-P+2=2-2+2=2. As the pressure is kept constant, only one variation remains ($F = 1$). Ellingham diagrams are special cases of predominance diagrams as they depict the dependency of the Gibbs energy on the temperature (e.g. $RT(lnp_{02})$ versus T).

If two or more solid or liquid components arise within a system, the partial molar Gibbs energy of the mixing (of the solution), Δg_m, will be [98]:

$$\Delta g_m = g - (\sum X_i g_i^0), \tag{2.13}$$

with X_i as mole fractions of a component i:

$$X_i = \frac{n_i}{\sum_{j=1}^{m} n_j}. \tag{2.14}$$

n_i as the number of moles of a component i. If the molar Gibbs energy of mixing is negative, $\Delta g_m \leq 0$, the components intermix. When two ore more phases are in equilibrium, the partial molar Gibbs energy of each component is the same in all phases [98]. The Gibbs-Duhem equation expresses the dependency of the partial molar Gibbs energies [98]:

$$\sum_j (X_i \mathrm{d}g_i) = 0. \tag{2.15}$$

This implies that the partial molar Gibbs energy of a component i cannot change independently of the Gibbs energies g_j ($j \neq i$). Since the ideal enthalpy of mixing is zero [98], the ideal Gibbs energy of mixing can be formulated as follows [98]:

$$\Delta g_{\mathrm{m}}^{\mathrm{ideal}} = RT \ln(X_{\mathrm{i}}) = RT \ln(a_{\mathrm{i}}^{\mathrm{ideal}}), \tag{2.16}$$

with $a_{\mathrm{i}}^{\mathrm{ideal}}$ as activity of a component i. Activities can be treated as effective mole fractions X_i of a component i according to fugacities f_i as effective partial pressures p_i. In the case of non-ideal behavior of mixed phases, the deviation from the ideal solution can be expressed by adding an extra excess term to the Gibbs energy of mixing according to [9]:

$$g^{\mathrm{E}} = \Delta g_{\mathrm{m}} - \Delta g_{\mathrm{m}}^{\mathrm{ideal}}. \tag{2.17}$$

In the case of $g^{\mathrm{E}} > 0$, the solution is less stable than an ideal solution (positive deviation from the ideal term).

2.2.2 Binary phase diagrams

Binary phase diagrams can be constructed from $g^{0(l)}$ versus X_i and $g^{0(s)}$ versus X_i functions. $g^{0(l)}$ and $g^{0(s)}$ represent the standard molar Gibbs energy of the liquid and solid state of a system. A tangent construction of the $g^0(X_i)$ curves reveal the phase fields for the coexistence of two phases [98]. Typically, in crystallization from the melt and structural changes the total pressure p of a system has only minor influence on the process (because of small volume change). Therefore, binary phase diagrams are representative T versus X_i diagrams with constant pressure. The phase diagrams in section 2.3.2 are examples for T versus X_i diagrams. Relevant information that can be collected from this diagrams will be explained in section 2.3.2.

Phase equilibria can be calculated by the minimization of Gibbs energy [114]. For a given set of constraints (e.g. fixed p, overall composition) free energy minimization algorithms find the mole numbers n_i and the compositions of all relevant solution phases within a system, which globally minimizes G [98]. These algorithms use thermodynamic databases for the minimization process. A powerful tool that combines the algorithm (of G minimization) with a large thermodynamic database is the Factsage™ software. It is a fusion of the software packages FACT-Win (formerly F*A*C*T) and ChemSage (formerly SOLGASMIX) [11]. A compound database and another for solution species are embedded in the software. Among other the stored data includes values of the standard enthalpy ΔH^0, the standard entropy S^0, the heat capacity at constant pressure $C_p(T)$, and the molar volume of species. The calculation of growth conditions (section 5.1) is performed using this software.

2.2.3 Thermal analysis

Thermal analysis contains a set of methods to investigate phase diagrams. High-temperature differential thermal analysis (HT-DTA) was used for the determination of relevant phase relations. Heat flux differential thermal scanning calorimetry (DSC) was used for C_p measurements. Both methods measured the thermal gravimetric function (TG) of the samples as well. In general, the term thermal analysis summarizes a set of methods that determine chemical and physical properties of a substance dependent on the temperature or time while the substance is exposed to a temperature program [1].

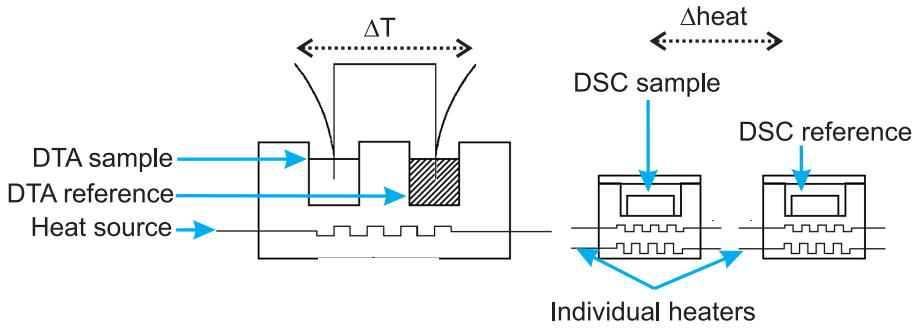

Figure 2.7: Principle setup for DTA (left) and power compensation DSC (right) (after [106]). Note that the thermocouples within the DTA setup used for this work contacted the sample holder and not the sample itself.

DTA and (power compensation) DSC differ from each other in the set sample-heating-source-thermocouple: Using differential thermal analysis the temperature difference between the sample (s) and a reference sample (r) ($\Delta T = T_r - T_s$) is recorded as a function of time (and temperature) (figure 2.7, left). In contrast to this, the differential scanning calorimetry measures different heat (power) that is required for establishing $\Delta T = T_r - T_s = 0$. This is performed by a different setup (figure 2.7). In the DTA setup the sample and reference are embedded within the same heating system, the power compensation DSC sample and reference are heated individually. An alternative DSC concept is applied in the STA 449 (Netzsch, Germany), which was used in this study. The setup is similar to a DTA (figure 2.7, left), but additionally a disk allows the controlled flux of heat between sample and reference. The quantity of this heat flux is proportional to the heat energy that is consumed or created in the sample.

The DTA system used in this work is a free-standing crucible measuring system [61]. In contrast to figure 2.7, the protected thermocouples are in contact with the sample holder instead of the sample. The experimental setup is presented in 3.3. With the DTA method it is possible to investigate the stability of phases (e.g. decompositions, melting points), recognize solid state transitions (e.g. change in crystal structure), and thus constructing phase diagrams. Advantages of DTA are high operating temperatures (up to 2400 °C) and a high sensitivity of the signal. However, the limitations of high-temperature DTA that is affected by evaporation of species and degeneration of the thermocouples and crucibles are visualized (section 4, 7). If the DTA signal is coupled with the TG signal (simultaneous thermal analysis - STA), further information about the process (e.g. purity, evaporation) can be detected. An increase of the heating rate and the sample size shifts the TG signal towards higher temperatures (heating cycle). The differential scanning calorimetry requires a more complex design than the DTA setup [48]. The properties of the measuring system should depend as little as possible on the sample properties and the heating rate [61]. This will be achieved, if the temperature field of the measuring system does not depend on sample properties but on the measuring system itself (dominance of the measuring system, [61]). Whereas enthalpies can be detected semi-quantitatively using DTA, it is possible to measure accurate enthalpies for melting/crystallization with the DSC technique.

Phase modifications, melting and crystallization, sublimation, and decomposition are described by the term phase transition. If the first derivative of the chemical

potential with respect to temperature is discontinuous, a transition will be classified as a first-order phase transition [9]. All first-order phase transitions possess a latent heat: At the transition temperature, the enthalpy H changes by a finite amount for an infinitesimal change of temperature (C_p becomes infinite) [9]. All crystallization and melt processes are first-order transitions. In contrast to this, in a second-order phase transition the first derivative of the chemical potential with respect to temperature is continuous, but the second derivative is discontinuous. Therefore, $C_p(T)$ is discontinuous, but does not become infinite at the transition temperature. Examples for second-order phase transitions are ferroelectric and ferromagnetic transitions.

2.3 Luminescence and laser materials

Material	$CaSc_2O_4$	SrY_2O_4	Sr_3SiO_5
Melting point (°C)	2110 [101]	≈ 2170	2170 [44]
Density (g/cm^3)	3.9 [50]	5.3 [79]	4.7
Thermal conductivity (W/(m·K))	8.4 [50]	7.4 [79]	-
Band gap (eV)	≈ 5.8 [39]	6.1 [10]	≈ 6.0 [62]
Linear th. expansion coeff. α ($10^{-6}K^{-1}$)	11.71 [83]	11.31 [83]	-

Table 2.2: (Thermo-)Physical properties of the materials CS2, SY2, and TSS.

Three materials investigated as light phosphors, calcium scandate (CS2) [113], strontium yttrium oxide (SY2) [124], and tristrontium silicate (TSS) [97], are in the scope of this work. All materials have melting points above 2100 °C. Some material properties are listed in table 2.2. Despite their melting point, they have the following properties in common: CS2 and SY2 are isostructural. As of this writing, calcium scandate and tristrontium silicate are the only known non-cubic host materials, in which the luminescence of trivalent cerium is within the green light region [39, 65]. All three materials have band gaps of ≈ 6 eV. CS2 and SY2 have relatively high thermal conductivities when compared to other oxides (table 2.2). Note that the thermal conductivity of TSS has not been investigated yet. Because of these common features tristrontium silicate and strontium yttrium oxide can act as reference materials to calcium scandate, which is the main issue of this work: The doping mechanism and the crystal growth parameters can be compared between CS2 and SY2. Regarding CS2 and TSS the luminescence properties and laser potential can be compared.

2.3.1 Crystal structure

Tristronstium silicate crystallizes within the tetragonal space group $P4/ncc$ (No. 130). The crystallographic properties [26], table 2.3, reveal a structural resemblance with the Cs_3CoCl_5 type [88]. The latter, among several other pentaoxometallates, crystallizes within the body centered space group No. 140 ($I4/mcm$) [88]. Figure 2.8 reveals the differences between both structures. According to Mansmann [88] the A_3MeX_5 structure type (e.g. Cs_3CoCl_5) is stabilized by large A cations (Cs^{2+} 167 pm, Ba^{2+} 135 pm when sixfold coordinated [110]). The smaller size of the Sr^{2+} ions (118 pm) causes a 16.5 degree torsion of the SiO_4 tetrahedra with respect to the base diagonal in the (001) plane (figure 2.8). This torsion, which is altering in

Formula	Sr_3SiO_5		
Symmetry	tetragonal		
Space group	No. 130 ($P4/ncc$)		
Lattice constants (Å)	$a = 6.949$	$c = 10.757$	
Cell volume (Å^3)	521.97		
Formula units/unit cell	4		
Atom positions [26]			
Atom	Wyck.	x	y	z
8 Sr1	8f	0.181	0.181	0.250
4 Sr2	4c	0.000	0.500	0.000
4 Si	4b	0.000	0.000	0.000
16 O1	16g	0.169	-0.092	0.088
4 O2	4c	0.000	0.500	0.250

Table 2.3: Structure parameters and crystallographic properties of Sr_3SiO_5, data collected from [26, 88, 58, 85] (Wyck. - Wyckoff position).

Formula	$CaSc_2O_4$	SrY_2O_4	
Symmetry	orthorhombic		
Space group	No. 62 ($Pnma$)		
a(Å)	9.65	10.08	
b(Å)	3.16	3.40	
c(Å)	11.2	11.91	
Cell volume (Å^3)	341.53	408.18	
Formula units/unit cell	4		
$CaSc_2O_4$ atom positions			
Atom	Wyck.	x	y	z
4 Ca	4c	0.755	0.250	0.654
4 Sc1	4c	0.420	0.250	0.107
4 Sc2	4c	0.433	0.250	0.612
4 O1	4c	0.203	0.250	0.172
4 O2	4c	0.122	0.250	0.481
4 O3	4c	0.519	0.250	0.786
4 O4	4c	0.420	0.250	0.430
SrY_2O_4 atom positions				
Atom	Wyck.	x	y	z
4 Sr	4c	0.751	0.250	0.653
4 Y1	4c	0.424	0.250	0.109
4 Y2	4c	0.426	0.250	0.609
4 O1	4c	0.210	0.250	0.193
4 O2	4c	0.139	0.250	0.467
4 O3	4c	0.520	0.250	0.776
4 O4	4c	0.414	0.250	0.410

Table 2.4: Structure parameters and crystallographic properties of $CaSc_2O_4$ and SrY_2O_4, data collected from [91, 93, 92, 83].

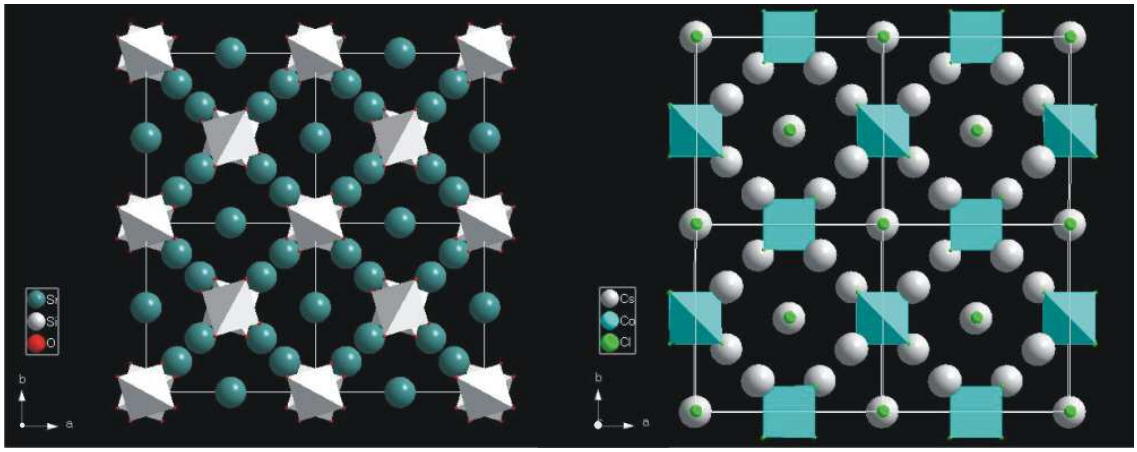

Figure 2.8: Unit cells (2×2×2 clusters) of Sr_3SiO_5 (left) and Cs_3CoCl_5 (right). Projection in [001] direction. Note that the origin in both structures is different.

	[8]	[6]	[4]
Mg^{2+}	89	72	-
Ca^{2+}	112	100	-
Sr^{2+}	126	118	-
Ba^{2+}	142	135	-
Sc^{3+}	87	75	-
Y^{3+}	102	90	-
Si^{4+}	-	40	26
Ce^{3+}	114	101	-
Ce^{4+}	97	87	-
Nd^{3+}	111	98	-

Table 2.5: Overview of relevant ionic radii for eightfold, sixfold and fourfold coordination. All values in pm [110].

[001] direction, causes the transition from body centered to primitive cell. Sr_3SiO_5 can be described as an oxy-orthosilicate [58]. The SiO_4 tetrahedra are isolated, additional oxygen atoms that do not belong to a SiO_4 tetrahedron are surrounded by four Sr1 (Wyckoff 8f) and two Sr2 (4c) atoms. The resulting formula can be written as $Sr_2SiO_4|SrO$ compound. It was possible to refine the crystal structure of tristrontium silicate with fabricated SCFs. The results are presented in section 5.6.3.

Both oxides, $CaSc_2O_4$ and SrY_2O_4, belong to the $CaFe_2O_4$ structure type, described by Müller-Buschbaum as AM_2O_4 oxometallate showing tunnel structures [92]. In his work, Müller-Buschbaum thoroughly describes this structure type. Although CaV_2O_4 has been described prior to $CaFe_2O_4$, AM_2O_4 oxides that crystallizes in *Pnma* are called calcium ferrate(III)-type. Among a variety of different structures of AM_2O_4 this type shows a characteristic MO_6 octahedra network [92]. In figure 2.9 the framework of ScO_6 octahedra (green) of CS2 is connected via edges and corners. Trigonal prismatic cavities are occupied by the Ca^{2+} ions that are surrounded by eight oxygen atoms. The polyhedron (figure 2.9, blue) is an eightfold coordinated bicapped trigonal prism. Oxides that crystallize in calcium ferrate(III)-type have a certain range of cation radii ratios in common ($0.53 \leq R_M/R_A \leq 0.89$) [92].

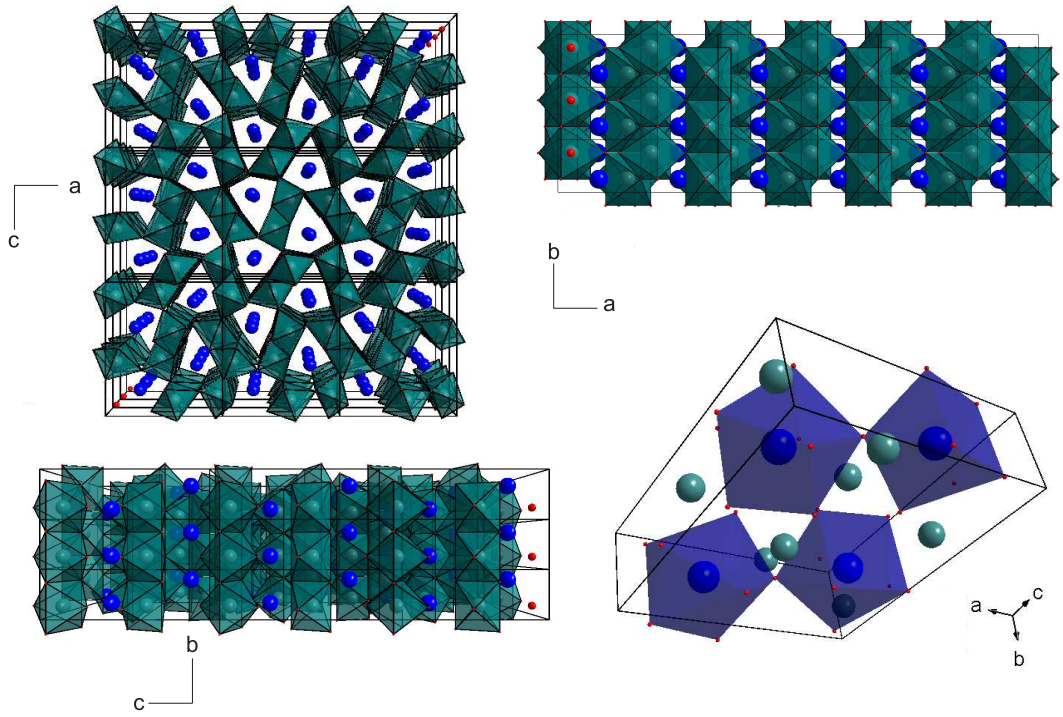

Figure 2.9: Unit cells (3×3×3 clusters) of $CaSc_2O_4$ in [010] (top left), [001] (top right), [100] (bottom left) showing ScO_6 polyhedra (green). Unit cell in [131] showing CaO_8 polyhedra.

First crystallographic properties of calcium scandate have been published by Carter and Feigelson [18], atom positions were determined by Müller-Buschbaum [93]. Table 2.4 summarizes structure parameters and crystallographic properties of calcium scandate and strontium yttrium oxide. All atoms are located on the same Wyckoff position 4c. The scandium atoms Sc1 and Sc2 are coordinated by six oxygen atoms. The Sc-O distances are vary from 2.04 to 2.22 Å [93]. The crystallographic properties of strontium yttrium oxide are similar to the calcium scandate properties (table 2.4). The larger sizes of the Sr^{2+} and Y^{3+} cations cause larger lattice constants and cell volume [91]. Refined chemical bond parameters are given in [83]. The alkaline earth metal scandates $MgSc_2O_4$, $SrSc_2O_4$, and $BaSc_2O_4$ demonstrate boundaries of the structure type. A $MgSc_2O_4$ phase has been reported in 1966 [91], but due to similar ion radii of Mg^{2+} and Sc^{3+} (table 2.5) a statistical distribution of cations on the metal positions was assumed. In recent publications that investigated the phase system MgO-Sc_2O_3 no intermediate compound has been reported [72]. Instead, a MgO_{ss}+Sc_2O_{3ss} phase relation was reported. However, an estimated metastable liquid miscibility gap in the phase system might include a metastable mixed oxide $MgSc_2O_4$ above 1900 °C [72]. $SrSc_2O_4$ is isostructural with $CaSc_2O_4$ [50]. Possible laser potential of $CaSc_2O_4$:Yb^{3+} and $SrSc_2O_4$:Yb^{3+} has been reported by Gaume et al. [50]. Calcium scandate has a better thermal conductivity (8.4 W/m·K) than strontium scandate (6.4 W/m·K) and is considered as promising laser material with difficult crystal growth application [50]. In $BaSc_2O_4$ the large radii of the Ba^{2+} ions inhibit a crystallization in $CaFe_2O_4$ type. The resulting structure has monoclinic symmetry (space group No. 15, $C2/c$) with a pseudo-orthorhombic unit cell (β=90°) [4].

Doping

Doped atoms inside a crystal structure are treated as imperfections of the lattice. The doping mechanism can be formulated using a notation presented by Kroeger and Vink [78]. Regarding the crystal structure and ionic radii (table 2.5) a presumably valence-coupled diadochy can be formulated as follows:

$$Ce_2O_3 + 3Ca^x_{Ca} = 2Ce^{\bullet}_{Ca} + 3CaO + V''_{Ca}. \tag{2.18}$$

Two trivalent cerium ions substitute two Ca^{2+} ions within the calcium scandate lattice because of similar ionic radii (114 pm to 112 pm, when eightfold coordinated). The resulting holes of the two cerium atoms on the calcium positions $Ce^{\bullet}_{Ca}$ can be compensated by one calcium void V''_{Ca} within the lattice. On the other hand, the holes could be compensated by an interstitial oxygen atom O''_i:

$$Ce_2O_3 + 2Ca^x_{Ca} = 2Ce^{\bullet}_{Ca} + 2CaO + O''_i. \tag{2.19}$$

The investigation of the composition shift and segregation of crystal fibers (5.5) will show that the first formulation (equation 2.18) is more likely than the latter one. If cerium is tetravalent, a valence-coupled diadochy on the calcium position will be unlikely. The ion radius of eightfold coordinated Ce^{4+} only 97 pm. If substituted on the Ca position, there would be two electron holes per substituted atom. Therefore, a diadochy with scandium ions is favored:

$$2CeO_2 + 2Sc^x_{Sc} + Ca^x_{Ca} = 2Ce^{\bullet}_{Sc} + 2ScO_{1.5} + CaO + V''_{Ca} \tag{2.20}$$

or

$$2CeO_2 + 2Sc^x_{Sc} = 2Ce^{\bullet}_{Sc} + 2ScO_{1.5} + O''_i. \tag{2.21}$$

Note that calcium is included in the diadochy in equation 2.20. Investigation of the composition shift will mark a negative deviation of Ca atoms (5.5). Therefore, calcium voids are more likely than hypothetical scandium voids V''_{Sc} within the lattice.

If strontium yttrium oxide is doped with trivalent cerium, a valence-coupled diadochy will be unlikely. Instead, a Ce^{3+}-Y^{3+} exchange seems to be reasonable. Tetravalent cerium can substitute trivalent yttrium in the same way as formulated in equation 2.20 for the calcium scandate. The occupation of different sites in both materials causes different absorption and emission properties as it is described in section 5.8. The only possibilities for a Ce^{3+} substitution in tristrontium silicate are either a valence-coupled diadochy according to equations 2.18 and 2.19 or occupation of interstitials. Note that the Cs_3CoCl_5 structure type is stable with large metal ions on the Cs position. The smaller Sr^{2+} ion in Sr_3SiO_5 causes a change in the crystal structure (figure 2.8). It will be shown in chapter 5 that trivalent cerium is more incompatible with tristrontium silicate than the other materials (calcium scandate and strontium yttrium oxide). Moreover, tetravalent cerium will not be incorporated into TSS.

2.3.2 Phase relations

As of this writing, the phase diagram CaO-Sc_2O_3 has not been published. However, phase relations within the ternary system BaO-CaO-Sc_2O_3 have been investigated [80, 76, 81]. In an early work Carter and Feigelson detected $CaSc_2O_4$ as presumably only intermediate compound within the system CaO-Sc_2O_3 [18]. Because of

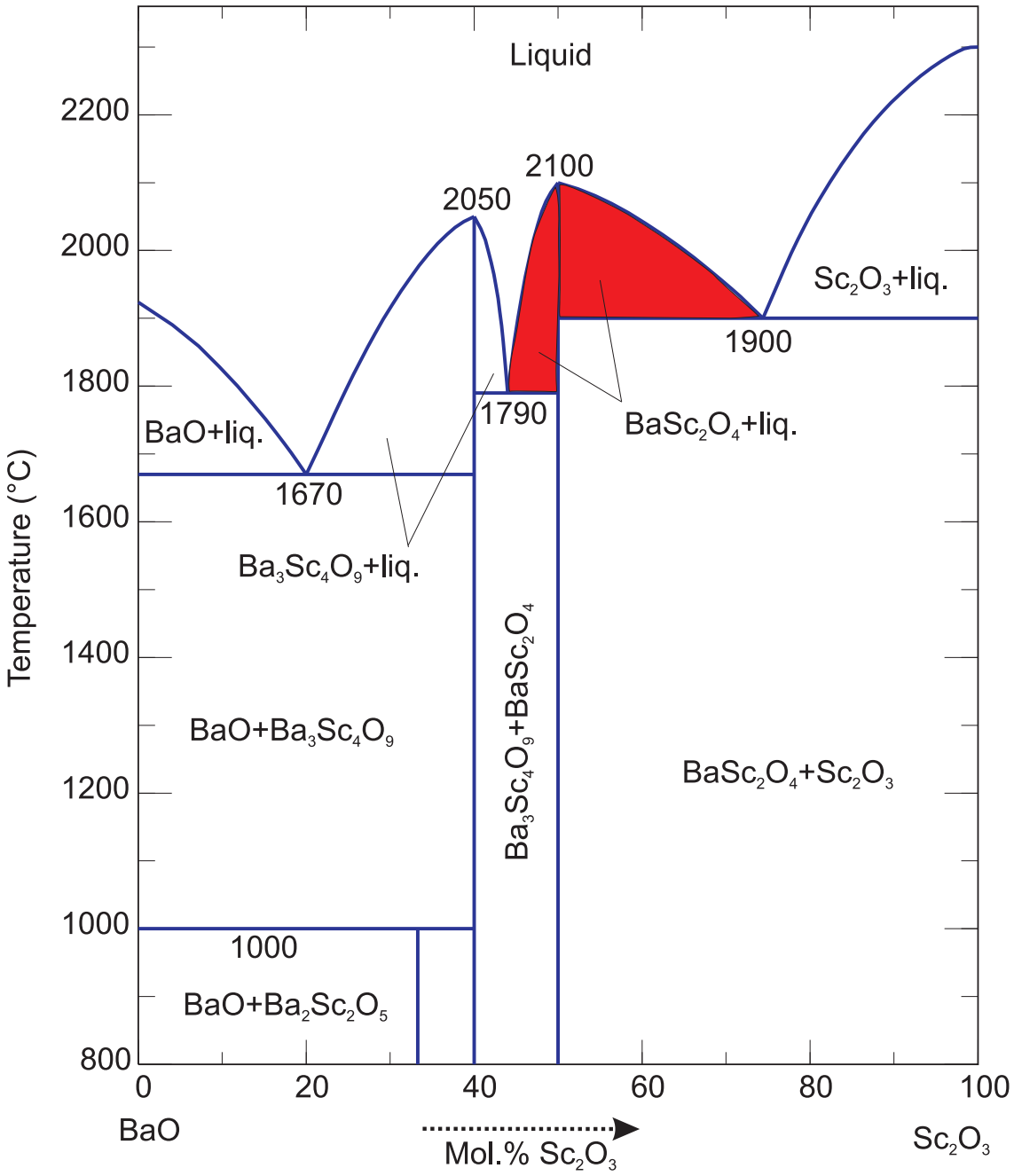

Figure 2.10: The binary phase diagram BaO-Sc_2O_3 (after [76]). Because of chemically resemblance BaO-Sc_2O_3 act as reference to CaO-Sc_2O_3 that is investigated in this work.

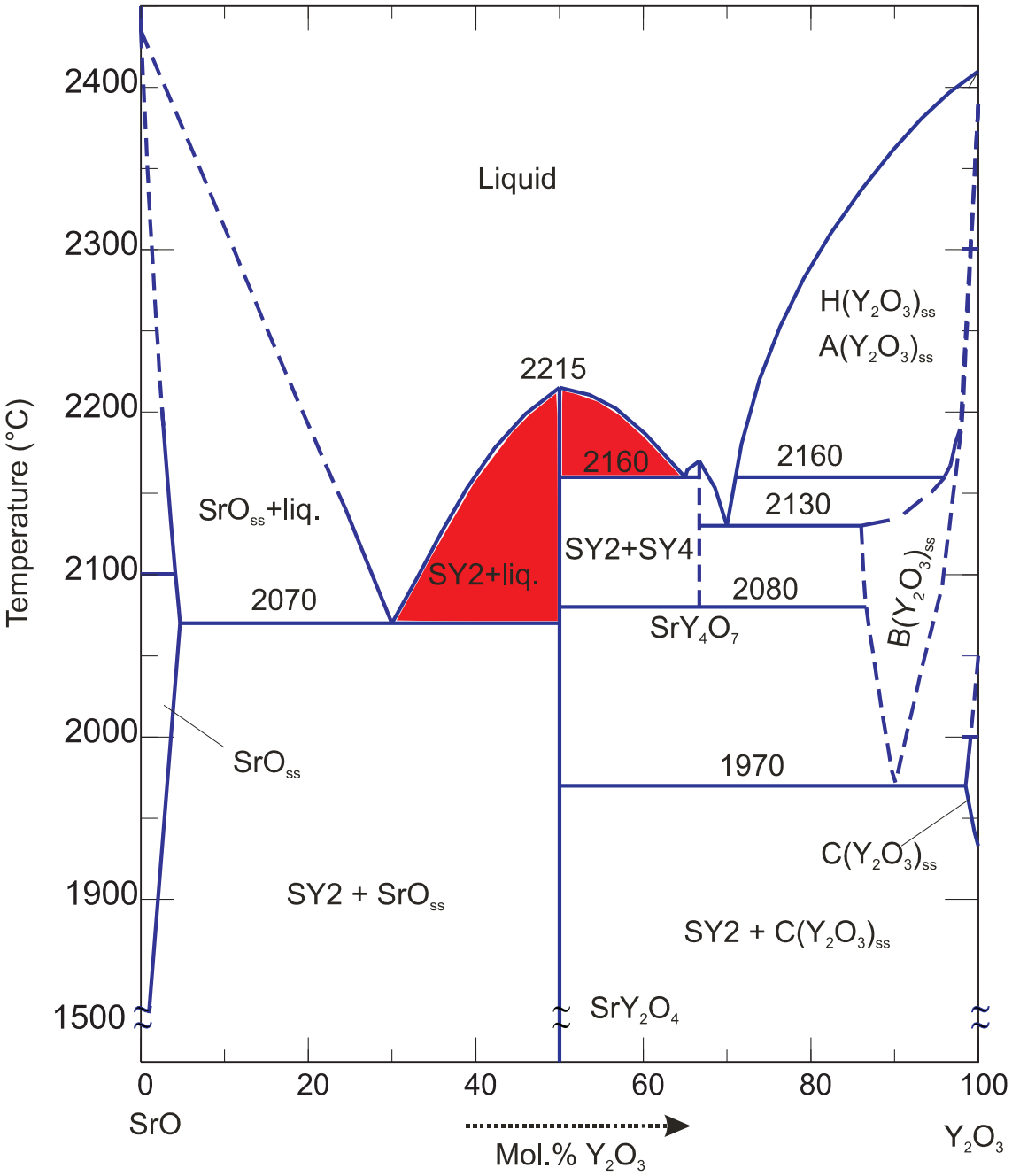

Figure 2.11: The binary phase diagram SrO-Y_2O_3 (after [118]). The areas in which SrY_2O_4 and liquid exist in equilibrium are colored in red.

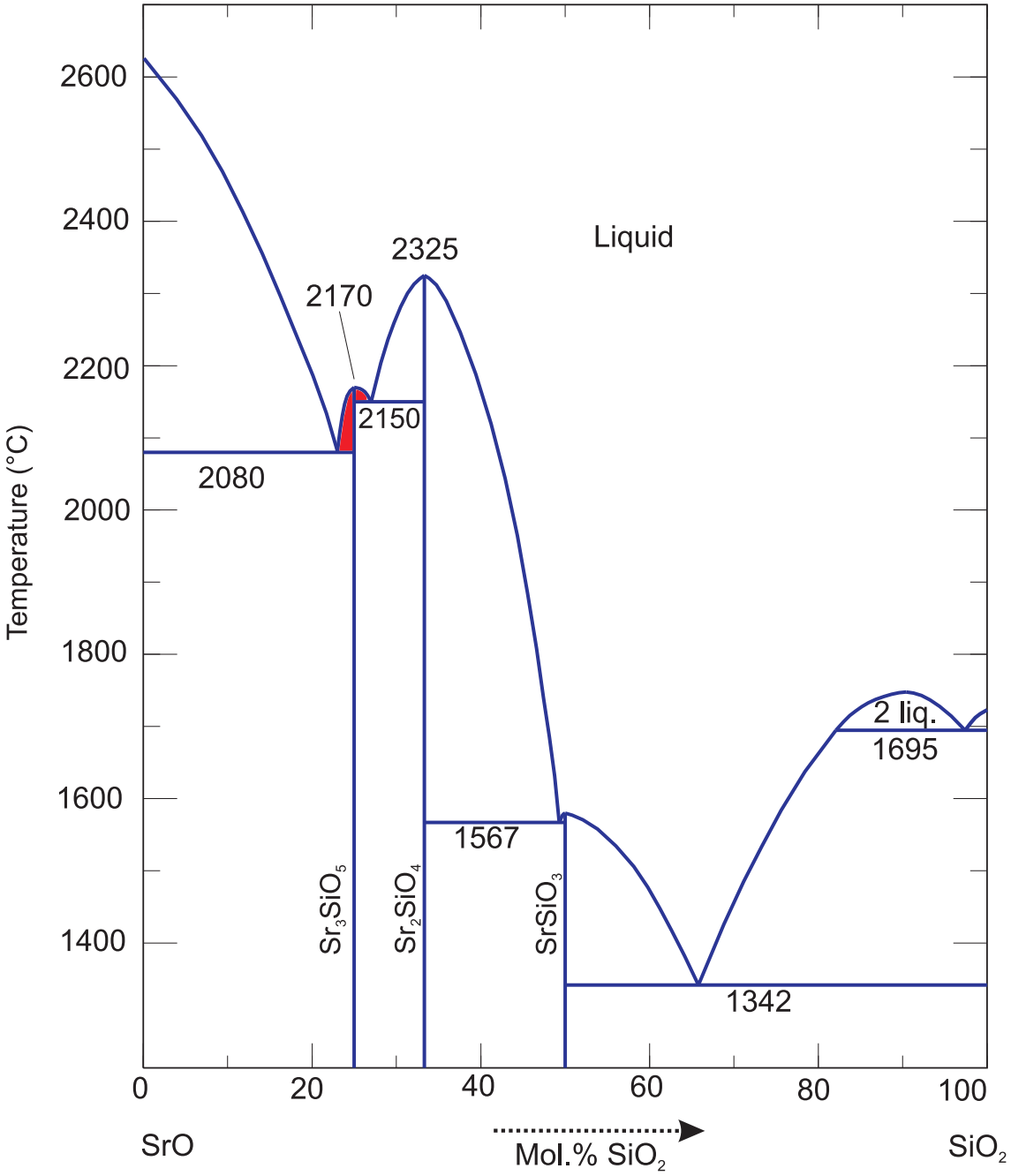

Figure 2.12: The binary phase diagram SrO-SiO_2 (after [63]). The areas in which Sr_3SiO_5 and liquid exist in equilibrium are colored in red.

the chemically resemblance this system might be similar to the system BaO-Sc_2O_3. This diagram is depicted in figure 2.10: The system outlines two intermediate compounds, $BaSc_2O_4$ and $Ba_3Sc_4O_9$ (tribarium scandate), with congruent melting points at 2100 °C and 2050 °C, respectively. $Ba_2Sc_2O_5$ decomposes at ≈ 1000 °C into BaO and $Ba_3Sc_4O_9$. No occurrence of solid solution formation is reported. On either side of barium scandate eutectics occur at 1790 °C and 1900 °C. A eutectic is a mixture composition between two components that melts at lower temperatures than any other possible mixture between these components. It is displayed by an invariant point (F is zero at the eutectic point). A liquid phase with eutectic composition will solidify directly in the solid mixture of both compounds without occurrence of liquid and solid phase, if cooled down [95]. If evaporation or segregation occurs, crystal growth will be performed close to the $BaSc_2O_4$ composition. The relevant two-phase areas (liquid and $BaSc_2O_4$) are filled in red in figure 2.10.

Tresvyatskii et al. published the phase diagram SrO-Y_2O_3 [118], depicted in figure 2.11. The phase equilibria between the two hexagonal phases A and H of Y_2O_3 are not known in detail but are not relevant for this study. Hence, this part of the phase diagram is simplified here. In comparison with BaO-Sc_2O_3 the latter phase diagram is more complex: Despite of solid solutions SrO_{ss} and $(Y_2O_3)_{ss}$ the system contains a phase SrY_4O_7 with a stability region between 2080 °C and 2170 °C. The authors also note a possible peritectic decomposition of SrY_4O_7 at 2160 °C that is not shown here. A peritectic is an invariant point within a binary phase system. This point is characterized by thermodynamic equilibrium between a solid phase β that crystallizes at temperatures below the peritectic temperature and coexisting liquid phase and solid phase α. At temperatures above the peritectic temperature the ratio of α and the liquid phase is given by the lever rule [95].

The system SrO-SiO_2 contains the intermediate phases strontium silicate, distrontium silicate, and tristrontium silicate that all melt congruently [63]. Note that the two eutectic compositions are located close to Sr_3SiO_5. Therefore, if SrO evaporates, the crystallization of Sr_3SiO_5 will be disturbed by crystallization Sr_2SiO_4. Section 5.5.2 will demonstrate this case. Chapter 4 will present and discuss the results regarding phase relations of the relevant materials.

2.3.3 Application as light phosphors

Phosphors are fabricated luminescence materials. A luminescent material converts certain types of energy into electromagnetic radiation [12]. In the literature on luminescent materials, the term phosphor is being used synonymously. Thermal radiation that all solids emit in excess of a certain temperature is not considered as luminescence (but black body radiation). Dependent on the excitation type the phenomena is named after, such as photoluminescence (by electromagnetic radiation), cathodoluminescence (by electron beam), and electroluminescence (by an electric voltage). A historical exception is the scintillation process, in which electromagnetic light is emitted though ionizing radiation. The laser fluorescence, described in section 5.8, is a special type of photoluminescence. Laser radiation instead of conventional light source is used to excite luminescence. Fluorescence, in contrast to phosphorescence, is one of the photoluminescence types. Fluorescence is considered as the property of an atom or molecule to absorb (visible) light at a certain wavelength region and emits light at a longer wavelength region than the incident

light [12]. All processes concerning the phenomenon occur in relatively short time intervals: The absorption process in $\approx 10^{-15}$ s, the vibrational energy relaxation in $\approx 10^{-12}$ s, and the de-excitation in $\approx 10^{-9}$ s. The stokes shift is the shift in wavelength between absorption and emission.

Dorenbos summarizes a variety of luminescence materials, including TSS [30]. CS2 has been investigated as terbium, ytterbium, and cerium doped phosphor [113, 57, 85]. Europium doped TSS has been investigated for LED applications [20]. The photoluminescence of europium doped SY2 has already been investigated by Blasse et al. in 1969 [14]. Application for this material as light phosphor is presented in [125]. Within this work, cerium doped materials are investigated with respect to applications as light phosphors and laser materials.

2.3.4 Electronic states of cerium

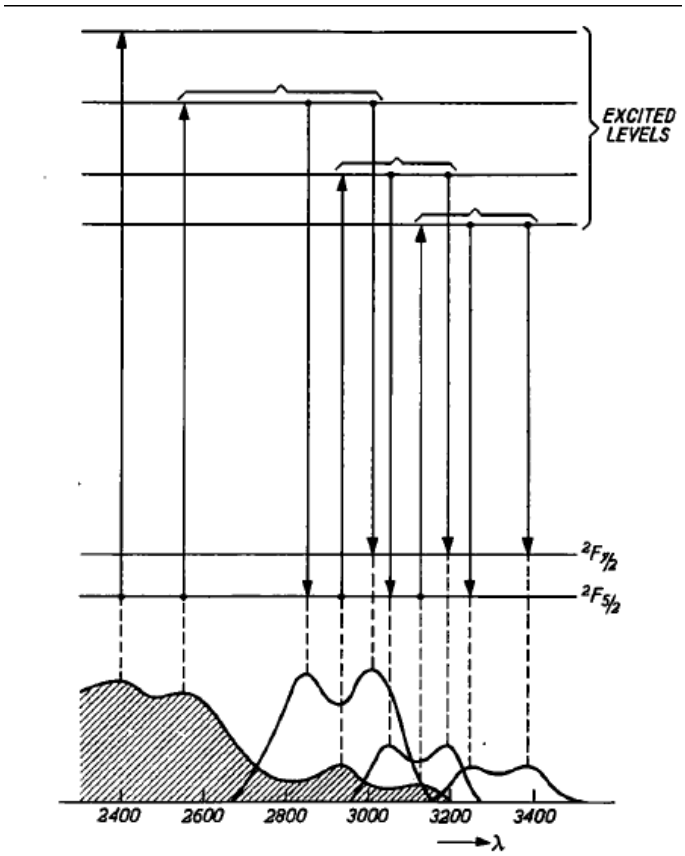

Figure 2.13: An early work of Kröger and Bakker [77] describes the term scheme for cerium phosphors. Wavelength is given in Å.

Trivalent ions of the rare-earth elements (REE) function as optical centers in a variety of solid state laser materials [70]. Trivalent cerium is of particular interest, because it absorbs and emits not in sharp lines, but rather in broad bands [77]. The electronic configuration of Ce^{3+} is $[Xe]\,4f^1$ with only one electron in the 4f shell. The ground state configuration inheres two levels, $^2F_{5/2}$ and $^2F_{7/2}$, separated by $\approx 1900\,cm^{-1}$ due to spin-orbit coupling [12]. Figure 2.13 depicts the term scheme with electronic excited and ground states. The 5d electron orbital is strongly affected by the neighboring ions, therefore the 4f-5d absorption is a broad band [60]. The

positions of the 5d levels of cerium (and other lanthanides) depend strongly on the crystalline environment. The positions of the shielded 4f electrons do not change significantly and remain constant within several 100 cm^{-1} [30]. Dorenbos compiled the data of nearly 400 lanthanides sites in more than 300 compounds. From this data the position of the lowest 5d level can be predicted [29]:

$$E(\mathrm{Ln}, A) = E(\mathrm{Ce}, \mathrm{free}) - D(A) + \Delta\ E^{\mathrm{Ln,Ce}}. \tag{2.22}$$

$E(\mathrm{Ln}, \mathrm{A})$ is the energy difference (cm^{-1}) of a trivalent lanthanide ion between the $4f^n$ ground state level and the lowest $4f^{n-1}5d$ level, incorporated into a compound A. $E(\mathrm{Ce}, \mathrm{free})$ is the the energy of the first f-d transition of Ce^{3+} as free gaseous ion ($\approx$ 49340 cm^{-1} [29]), and $D(A)$ the crystal field depression. The expression $\Delta\ E^{\mathrm{Ln,Ce}}$ is the f-d energy difference of the assigned lanthanide ion with the first electric dipole allowed transition for Ce^{3+} [30]. Thus, all lanthanide 4f-5d transitions are connected to the transition of cerium. The meaning of equation 2.22 implies that the influence of the compound A and the lanthanide ions act independently from each other. When only cerium 4f-5d is regarded, $\Delta\ E^{\mathrm{Ln,Ce}}$ equals zero:

$$E(\mathrm{Ce}, A) = 49340\, cm^{-1} - D(\mathrm{Ce}, A). \tag{2.23}$$

The crystal field depression is the lowering of the 4f-5d transition energy of the free ion by a crystal field when incorporated into a compound A. According to Dorenbos $D(A)$ as well as the resulting stokes shift $\Delta\ S(A)$ can be considered as properties of the host lattice [29]. In general, temperature, cerium concentration, stokes shift, and crystal field depression affect the absorption and emission properties of a cerium doped material. The absorption of the free Ce^{3+} ion is at $\approx$ 201 nm [77]. Therefore, if an emission in the longer wavelength region of visible light is required, a host material must have either a large crystal field depression or a large stokes shift. For strontium yttrium oxide these values are: $D(A) \approx 24140\,\mathrm{cm}^{-1}$, $\Delta\ S(A) \approx 7800\,\mathrm{cm}^{-1}$ [13]. These values are inaccurate, because the excitation band instead of an absorption band was used to calculate $D(A)$ and $\Delta\ S(A)$. However, in comparison to values for other oxide cerium host materials, both the crystal field depression and the stokes shifts are outstanding large [12]. Although some trends for $D(A)$ and $\Delta\ S(A)$ can be observed and phenomenologically predicted, a comprehensive theory is still desirable. The crystal field depression (also called spectroscopic redshift) is a result of two independent contributions: 1. The centroid shift $\epsilon_c(\mathrm{A})$ - the lowering of the average energy of the Ce^{3+} 5d configuration relative to the value for the free ion. 2. The crystal field shift $\epsilon_{cfs}(A)$ - the energy difference between the lowest and highest 5d level [31]:

$$D(A) = \epsilon_c(A) + \frac{\epsilon_{cfs}(A)}{r(A)} - 1890\,\mathrm{cm}^{-1} \tag{2.24}$$

Whereas the centroid shift depends on the co-valence and polarizability of the anions coordinating the cerium ion, the crystal field shift is determined by the shape of the first anion polyhedron around Ce^{3+} [31]. $r(A)$ is the ratio between the crystal field splitting and the crystal field shift. Dorenbos remarks a trend for increase of the depression value for larger cation sites [30]. Therefore, host materials containing large alkaline earth metals are in the scope of this work.

2.3.5 Cerium based laser crystals

LASER is an acronym for Light Amplification by Stimulated Emission of Radiation. Basic requirements for laser are population inversion, laser gain, and threshold gain in a laser cavity. Since optical transitions have a finite spectral width, the absorption coefficient α depends on the wavelength λ [60]. For a medium in thermal equilibrium $\alpha(\lambda)$ will be positive, if $N_a \gg N_b$, N_a and N_b are densities of atoms in the electronic states a and b. With a suitable pumping mechanism a population inversion of the states a and b shifting the system out of thermal equilibrium can be realized [60]:

$$\Delta N = N_b - (g_b/g_a)N_a > 0, \tag{2.25}$$

with g_b and g_a as shape factors [60]. Under these conditions amplification is possible according to [60]:

$$I(l) = I_0 exp(\gamma(\lambda)l), \tag{2.26}$$

with $\gamma(\lambda)$ as small-gain coefficient, l as length of the medium, and I as intensity. The small-gain coefficient results from the atomic processes involved in absorption and stimulated emission only. The gain inside a laser medium G_M must exceed internal cavity losses G_C according to $G_M G_C > 1$. If these requirements are fulfilled, the threshold conditions and thus laser will be possible.

A simple solid state laser consists of a laser active center (e.g. Ce^{3+}) incorporated into a host material (e.g. $CaSc_2O_4$) as laser medium. This medium is surrounded by mirrors forming the laser cavity. With a suitable pumping mechanism (Xe lamps) a laser can be established.

If a cerium host material establishes a large stokes shift, self absorption quenching can be minimized. In this case, the absorption and emission bands only have a small cross section in common [39]. Ce^{3+} ions inhere two laser channels that enable stimulated emission [70]. Already in 1979/1980 fluoride host crystals with Ce^{3+} as active centers have been investigated using the $5d^1 \rightarrow {}^2F_{7/2}$ transition (Ce:LaF_3 [35]) and the $5d^1 \rightarrow {}^2F_{5/2}$ transition (Ce:$LiYF_4$ [36]). In recent years, several other cerium containing materials have been investigated (Ce:LaF_3, Ce:LiCAF, Ce:CaF_2, Ce(Y,Lu)PO_4 [17]). Most of them are fluorides that create a relatively weak crystal field (small D(A)) [28]. Therefore, these materials lase in UV. But also oxides with a large crystal field depression turned into the field of interest, because a solid state laser material that lases in the green range of visible light is still desirable. Ce:YAG has been investigated by Hamilton et al. [56]. Although the material shows many of the characteristics for a solid-state laser material, strong excited state absorption (ESA) into the conduction band quenches stimulated emission. Because of a possible polarization-dependent ESA [39] materials with low symmetry are in the scope of this work. Ce^{3+} ions support tunable laser action based on crystal-field transitions. Their 5d levels, in accordance with 3d levels (e.g. of Cr^{3+}), are strongly coupled to lattice vibrations [59]. In consequence, the 4f-5d transitions are readily shifted to different wavelength regimes by the static crystal field and broadened by vibronic coupling [59].

2.3.6 $CaSc_2O_4$:Ce^{3+} band structure

In his work Fechner describes the band structure of $CaSc_2O_4$:Ce^{3+} [39]. The direct band gap of calcium scandate varies between 5.8 and 7.1 eV depending on the position within the Brillouin zone. The energy range of the conduction band varies

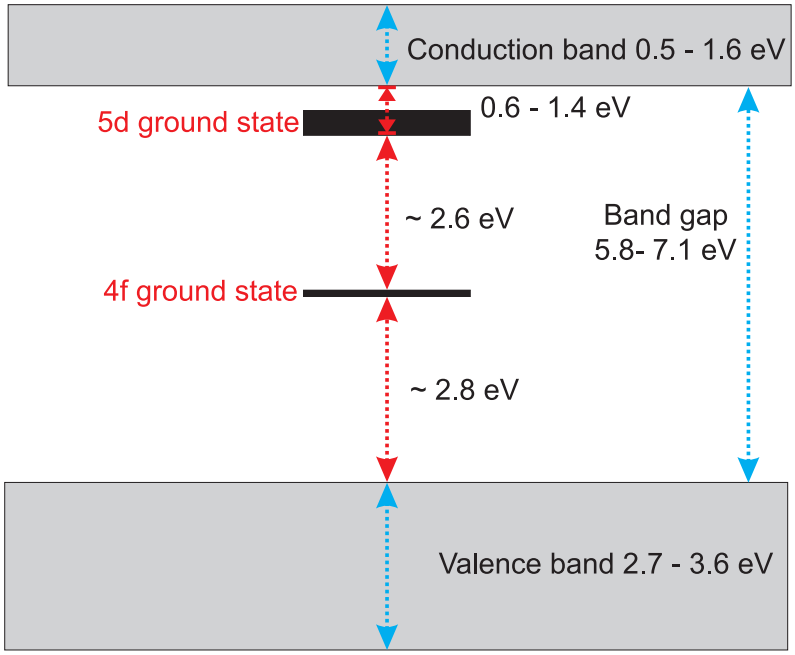

Figure 2.14: Schematic draw of the $4f^1$ and $5d^1$ ground states of Ce^{3+} relative to $CaSc_2O_4$ valence band and conduction band (after [39]).

between 0.6 and 1.6 eV and is much lower than the value for YAG (> 5 eV [24]). This is a reason for the possibility of stimulated emission within the visible light region, because ESA will be less probable [39]. The $4f^1$ and $5d^1$ Ce^{3+} energy levels relative to the band structure of calcium scandate are depicted in figure 2.14. The energy difference between the $4f^1$ ground state and the valence band ($\approx$ 2.8 eV) has been approximated by Fechner after a method described in [32]. Fechner concludes that, depending on the band structure and energy states of trivalent cerium inside calcium scandate, a laser setup with stimulated emission within the visible (green) light range is possible. The following chapter summarizes the experimental setup for investigation of high quality crystal fibers that shall be suitable for luminescence and laser experiments.

Chapter 3

Experimental setup

This chapter gives a concise summary of the experimental work. Thermodynamic calculations predicted equilibrium conditions that are needed for growth experiments (3.1). High-temperature DTA-TG and DSC indicated phase relations are main issue in chapter 4. Preparation, growth experiments, and their parameters are explained in 3.2. Characterization methods for crystal quality investigation and enhancement are described at the end of this chapter (3.3).

3.1 Thermodynamic calculations

Under the very high temperatures during the growth thermodynamic equilibrium is reached quickly, and it can be expected that calculations of thermodynamic equilibrium are a useful tool for the description of the process. Factsage™ [3], an integrated thermodynamic data bank system and Gibbs free energy minimization program, was used for this purpose.

The Factsage™ equilib module minimizes the Gibbs energy for fixed values of T and p varying the amounts of possible products under the constraint that the element balances must be kept constant [3]. Kinetic considerations are ignored. For each growth atmosphere and feed material the amounts n_i of the components i (also including the mole fractions of the gas atmospheres) were inserted for equilib calculation. The following assumptions were made: 1. In LHPG growth only a small volume of the feed is at melting temperature. During mPD growth the total amount of the feed material is liquid. 2. The system was considered to be closed (no mass exchange). 3. For each atmosphere a background of typical $f_{O_2} \approx 2 \times 10^{-6}$ bar has been considered (see table 3.2).

For growth conditions the equilib algorithm determined the combinations n_i, X_i, and f_i that minimized the Gibbs energy G for the system. Most important for crystal growth are the fugacities f_i of evaporating species. f_i indicate possible composition shifts during the growth experiment. Dependencies of the fugacities on the composition, temperature, and pressure are given in section 5.1 on page 54. Using the Factsage™ phase diagram module in combination with the equilib module a predominance diagram, showing the stability of CeO_x phases as function of T and $\log[f_{O_2}]$, was calculated (figure 5.4).

Sample name	Composition	Comment/Assumption
	Calcium scandate	
CS2_P1	$Ca_{1.000}Sc_{2.000}O_{4.000}$	
CS2_P2	$Ca_{2.000}Sc_{2.000}O_{4.000}$	
CS2_P3	$Ca_{0.990}Ce_{0.010}Sc_{2.000}O_{4.010}$	Ce^{3+},Ce^{4+} on Ca
CS2_P4	$Ca_{0.997}Ce_{0.003}Mg_{0.003}Sc_{2.000}O_{4.000}$	Mg^{2+} on Sc
CS2_PS	$Ca_{0.998}Sc_{2.004}O_{4.001}$	Correction factor (Ca)
CS2_P5	$Ca_{0.990}Ce_{0.010}Sc_{2.000}O_{4.010}$	
CS2_P6	$Ca_{0.980}Ce_{0.050}Sc_{2.000}O_{4.080}$	Calcium excess
CS2_P7	$Ca_{0.980}Nd_{0.050}Sc_{2.000}O_{4.055}$	Calcium excess
	Tristrontium silicate	
TSS_P1	$Sr_{3.000}Si_{1.000}O_{5.000}$	
TSS_P2	$Ce_{0.015}Sr_{3.000}Si_{1.000}O_{5.030}$	Ce^{3+} on Sr, Ce^{4+} on Si
TSS_P3	$Sr_{3.000}Si_{1.000}O_{5.000}$	
TSS_P4	$Ce_{0.015}Sr_{2.985}Si_{1.000}O_{5.015}$	Ce^{3+} on Sr
TSS_P5	$Sr_{3.000}Si_{1.000}O_{5.000}$	
TSS_P6	$Sr_{3.000}Si_{1.000}O_{5.000}$	
	Strontium yttrium oxide	
SY2_P1	$Ce_{0.020}Sr_{1.000}Y_{1.980}O_{4.010}$	Ce^{3+} on Y
SY2_P2	$Ce_{0.020}Sr_{1.000}Y_{1.980}O_{4.010}$	

Table 3.1: Overview of the used powders.

3.2 Growth experiments

Table 3.1 lists the composition of the feed materials used for growth experiments. Samples were prepared from $CaCO_3$, $SrCO_3$, MgO, Sc_2O_3, and SiO_2 powders with 99.99 % purity. The dopant cerium was tetravalent CeO_2 (p.a. purity). Note that cerium will be trivalent or tetravalent depending on the atmosphere and temperature (figure 5.4). Different assumptions were made for the powder preparation (comment/assumption) having been chosen depending on the doping process (section 2.3, doping). In powder sample CS2_P4 magnesium was used for possibly valence-coupled diadochy (Mg^{2+}, Ce^{3+} $\leftrightarrow$$Sc^{3+}$,$Ca^{2+}$). Sample CS2_P6 has 5 % cerium that should substitute for calcium. However, a calcium excess was taken into account because of high Ca evaporation. The composition of TSS_P4 was made under the assumption that only trivalent cerium incorporates into TSS.

3.2.1 Feed rod preparation for LHPG

The fabrication of homogeneous high density and high purity feed rods is essential for LHPG experiments [27]. Two different techniques have been used in this work: 1. Cold isostatic pressing and sintering. 2. Cold extrusion technique (described by Andreeta et al. [6]).

1. Powder samples were calcinated at 900 °C for 8 hours. The products were multiply ground and sintered at temperatures up to 1600 °C to ensure complete reaction. Phase purity was checked by XRD. The dried powders were pressed isostatically at 2000 bar in a die, sintered at $1400-1600$ °C for 24 h and cut into rectangular prisms. These prisms were used as feed rods for LHPG. Regarding the sintering temperature a compromise between formation reaction and evaporation had to be balanced. This can be explained with figure 3.1: The DTA (blue) and TG (red) signal of the com-

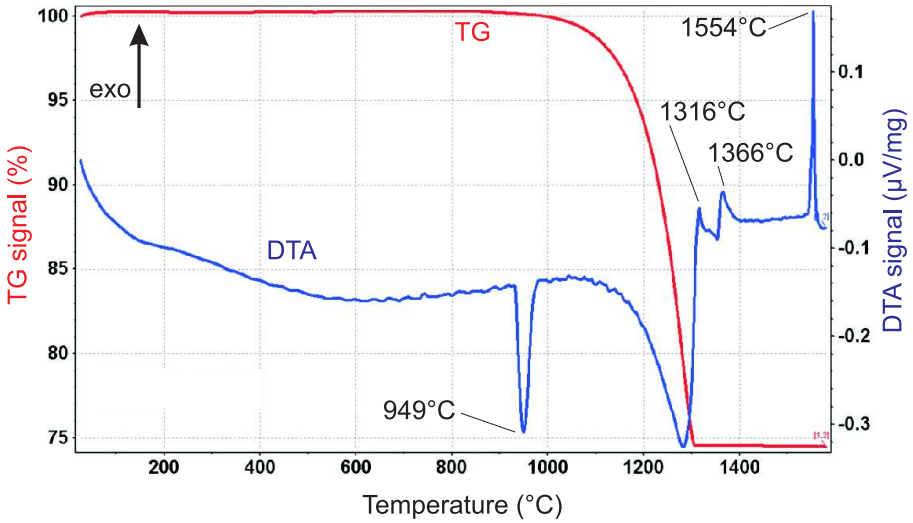

Figure 3.1: DTA (blue) and TG (red) signal of the composition $(SrO)_3(SiO_2)$.

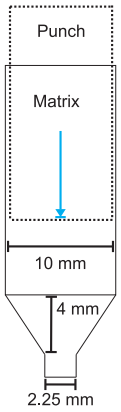

Figure 3.2: Metallic matrix and punch that were used for cold extrusion technique.

position $(SrO)_3(SiO_2)$ indicate several exothermic reaction peaks up to $\approx 1554\,°C$. This fact justifies the high sintering temperature. At lower temperature SrO remains within the feed and will eventually be carbonated. Samples cannot be pressed because $SrCO_3$ decarbonates at high pressures and will destroy the sample. Note, that the endothermic signal with its peak at $\approx 949\,°C$ arise from the thermally delayed phase transition β-SiO_2 to tridymite [95]. The onset of this peak is at $\approx 929\,°C$ and indicates the transition temperature. The TG signal indicates a 28 % mass lost that is mainly CO_2 and subordinated SrO loss (section 5.5).

2. For the cold extrusion technique a metallic matrix and punch was fabricated (figure 3.2). Instead of square sectioned feed rods, samples with round cross section could be prepared. Thereby, a more uniform growth angle could improve the fiber quality [119]. For feed preparation calcium scandate compositions (CS2_P5) were calcinated at $\approx 1000\,°C$ for 10 h. Polyvinyl alcohol was added as an organic binder [104]. Cylindrical rods (green bodies [8]) with 2 mm diameter were extracted and sintered at lower temperatures (in comparison with cold pressing) about $\approx 1000 - 1200\,°C$. Ardila et al. note that lower sintering temperatures can

significantly reduce oxygen vacancies in high melting oxides in LHPG growth [8].

3.2.2 Growth setup

Atmosphere	composition (mbar)
Oxidizing I	Ar (800), O_2 (200)
Oxidizing II	Ar (980), O_2 (20)
Oxidizing III	Ar (950), O_2 (50)
Inert	Ar (1000)
Reducing I	N_2 (1000)
Reducing II	N_2 (990), H_2 (10)
Reducing III	N_2 (950), H_2 (50)
Reducing IV	Ar (900), N_2 (95), H_2 (5)
Reducing V	N_2 (900), CO_2 (80), CO (20)

Table 3.2: Composition of atmospheres for LHPG and mPD experiments. All gases had 5N (99.999 %) nominal purity.

Table 3.2 depicts the composition of the atmospheres that were used for LHPG and mPD experiments. If a rest impurity is assumed as air, an oxygen partial pressure of $p_{O_2} \approx 2 \times 10^{-6}$ bar can be estimated for all atmospheres not already having O_2 as one major component [75]. It will be shown later that N_2 is slightly reducing, compared to Ar (figure 5.4). In both techniques SCFs have been grown in fluent (up to 3 Nl/min) and static atmosphere.

LHPG setup and parameters

Parameter	LHPG
Growth rate	0.1–2 mm/min
Fiber diameter	0.5–2.5 mm
Fiber length	≤ 50 mm
Aspect ratio h/d_{scf}	1–3

Table 3.3: Growth parameters during LHPG process.

The LHPG furnace in this study is similar to the furnace described by Fejer et al. [42]. The LHPG system was constructed and built by Cyberstar (France). The IR laser is a Firestar™ f400 (Synrad, USA). The laser expander consists of two ZnSe lenses (Lasermech, USA). Temperature of the melt zone is measured by a Modline 5 IR pyrometer (Raytek, USA). The recipient can be evacuated ($< 5 \times 10^{-5}$ mbar) by using a turbo molecular pump (Pfeiffer Vacuum, Germany).

SCFs were grown in different atmospheres (reducing to oxidizing, table 3.3). At the beginning of the LHPG process, the top of the feed rod was melted to a small droplet. With low translation rate the seed crystal was directed to the droplet and contacted the melt. After seeding, the seed rod and the feed rod have been moved upwards with similar translation rates until the fiber crystallized with a suitable diameter. With an appropriate ratio of translation rates the fiber crystallized with constant diameter. At the end of the process the seed rod was stopped and the fiber was pulled out of the melt. The laser power as well as the translation rate

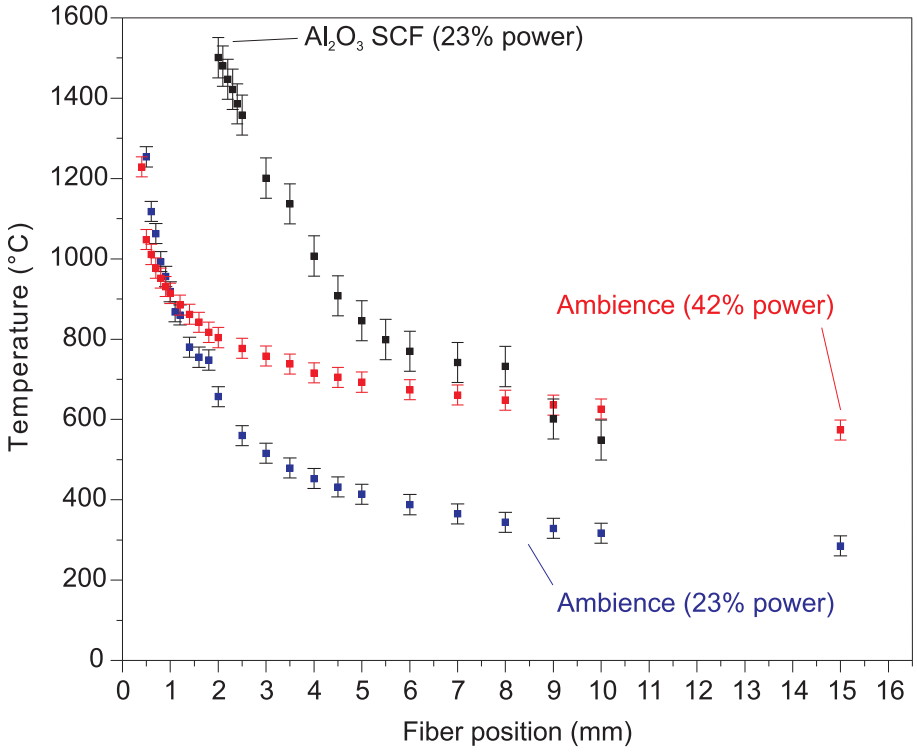

Figure 3.3: Temperature profiles during LHPG process measured using a type B thermocouple. Temperatures of the gas ambience were monitored at 23 % (blue) and 42 % (red) laser power as well as temperature of a growing fiber (black) at 23 % laser power. The melt zone is located at 0 mm.

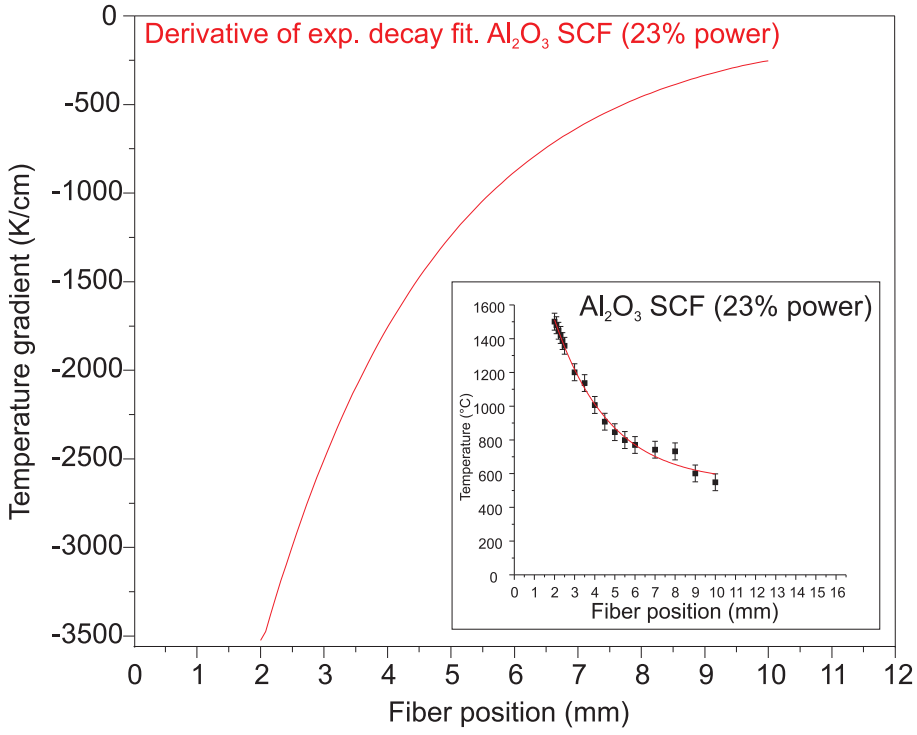

Figure 3.4: The derivative of an exponential decay fit reveals the temperature gradient inside a growing crystal fiber of Al_2O_3.

of the pedestal were adjusted to assure an aspect ratio h/d_{scf} between 1 and 3 (h: height of the melt zone, d_{scf}: diameter of the SCF). The melt zone was overheated approximately 100 to 150 K above the melting point. The temperature was measured with a pyrometer (accuracy $\pm 0.5\,\%$ of the determined surface temerature). The edge length of the pedestal base ranged from 0.8 mm to 2.3 mm. An overview of growth parameters and setup is given in table 3.3.

At high temperatures in the range of the materials melting points thermal radiation is the dominant transport phenomenon. To evaluate the temperature gradient for the given LHPG setup a thermocouple was used. Because of the small system size of the LHPG system pyrometric measurement of a crystallizing SCF did not work. Instead, an Al_2O_3 SCF was grown with a type B thermocouple as seed. The black curve in figure 3.3 defines the temperature distribution of this fiber. The melt zone was set at 0 mm. Because of the high temperatures first accurate temperature values are given at $\approx$ 2 mm above the melting zone. As reference measurements the temperature of the gas ambience above a heated melt zone was measured for 23 % and 42 % total laser power (blue and red curves). In an ideal case, the surface temperature distribution in axial direction should fit a Gaussian function [82]. The curves in figure 3.3 resemble exponential decay functions, because only a part of the temperature distribution was monitored. The Gaussian function combines a parabola and an exponential decay function. The temperature distribution of the part close to the melt zone should fit the codomain of the parabola. The temperature distribution apart from the melt zone, which is depicted in figure 3.3, fits the Gaussian codomain where the exponential decay function is dominant.

The temperature distribution resembles the values given by Andreeta et al. for the growth of $LiNbO_3$ [7]. The deviation of an exponential fit of the temperature distribution is given in figure 3.4. The temperature gradient is up to $\approx 3500\,\mathrm{K/cm}$ and matches the gradient given by Chen et al. for LHPG growth of $LiNbO_3$ [19]. It is noteworthy that the temperature gradient measured within this work is an in-situ gradient of the volume of a growing fiber. Because of similar thermal properties and melting points of aluminum oxide and the investigated materials the determination of the temperature distribution was suitable for the growth experiments. In detail, the steep axial temperature gradient justified the rapid growth rates.

mPD setup and parameters

Parameter	mPD
Growth rate	0.2–1 mm/min
Fiber diameter	0.5–2 mm
Fiber length	≤ 50 mm
Melt meniscus	$\approx 50 - 200\mu$m

Table 3.4: Growth parameters during mPD process.

The setup for the mPD (figure 3.5) furnace is given in section 2.1.4. The parameters are depicted in table 3.4. The crystal growth parameters were selected to produce fibers having similar geometry to the LHPG fibers. Temperature gradient studies that had been performed by Maier using the same crystal growth apparatus were used for adjusting the melt meniscus ($\approx 50 - 200\mu$m) [86]. Further description of the mPD apparatus is given in [86].

Figure 3.5: Photography of the apparatus that was used for mPD growth experiments.

Sintered powders were RF-heated in the mPD furnace in Ir crucibles. The amount of feed material had been chosen with the result that after crystallization of an $\approx 50\,\mathrm{mm}$ SCF enough material remained inside the crucible. By this, it could be ensured that the composition of the melt did not change significantly because of segregation effects (section 2.1.5).

3.3 Characterization methods

Thermal analysis

High-temperature DTA-TG was performed using a STA 429 CD (Netzsch, Germany). Lidded tungsten crucibles and He atmosphere were used. The heating filament and thermal shields consist of tungsten and enable measurements up to 2400 °C. Reactive samples will lower the temperature limit as described in the following chapter 4. Tungsten-rhenium thermocouples are attached at the sample holders. Prior to each measurement the recipient was evacuated ($< 2 \times 10^{-5}\,\mathrm{mbar}$) and rinsed with He for three times. The calcium scandate heat capacity measurement was done with a STA 449 Jupiter (Netzsch, Germany) in oxygen atmosphere.

X-ray diffraction and fluorescence

X-ray source	Cu Kα
Wavelength	0.15406 nm
Range ($^\circ 2\theta$)	$10 - 100$
Step width ($^\circ$)	0.01
Time per step (s)	4

Table 3.5: XRD parameters for phase analysis (XRD 3003 TT).

For phase analysis an X-ray powder diffraction system (XRD 3003 TT, GE, USA) with Bragg-Brentano geometry was used. X-ray source was Cu Kα. The parameters are given in table 3.5. For Laue diffraction and high-resolution XRD (rocking curve) an X-ray Diffraction System Galaxy (GE, USA) was used.

Data for single crystal structure determination of Sr_3SiO_5 were collected on an Oxford-Diffraction Xcalibur diffractometer. A CCD area detector (Sapphire S) and a graphite monochromator were used. X-ray source was Mo Kα ($\lambda = 0.071073\,\mathrm{nm}$). Suitable monocrystalline fragments of TSS (undoped and cerium doped) were attached to glass fibers using perfluoropolyalkylether oil and installed in a goniostat. Data were collected at 150 K. CrysAlis CCD was used for data collection, CrysAlisPro for cell refinement and data reduction [117].

Inductively coupled plasma optical emission spectrometry

For elemental analysis (ICP-OES) an IRIS Intrepid HR Duo (Thermo Elemental, USA) was used. Samples were ground, chemically fusion was performed using mineral acids and a microwave (HNO_3,H_3PO_4, 240 °C, 20 min). For the measured samples the limit of quantitation was 0.09 ma.%, the limit of detection was 0.04 ma.%.

High-temperature mass spectrometry

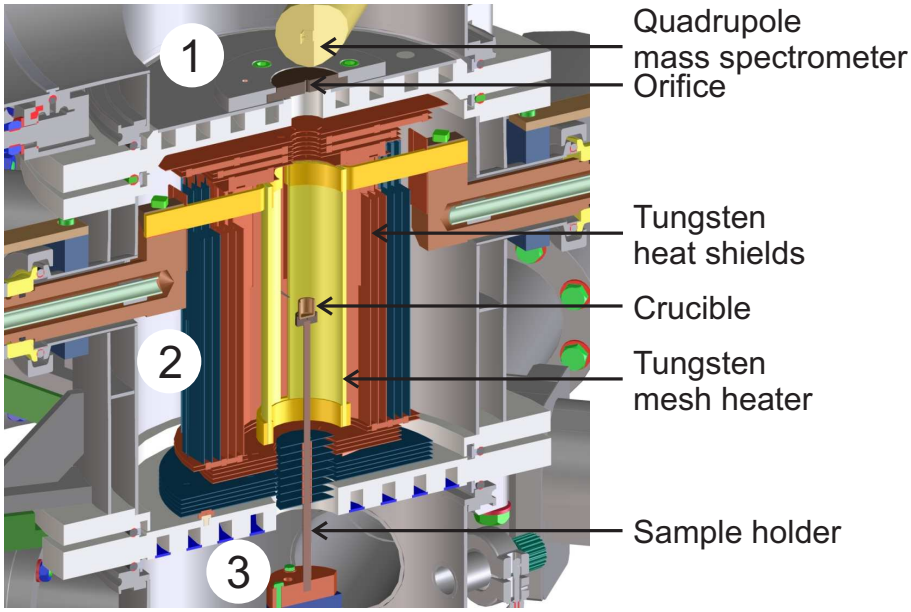

Figure 3.6: CAD model of the tungsten based HTMS system (after [55]). The numbers show different chambers inside the recipient with operating pressures at 10^{-7} mbar (chamber 1) and 10^{-6} mbar (chambers 2 & 3).

The evaporation of components was ex situ investigated with a multifunctional high-temperature mass spectrometer (HTMS), described in detail by Guguschev [55]. Fig. 3.6 shows a CAD model of this system that consists of three separated chambers. Two turbo molecular pumps created a chamber pressure from 10^{-7} mbar (chamber 1) to 10^{-6} mbar (chambers 2 and 3). The sample container is symmetrically surrounded by a resistivity tungsten mesh heater. Tungsten and molybdenum heat shields created thermal insulation (chamber 2). In chamber 1 that is connected to chamber 2 via a 2 mm orifice a quadrupole mass spectrometer (Pfeiffer Vacuum, USA) with a crossbeam ion source detects a representative fraction of evaporating species. Remaining amounts of these species in chamber 2 condense at water-cooled

parts, react with hot tungsten or molybdenum or are pumped out of the system. Under high vacuum conditions (10^{-6} mbar) SCFs were heated up to 2150 °C in an open tungsten crucible. The electron impact energy was set to 70 eV and a secondary electron multiplier voltage of 1300 V was used for signal amplification. The temperature ramps were adjusted manually and temperature was measured with an optical pyrometer. Note that only SCFs were measured with HTMS. Therefore, species that had already evaporated during growth were taken into account.

Electron microscopy

Scanning electron microscopy (SEM) and energy-dispersive X-ray spectroscopy were run by using a FEI Nova 600 DualBeam microscope (FEI, USA). Additionally, samples were investigated using an electron microprobe analyzer (EMPA) at Deutsches GeoForschungszentrum (GFZ Potsdam, Germany). EMPA samples were analyzed using wavelength dispersive X-ray spectroscopy (WDX). Samples for SEM and EMPA were sectioned, embedded in epoxy, ground, and polished (50 nm diamond slurry). With a sputtering device an $\approx 16-24\,\mu$m carbon film coating was attached. Acceleration voltage and beam current were adjusted to 20 kV and 15 nA for EMPA and 15 kV and 0.14 nA for SEM.

Two different microscopes were used for TEM examination. Structural characterization was analyzed with an aberration corrected FEI-Titan 80-300 operated with an acceleration voltage of 300 kV. With this microscope the crystal structure was analyzed by electron diffraction and by high-resolution high-angle annular dark-field imaging in scanning mode (STEM-HAADF). For this method a focused beam (1.3 Å FWHM, semi-convergence angle 9.0 mrad) was scanned across the sample and only electrons with a high scattering angle (< 36 mrad) were collected by an annular detector. For scattering into this angular range the scattering cross-section and therefore the HAADF image intensity correlates with the average effective atomic number Z of the monitored atomic columns. To interpret the TEM results and to analyze the crystal structure of the specimen experimental images were compared with TEM simulations. Therefore a [010] oriented supercell with dimensions of $3 \times 10 \times 30$ unit cells ($\approx 2.9 \times 3.1 \times 33.6$ nm) of the CS2 structure was constructed with the software Diamond™3.0a. Two percent of Ca atoms were randomly substituted by Ce atoms.

For chemical analysis of the sample energy-dispersive X-ray spectroscopy (EDXS) measurements were performed with a JEOL JEM-2200 FS operated with an acceleration voltage of 200 kV and a beam current of 3 nA. The EDXS investigation was carried out in TEM mode by illuminating the specimen (thickness for EDXS measurements ≈ 300 nm) with with a nearly parallel electron beam ($1.5\,\mu$m beam diameter, 0.7 mrad convergence angle). The EDX-spectra were recorded with a X-Flash 5030T silicon drift detector (Bruker Nano GmbH, Germany).

Spectroscopy

Laser luminescence and lifetime measurements were performed by using different laser setups (table 3.6). A nitrogen laser (MNL 200, LTB Lasertechnik Berlin, Germany) with an operating wavelength at 337.1 nm and $\approx 100\,\mu$J pulse energy was used (laser 1). It is noteworthy that only a small fraction of the pulse energy attaches the fiber surface of the samples. In Laser 3 setup the third harmonic of a Nd:YAG

Setup	Laser 1	Laser 2	Laser 3
Type	Nitrogen laser	OPO	Nd:YAG
Wavelength	337.1 nm	450 nm	355 nm (3rd. harm.)
Energy per pulse	$\approx 100\,\mu$J	6-8 mJ	130 mJ
Pulse duration	500 ps	4 ns	6 ns

Table 3.6: Overview of parameters that were used for laser fluorescence and lifetime measurements.

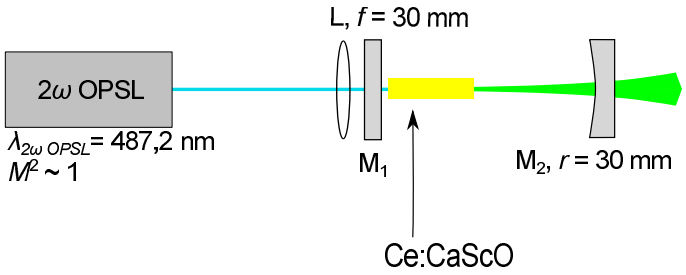

Figure 3.7: Laser experiment outline (Daniel Marzahl, ILP HH). The experiments were performed by Matthias Fechner and Daniel Marzahl (ILP HH).

laser (Brilliant B, Quantel, France) provides stronger pulses (130 mJ) at 355 nm in comparison to laser 1 setup. The YAG laser is pumped by two xenon flash lamps, monopotassium phosphate (KDP) is used for the harmonics generation. In laser 2 setup the nonlinear barium borate (BBO) crystal is used for optical parametric oscillation (OPO-VIS, OPOTEK, USA).

Transmission of plane parallel samples was measured between 190 nm and 2500 nm (Lambda 19 UV/VIS/NIR, Perkin Elmer, USA). Samples were adjusted in front of a 1.0 mm aperture. For some samples an integrating sphere (Ulbricht sphere) was attached to integrate scattering light. The slit width was 5 nm and the measuring time set to 60 nm/min.

Laser experiment

CS2:Ce SCFs have been investigated at the Institute of Laser Physics (ILP HH, University of Hamburg, Germany). Therefore, an experimental setup was built for laser experiments (figure 3.7):

The fibers were attached within a linear resonator. The planar high reflector is reflective for green light and anti-reflective for blue light. The output coupler possesses a 50 mm radius of curvature and 0.3 % reflectivity. The fiber was pumped with a 2 W optical pumped semiconductor laser (OPSL, $\lambda_{\text{laser}} = 478.2$ mm). The pump laser was induced into the crystal fiber using a 30 mm lens. Previous laser experiments with CS2:Ce SFCs, fabricated within this work, were measured at ILP HH by Matthias Fechner, described in detail in [39]. As of this writing, it was not possible to excite and detect stimulated emission with CS2:Ce SCFs (see section 7).

Chapter 4

Phase diagram studies

ID	Composition	m (mg)	$\mathrm{d}T/\mathrm{d}t$ (K/min)	T_m (°C)	Δm (mg)
11	$(CaO)_{0.33}(ScO_{1.5})_{0.67}$	9.29	15	2329	0.29
43	$(SrO)_{0.33}(YO_{1.5})_{0.67}$:Ce	45.29	20	2144	5.42
41	$(SrO)_{0.75}(SiO_2)_{0.25}$:Ce	33.34	20	2203	4.20
44	$(SrO)_{0.75}(SiO_2)_{0.25}$	33.72	20	2196	5.48
1	$(CaO)_{0.33}(ScO_{1.5})_{0.67}$	11.77	15	2212	0.00
3	$(CaO)_{0.32}(ScO_{1.5})_{0.68}$	12.23	15	2273	0.00
4	$(CaO)_{0.29}(ScO_{1.5})_{0.71}$	13.44	15	2277	0.39
5	$(CaO)_{0.27}(ScO_{1.5})_{0.73}$	14.73	15	2282	0.45
6	$(CaO)_{0.24}(ScO_{1.5})_{0.76}$	16.38	15	2285	**4.21**
7	$(CaO)_{0.22}(ScO_{1.5})_{0.78}$	26.16	15	2285	0.15
8	$(CaO)_{0.19}(ScO_{1.5})_{0.81}$	30.75	15	2290	0.42
10	$(CaO)_{0.11}(ScO_{1.5})_{0.89}$	51.09	15	2329	**6.99**
21	$(CaO)_{0.18}(ScO_{1.5})_{0.82}$	19.62	20	2146	0.18
25	$(CaO)_{0.18}(ScO_{1.5})_{0.82}$	22.60	25	2159	0.24
30	$(CaO)_{0.54}(ScO_{1.5})_{0.46}$	18.23	25	2154	0.24
31	$(CaO)_{0.67}(ScO_{1.5})_{0.33}$	18.84	25	2137	0.00
32	$(CaO)_{0.82}(ScO_{1.5})_{0.18}$	20.94	25	2140	0.00
37	(CaO)	23.63	25	2202	0.00

Table 4.1: Overview of the DTA measurements presented in this chapter. Note that the TSS and SY2 samples (ID 43, ID 41) contain $\approx 1\,\%$ cerium substituted on the Y position for SY2 and Sr position for TSS, respectively).

This chapter deals with the thermal analysis and phase relations of the materials. Whereas the phase diagrams SrO-SiO_2 (for TSS) and SrO-Y_2O_3 (for SY2) are already investigated (section 2.3.2), the system CaO-Sc_2O_3 is the subject investigated in this work. HT-DTA of SY2 and TSS crystal fibers, section 4.1, indicated phase relations that can be compared to the CaO-Sc_2O_3. XRD of $(CaO)_x(Sc_2O_3)_{1-x}$ compositions (4.2) indicated no further intermediate phases except of $CaSc_2O_4$. Moreover, lattice constant deviations were calculated to reveal solubilities (4.2). With consecutive HT-DTA of the $(CaO)_x(Sc_2O_3)_{1-x}$ compositions (4.3) the phase diagram CaO-Sc_2O_3 could be approximated. The composition of the DTA samples are given in table 4.1. The sample mass m, the heating ramps $\mathrm{d}T/\mathrm{d}t$, the maximum temperature T_m, and the weight loss Δm are noted for each sample. Note that the weight loss excludes evaporation of CO_2 from $SrCO_3$ and $CaCO_3$. The maximum

temperature is a critical value. It reveals the boundaries for high-temperature DTA. It will be shown that due to the high temperatures and the reactive compositions the measurement is limited by a rapid degeneration of the crucibles and the thermocouples. Each of the HT-DTA measurements was calibrated with DTA of Al_2O_3 with the melting point as a fixpoint. All DTA curves depicted in this chapter possess corrected T values.

4.1 HT-DTA of crystal fibers

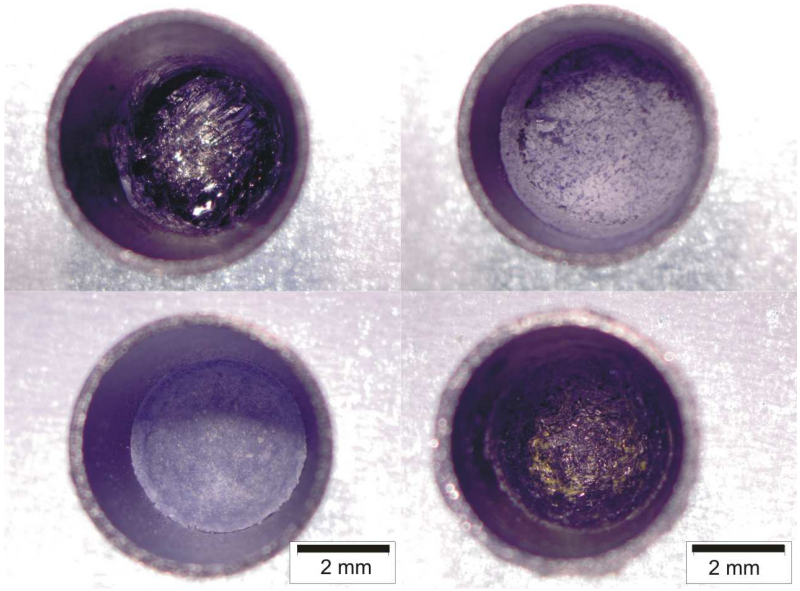

Figure 4.1: DTA crucibles after the measurement: CS2 (top left) was entirely melted, SY2:Ce fibers (bottom right), $(CaO)_{0.67}(ScO_{1.5})_{0.33}$ powder (top right) and TSS:Ce fiber (bottom left) were partially melted.

Figure 4.2 shows three subsequent DTA heating curves of an undoped $CaSc_2O_4$ fiber with identical heating rates about 15 K/min. Cooling curves were recorded, the crystallization peaks appearing there showed some remarkable (several 10 K) but badly reproducible supercooling with respect to the heating peaks. The first heating curve shows the melting point with onset at 2110 °C, in agreement with the value given by Get'man [51]. During the second and third heatings the peak shifts to lower T and its area becomes smaller. Besides, an additional peak with an onset at 1958 °C appears. It was found that mainly Ca evaporates from the sample, consequently the composition shifts to the Sc-rich side of the system CaO–Sc_2O_3. Because no additional intermediate oxide phases except $CaSc_2O_4$ were found in the system (section 4.2), this additional peak is assumed to mark the eutectic point between Sc_2O_3 and $CaSc_2O_4$.

DTA measurement of a SY2:Ce fiber (figure 4.3) did not indicate the melting point of the material. According to the high fugacities f_{Sr} and f_{SrO} (5.1.2) the composition shifts. In curve 1 a liquidus can be marked at ≈ 2103 °C and a eutectic at 1980 °C. During the second and third heating cycles the liquidus peak shifted to lower temperatures and its peak area decreased. Simultaneously, the peak area of the eutectic increased. Compared with the phase diagram of SrO-Y_2O_3 in figure 2.11 the

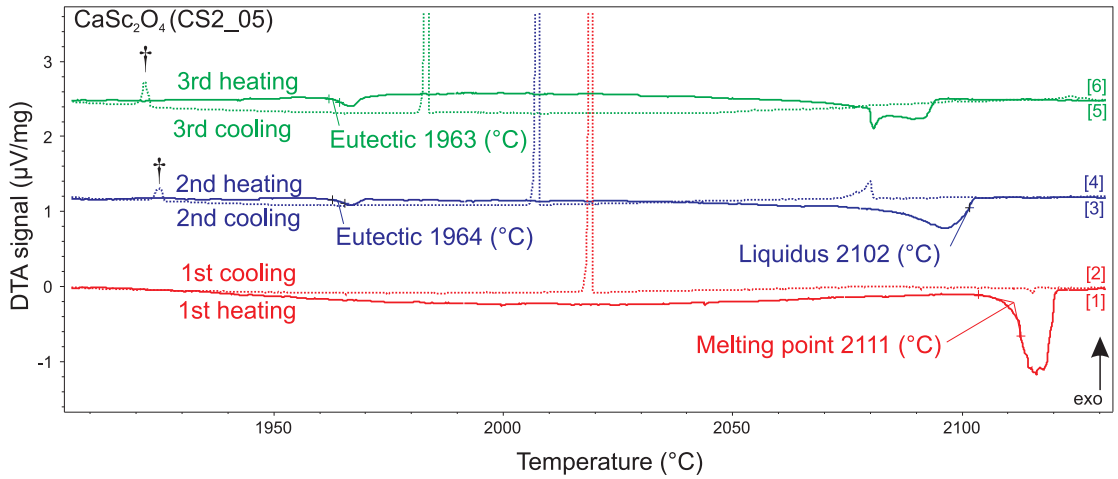

Figure 4.2: Subsequent DTA heating and cooling curves curves of a $CaSc_2O_4$ fiber.

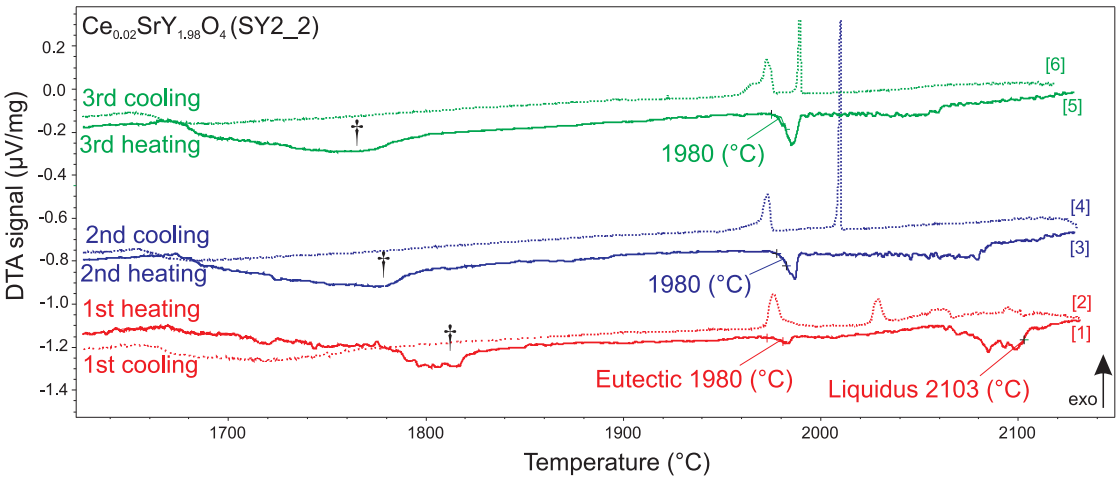

Figure 4.3: DTA heating and cooling curves of a SY2:Ce SCF. The temperature ramps were 20 K/min. † marks a peak that is possibly related to a metastable SrY_4O_7 phase [118].

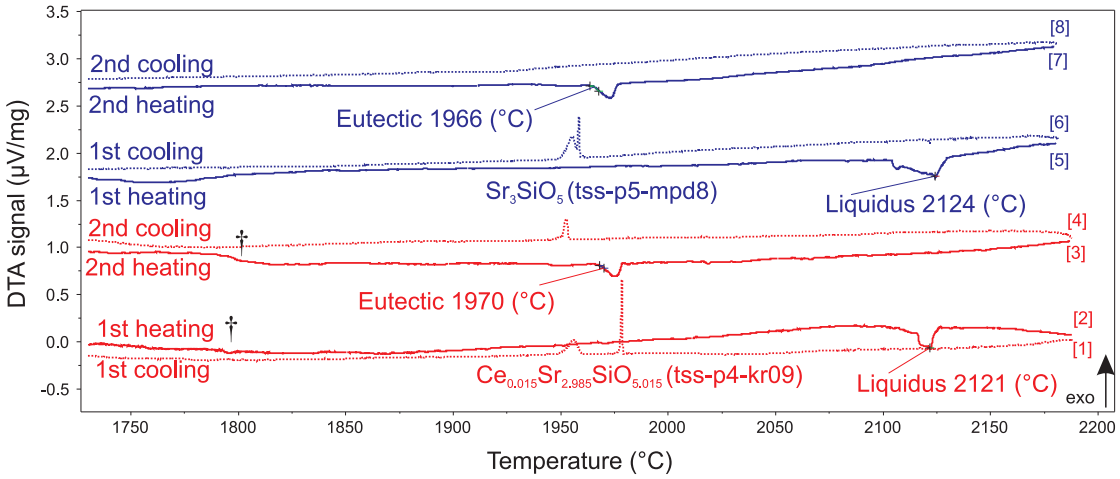

Figure 4.4: DTA heating and cooling curves of a of a cerium doped TSS:Ce fiber (curves 1-4) and a cerium free crystal fiber (curves 5-8). The temperature ramps were 20 K/min.

peaks in figure 4.3 correspond to the liquidus and eutectic point between the phases SrY_2O_4 and Y_2O_3. The determined temperatures for these points are $\approx 100-150$ K lower than the given values in [118] (≈ 2130 °C for the eutectic). This could be related to the influence of cerium or to the degeneration of the tungsten crucible. Taken the mass lost of this measurement into account the composition is shifted to $\approx (SrO)_{0.38}(Y_2O_3)_{0.62}$ that is close to the eutectic composition. An additional peak between 1700 °C and 1800 °C (†) is possibly related to a metastable SrY_4O_7 phase (figure 2.11, [118]). After the experiment the sample mass inside the crucible was fully melted. Therefore, the melting point of the material should be close to 2100 °C. This is in accordance with the melting point that was measured with a pyrometer during LHPG growth.

The melting behavior of the TSS crystal fibers (figure 4.4) can be compared to SY2 (figure 4.3): The heating and cooling curves of two TSS fibers are depicted. The fiber tss-p4-kr09 (figure 4.4, bottom) contains cerium, fiber tss-p5-mpd8 is cerium-free. SrO evaporated and caused a composition shift. Therefore, the liquidus line (2124 °C, curve 5) instead of the melting point is indicated. In general, there are only marginal differences in the cerium doped fiber (1-4). The cerium concentration inside a TSS:Ce crystal fiber is reduced, though, as it is presented in section 5.5.2. During second heating of both samples a eutectic peak at ≈ 1968 °C occurred that fits to the phase diagram SrO-SiO_2, described by Huntelaar et al. [63] (figure 2.12). Similar to the SY2 measurement, the detected eutectic temperature is ≈ 80 K lower than written in literature. Considering this and the composition shift caused by SrO evaporation, the missing of eutectic and liquidus peak in the third heating cycles (not shown here) can be explained: The amount of evaporated SrO caused a composition shift to the described phase Sr_2SiO_4 that melts at ≈ 2315 °C [63] and cannot be melted with the DTA setup. A signal close to the resolution limit can be observed at ≈ 1800 °C ((†), curves 2 and 3). This peak cannot be explained by the cited phase diagram and might be related to incorporated cerium.

Comparing the phase relations for TSS, SY2, and CS2, revealed by this mea-

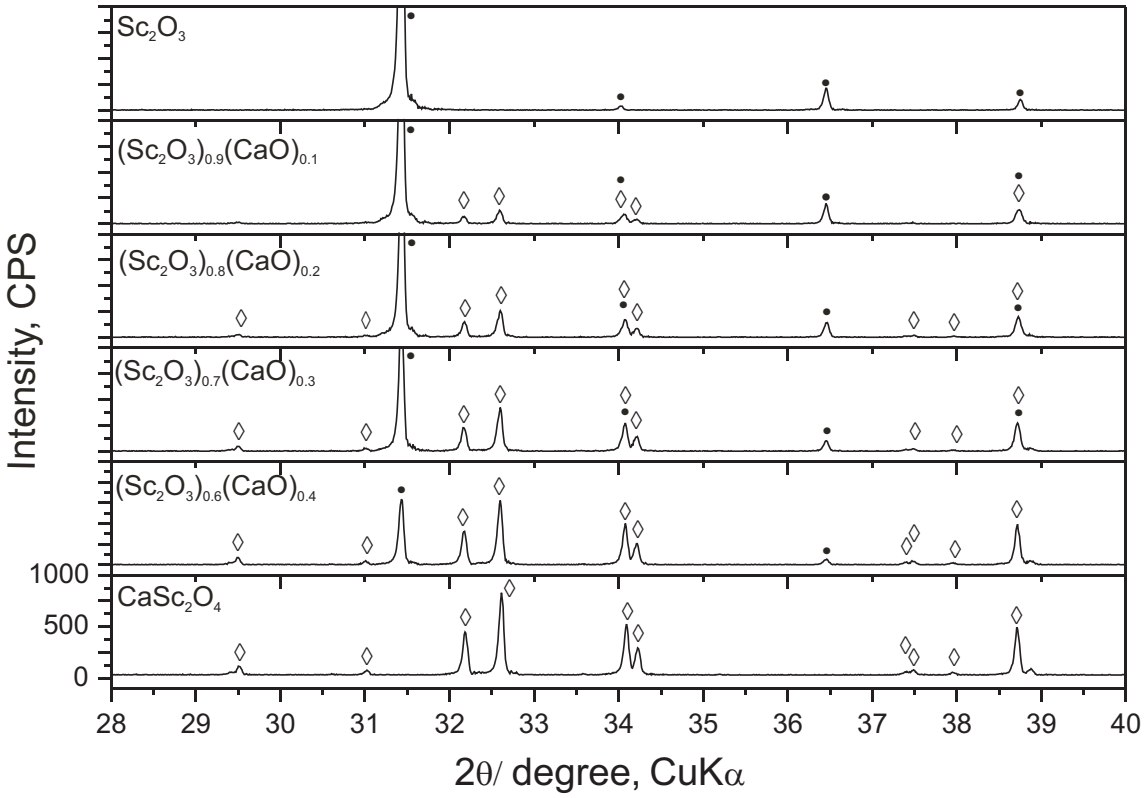

Figure 4.5: XRD patterns of sintered compositions within the range of pure scandium oxide (top) and calcium scandate (bottom). Reflections referring to Sc_2O_3 are marked with •, $CaSc_2O_4$ reflections are marked with ⋄.

surements, the systems SrO-Y_2O_3 and SrO-SiO_2 seem to be more complex than the system CaO-Sc_2O_3. The assumption of a simple eutectic system CaO-Sc_2O_3 has already been noted in [101]. It is vivid, that evaporation will take a major role in the crystal growth of each material.

4.2 Powder XRD of System CaO-Sc_2O_3

Composition samples $(CaO)_x(Sc_2O_3)_{1-x}$ were ground, calcinated and sintered at 1600 °C for 48 h. The figures 4.5 and 4.6 depict the XRD patterns of sintered compositions within the range of pure scandium oxide and calcium oxide/hydroxide. A representative 2θ range between 28 and 40 degrees is given, because it includes the strongest reflections of all relevant phases. Between 10 and 90 degree 2θ all reflections of the compositions correspond to the phases Sc_2O_3 (•), $CaSc_2O_4$ (⋄), CaO (‡) and $Ca(OH)_2$ (†). The intensities of the indexed reflections and those given in the Powder Diffraction Files (PDF, The International Centre for Diffraction Data® (ICDD) [2]) are consistent with each other: Sc_2O_3 (•) to PDF-No. 00-042-1463, $CaSc_2O_4$ (⋄) to 01-072-1360, CaO (‡) to 00-037-1497, and $Ca(OH)_2$ (†) to 00-044-1481 [2]. The patterns of the composition $(CaO)_{0.5}(Sc_3O_3)_{0.5}$ (figure 4.5 (bottom), figure 4.6 (top)) is homogeneous, all reflections (⋄) are indexed as calcium scandate phase $CaSc_2O_4$. A signal at 38.8 2θ is the (131) $K_{\alpha 2}$ reflex of calcium scandate.

Based on the XRD patterns, no evidence for the existence of intermediate phases except of calcium scandate was found. A hypothetical $(CaO)_{0.6}(Sc_2O_3)_{0.4}$ phase,

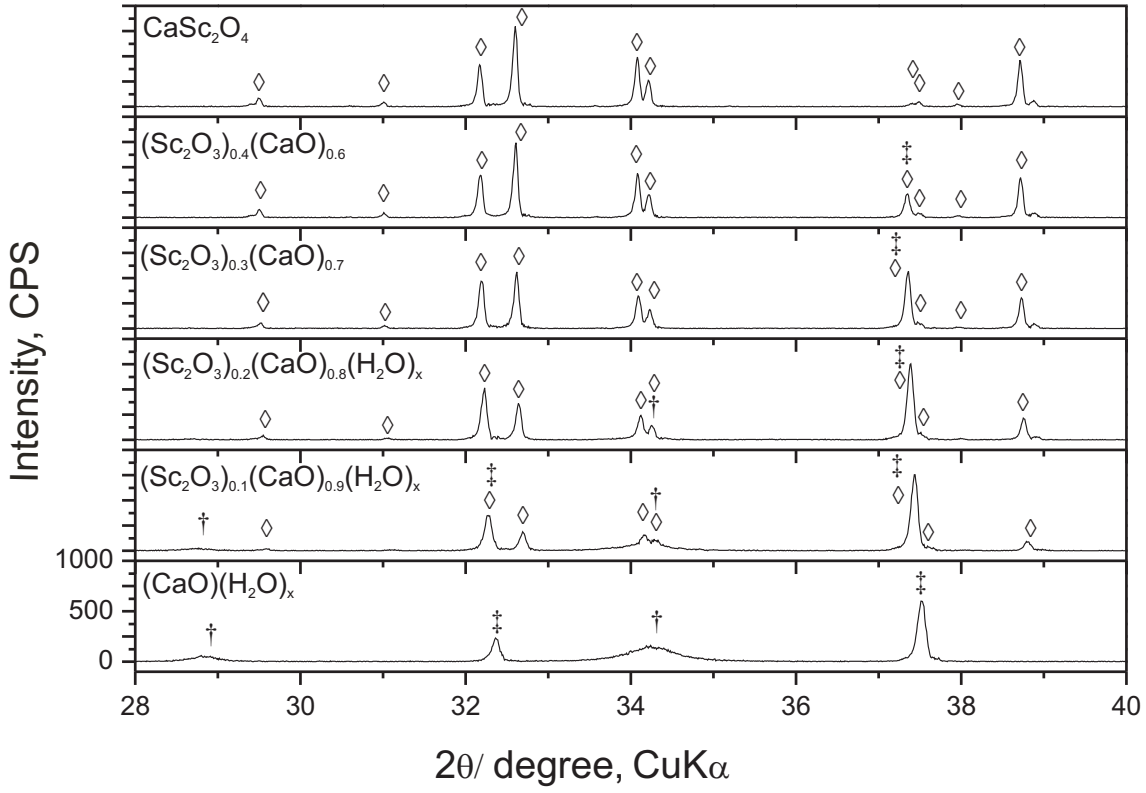

Figure 4.6: XRD patterns of sintered compositions within the range of pure calcium scandate (top) and calcium oxide/calcium hydroxide (bottom). $CaSc_2O_4$, CaO and $Ca(OH)_2$ reflections are marked with ◇, ‡ and †, respectively.

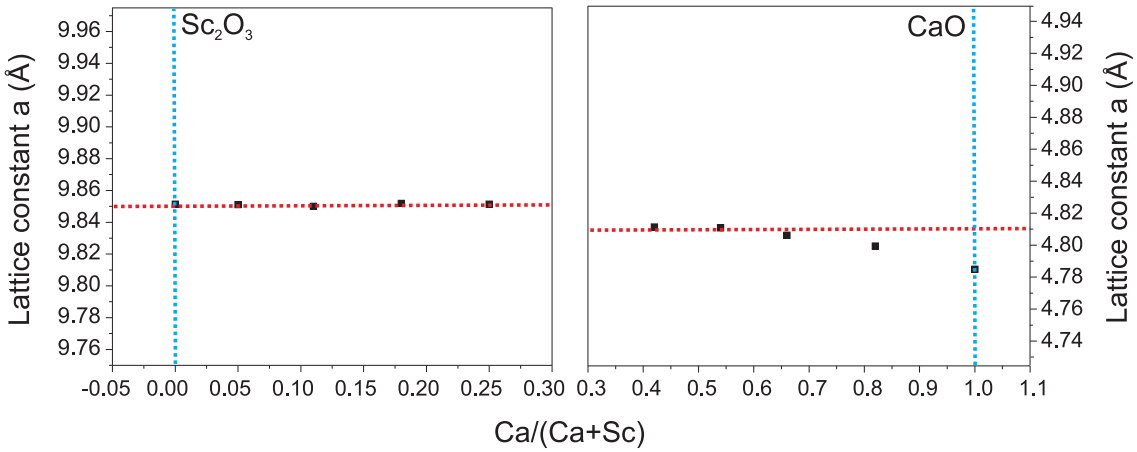

Figure 4.7: Calculated lattice constants a of the cubic CaO and Sc_2O_3 phases dependent on the XRD compositions (figures 4.5, 4.6). The red dashed lines represent the lattice constants given in PDF No. 00-037-1497 (CaO) and PDF No. 00-042-1463 (Sc_2O_3) [2]. The blue dashed lines represent powder compositions of pure CaO and Sc_2O_3.

corresponding to the $(BaO)_{0.6}(Sc_2O_3)_{0.4}$ phase within the system BaO-Sc_2O_3 [76] (figure 2.10), is not present. The calcium rich XRD patterns (figure 4.6 middle to bottom) indicate the formation of both, calcium oxide and calcium hydroxide. The large FWHM values about 0.308 and 0.602 degree 2θ for the calcium hydroxide phase correspond to bonded (OH)-groups. In the following the calculated lattice parameters of the relevant phases are presented.

Lattice constants

The reflections of the diffraction patterns in figures 4.5 and 4.6 were indexed with the Miller indices (hkl) for each phase and reflection. The Miller indices describe lattice vectors of the reciprocal lattice [115]:

$$\vec{r}^* = h\vec{a}_1^* + k\vec{a}_2^* + l\vec{a}_3^* \perp (hkl). \tag{4.1}$$

The reciprocal system ($\vec{a}_i^*$) is oriented to the crystallographic system ($\vec{a}_i$) as follows:

$$\vec{a}_i^* \perp \vec{a}_j, \vec{a}_k (i \in 1, 2, 3). \tag{4.2}$$

Because of $|\vec{r}^*| = 1/d_{hkl}$, with $1/d_{hkl}$ as reciprocal lattice plane distance, the lattice constants can be derived from:

$$1/d_{hkl}^2 = (h^2 + k^2 + l^2)(a_1^*)^2 \tag{4.3}$$

for a cubic crystal structure, and:

$$1/d_{hkl}^2 = h^2(a_1^*)^2 + k^2(a_2^*)^2 + l^2(a_1^*)^2 \tag{4.4}$$

for an orthorhombic crystal structure. The results of lattice constant refinements are given in figure 4.7 for the cubic phases CaO and Sc_2O_3, and in figure 4.8 for the orthorhombic CS2. The lattice constants a, b, c represent a_1, a_2, and a_3 of the crystallographic system ($\vec{a}_i$).

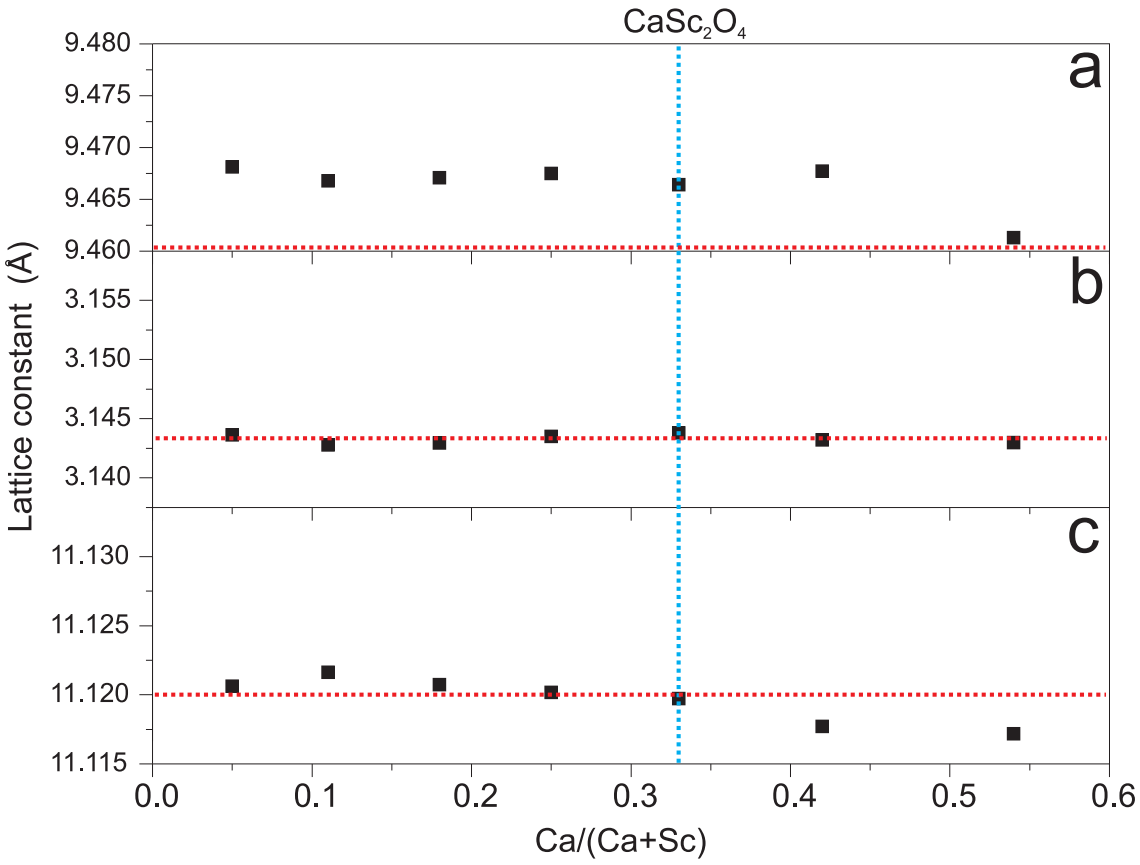

Figure 4.8: Calculated lattice constants a, b, c of the orthorhombic $CaSc_2O_4$ phases dependent on the composition, derived from the XRD compositions (figures 4.5, 4.6). The red dashed lines represent the lattice constants given in PDF No. 00-072-1360 [2]. The blue dashed line represent powder compositions of pure $CaSc_2O_4$.

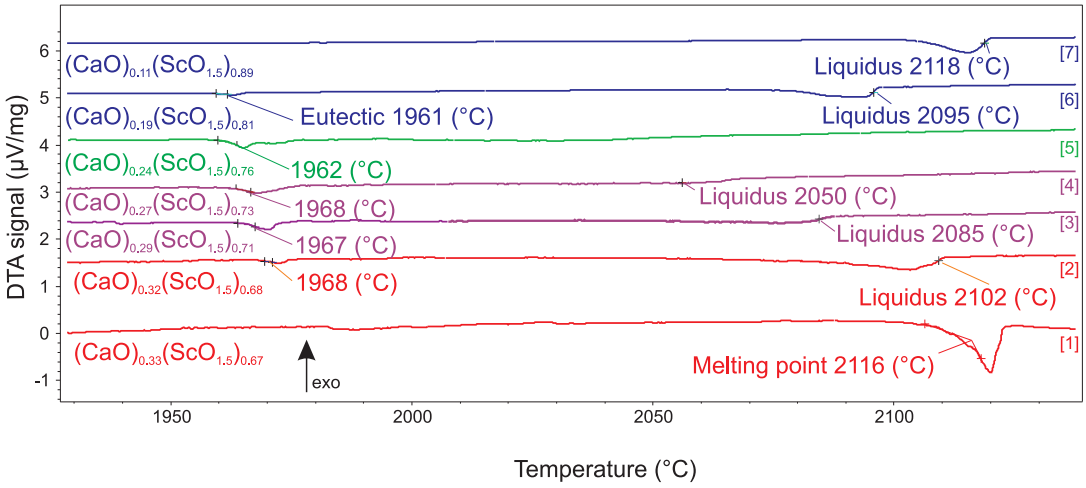

Figure 4.9: DTA heating curves of a CS2 SCF while adding Sc_2O_3 after each measurement (bottom to top). The heating ramps were 15 K/min.

All calculated lattice constants possess large errors (standard deviation, sigma (n-1), not shown here). Because of time limitation a lattice refinement was not performed. The presented values in figure 4.7 and figure 4.8 were not corrected regarding the sample eccentricity and absorption effects. However, some assumptions can be made: The lattice constant of Sc_2O_3, figure 4.7, seems to be independent on the composition. The CaO lattice constant shifts to greater values for scandium-rich samples (4.785 Å to 4.81 Å). Note that the calculated constant a deviates from the value given in PDF No. 00-037-1497 (CaO) [2]. The shift of the CaO lattice constant is associated by a decrease of the $CaSc_2O_4$ lattice constants for calcium-rich samples (figure 4.8, from the blue dashed line of the $CaSc_2O_4$ composition to the right). The lattice constants for scandium-rich compositions do not shift significantly. The shift of the lattice constants probably indicate a solid solution formation $(CaSc_2O_4)_{ss}$ and $(CaO)_{ss}$. This is reported for the system CaO-Y_2O_3 by Du et al. [33, 68]. The authors found a solubility of ≈ 3 at.% Ca in Y_2O_3 up to ≈ 10 at.% Y in CaO. The results in this section are not confirmed. For a precise analysis of the solubilities further work is required. This task is not the purpose of this work. However, the assumption of solubilities fit to the composition shift of the CS2 crystal fibers in section 5.5.2.

4.3 DTA of CaO-Sc_2O_3 samples

High-temperature DTA measurements revealed characteristics for the phase system CaO-Sc_2O_3. Figure 4.9 depicts the heating curves of a CS2 SCF. The curve of the pure fiber is shown at the bottom of the diagram (curve 1). After each measurement, Sc_2O_3 powder was added to the crucible. The resulting composition is given for each curve. The pure fiber melted at $\approx 2116\,°C$, characterized through the peak onset. After adding a small amount of scandium oxide the composition shifted to $(CaO)_{0.32}(ScO_{1.5})_{0.68}$. A new peak occurred at $\approx 1968\,°C$. The peak area of the melting point decreased and deviated to smaller temperatures ($\approx 2102\,°C$). As the XRD measurements of sintered powder samples (4.2) did not indicate additional phases

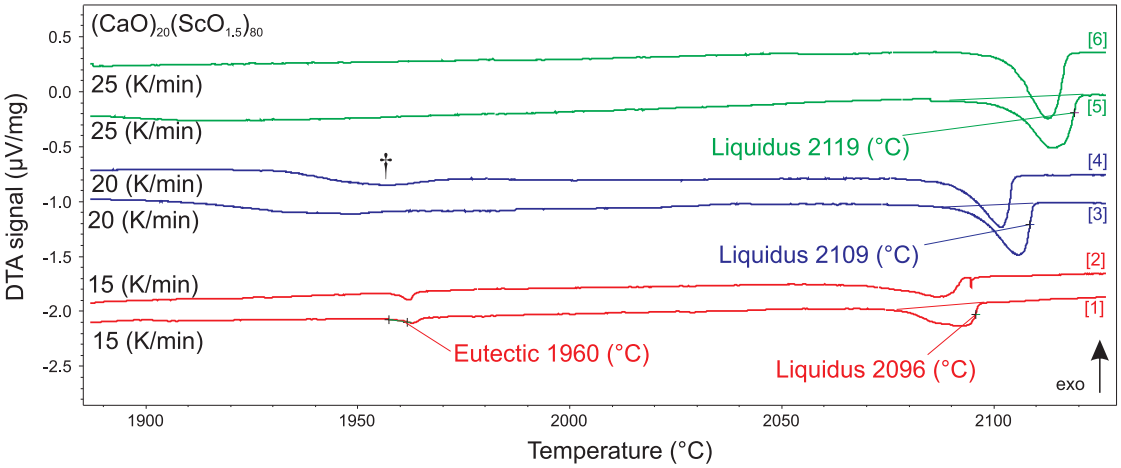

Figure 4.10: First and second heating of three samples with the composition $(CaO)_{0.2}(ScO_{1.5})_{80}$. The samples were measured with 15 K/min (curve 1 and 2), 20 K/min (curve 3 and 4), and 25 K/min (curve 5 and 6).

between pure Sc_2O_3 and $CaSc_2O_4$, the system indicate a typical eutectic behavior between both phases: By adding Sc_2O_3 to the system, the resulting liquidus of the system shifts to smaller temperatures; its peak area decreases. Simultaneously, the peak area of the eutectic peak increases and reaches a maximum at the composition $(CaO)_{0.27}(ScO_{1.5})_{0.73}$ (curve 4). In this curve, the liquidus peak is shifted to $\approx 2050\,°C$. In the following curve 5 no liquidus peak can be detected. Therefore, we mark a eutectic point:

$$E_{Sc_2O_3-CaSc_2O_4} \approx 1965 \pm 5\,°C. \tag{4.5}$$

The eutectic point is invariant within a two component system. Small deviations are caused by degeneration of the thermocouples and the tungsten crucibles. For the thermocouples a temperature shift of $\approx$ 4 K per heating cycle was approximated. The eutectic composition is located between the maximum of the eutectic peak area ($(CaO)_{0.27}(ScO_{1.5})_{0.73}$) and the minimum of the liquidus peak area ($(CaO)_{0.24}(ScO_{1.5})_{0.76}$). After the eutectic point is exceeded the liquidus of the system is increasing (curves 6, 7). Even if the crucibles are partly corroded by reactive Ca^{2+} ions, we can mark the eutectic composition within the above mentioned region. The mass lost caused by evaporation of mainly CaO (5.1.1) reached a maximum at the eutectic composition (curve 5).

4.3.1 Influence of the DTA heating rate

Two effects are obstacles for high-temperature DTA measurements of the materials in this work: 1. The rapid degeneration of the tungsten crucibles by reactive Sr^{2+} and Ca^{2+}. 2. The strong evaporation of mainly SrO and CaO. Both effects can be reduced by rapid DTA heating ramps. Figure 4.10 demonstrates the influence of heating velocity on the DTA signals. Three samples with the same composition $(CaO)_{0.2}(ScO_{1.5})_{80}$ were measured with 15 K/min (curve 1 and 2), 20 K/min (curve 3 and 4), and 25 K/min (curve 5 and 6). Curve 1 and 2 show the eutectic $E_{Sc_2O_3-CaSc_2O_4}$ at $\approx$ 1960 °C and the liquidus line at $\approx$ 2096 °C. When the heat-

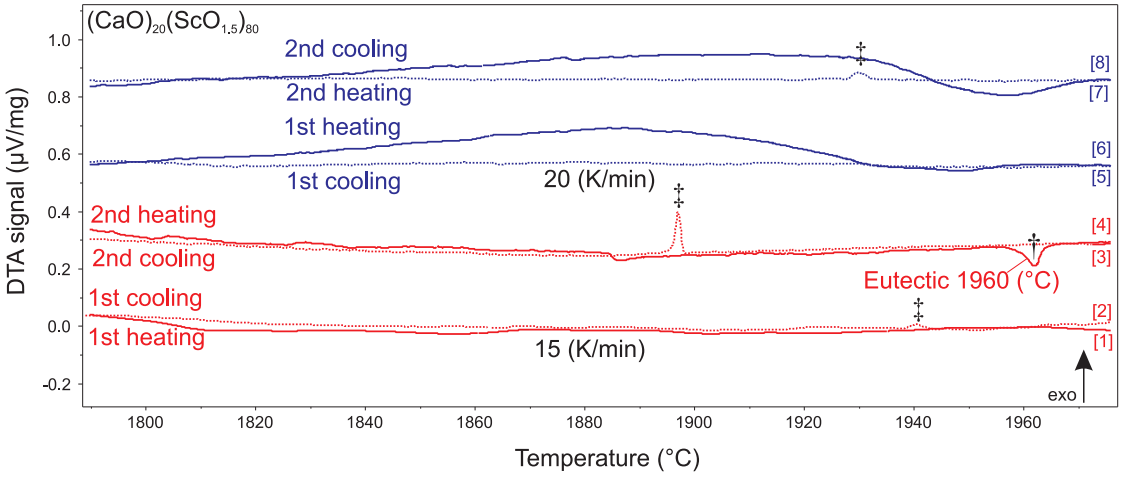

Figure 4.11: First and second heating and cooling curves (dotted) of two samples with the composition $(CaO)_{0.2}(ScO_{1.5})_{80}$. The samples were measured with 15 K/min (curve 1-4) and 20 K/min (curve 5-8).

ing ramp is altered to 20 K/min (25 K/min), the liquidus shifts to higher temperatures ≈ 2109 °C (≈ 2119 °C). Its peak area increases: -8.907 μVs/mg at 15 K/min, -12.420 μVs/mg at 20 K/min, -13.55 μVs/mg at 25 K/min. This is in accordance with [61]. The eutectic peaks are affected diametrically. The peak area is reduced and cannot be detected when using high temperature ramps. A peak near the resolution limit is marked (†). Nevertheless, when working with high temperature ramps, eutectic peaks can be detected when adding cooling curves. This is demonstrated in figure 4.11: A eutectic peak (‡) arising from the heating curves could only be detected in curve 3, when a $(CaO)_{0.2}(ScO_{1.5})_{80}$ sample was heated, the second time with 15 K/min. The cooling curves of the samples (curves 2, 4, and 8) reveal peaks that correspond to the eutectic point (‡). Even if the first heating did not show a eutectic peak (curve 1), its cooling curve indicated the eutectic. Moreover, when heating with high temperature ramps, the eutectic peak could be indicated (curve 8, ‡) after the second heating. This implies, the cooling curves are important for the determination of phase diagram studies with high-temperature DTA, however, the temperature of the cooling curve peaks may vary due to supercooling effects.

For a further understanding of the phase relations CaO-Sc_2O_3 a combination of measurements with different heating ramps is presented. The discussions of the DTA results will take all the differences caused by evaporation, supercooling, and degeneration into account.

4.3.2 The CaO-$CaSc_2O_4$ system

The measurement of the calcium-rich side of the phase system CaO-Sc_2O_3 is more challenging. Because of the high calcium fugacity f_{Ca} the weight loss during DTA measurements was higher. But through high temperature ramps and reducing the maximum temperature, the weight loss could be minimized. This is shown in figure 4.12: By raising the temperature ramps to 25 K/min and by reducing T_{max} to 2130 °C the shift of the melting peak is only 8 K , instead of the high composition

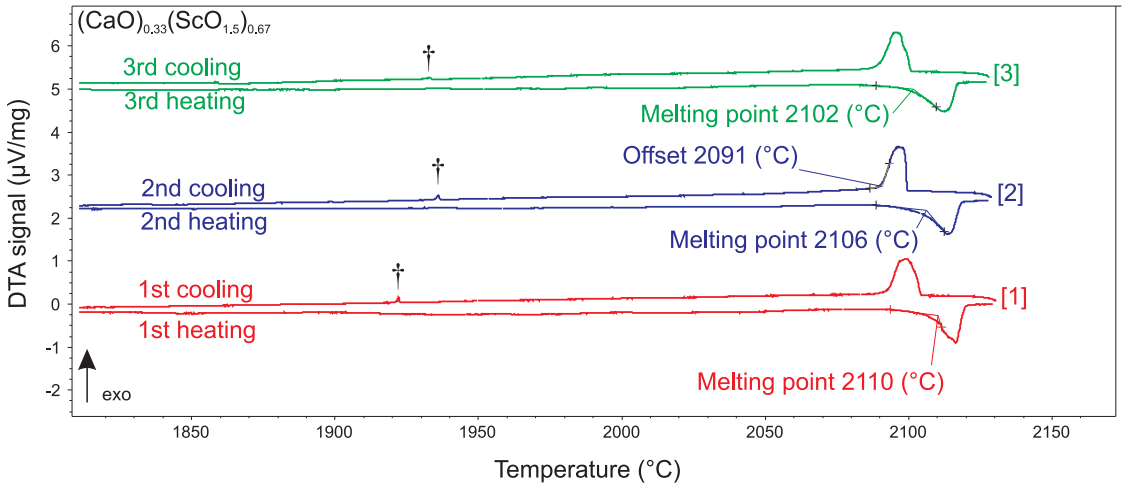

Figure 4.12: DTA heating and cooling curves of a $(CaO)_{0.33}(ScO_{1.5})_{0.67}$ powder sample. The heating ramps were 25 K/min.

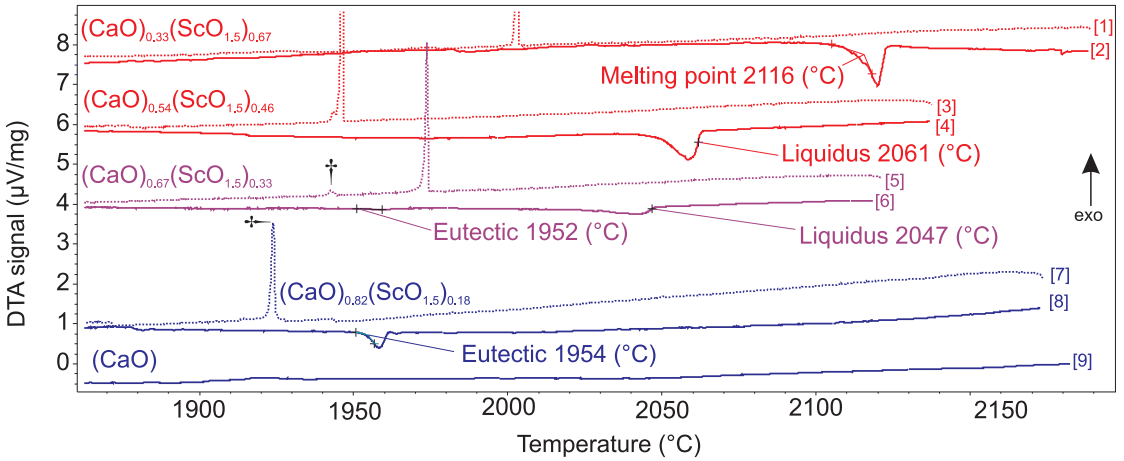

Figure 4.13: DTA heating curves and cooling curves (dotted) of a CS2 SCF (top) and compositions CaO-$CaSc_2O_4$. The heating ramps were 25 K/min.

shift in previous measurements [101]. This shift is mainly caused by the degeneration of the thermocouples and the crucible, the weight loss is of this sample was only evaporating CO_2 (calcination). The supercooling is $\approx 15\,°K$. The cooling curves being more sensitive than the heating curves reveal the eutectic $E_{Sc_2O_3-CaSc_2O_4}$ (†) and indicate a small shift of the composition.

Because of this shift the phase relations on the calcium-rich side of the system CaO-$CaSc_2O_4$ could not be determined exactly. Figure 4.13 depicts CaO-$CaSc_2O_4$ DTA curves that were measured under 25 K/min T ramps. Curve 1 and 2 (top) are DTA signals of the SFC that is also shown in figure 4.9. From top to the bottom of the diagram the calcium content of the samples is enhanced. In contrast to figure 4.9 every sample was measured in a new crucible to avoid weight loss and crucible degeneration. The weight loss is mainly CO_2. The resulting weight loss is close to zero (4.1). In accordance with the scandium-rich side of the phase system CaO-Sc_2O_3 the liquidus drops when additional calcium is added (curve 4 and curve 6). The curve 5 demonstrates the significance of the cooling curves for detection of the eutectic composition: Heating of a $(CaO)_{0.67}(ScO_{1.5})_{0.33}$ sample (curve 6) showed a minimum of the liquidus peak area at (2047 °C). The eutectic at ($\approx$ 1952 °C) is not clearly visible, however, the cooling curve 5 indicates an occurrence of an additional peak (†) that refers to the eutectic. The following sample (curves 7 and curve 8) mark the eutectic point

$$E_{CaO-CaSc_2O_4} \approx 1953 \pm 5\,°C \tag{4.6}$$

with an eutectic composition that is close to $(CaO)_{0.82}(ScO_{1.5})_{0.12}$.

The XRD measurements of sintered compositions CaO-Sc_2O_3 did not indicate any phases except the intermediate phase $CaSc_2O_4$. The high-temperature DTA measurement within the phase system point to a eutectic point at either side of the calcium scandate phase. As described in the characterization chapter 3.3 the accuracy of high-temperature DTA curves are limited. In this section it could be shown that despite of these limitations characteristics of a phase systems with melting points above 2000 °C can be determined.

4.3.3 Heat capacity of calcium scandate

For the thermodynamic assessment of the system CaO-Sc_2O_3 the heat capacity (at constant pressure) $C_p(T)$ of calcium scandate has been determined using differential scanning calorimetry (DSC). Figure 4.14 shows the average $C_p(T)$ values of four DSC measurements for a calcium scandate SCF (CS2_03). The fitted function led to

$$C_p = 140.5441 + 0.0272T - 1.462047 \times 10^{-6}\ T^{-2}. \tag{4.7}$$

This function resembles the $C_p(T)$ of strontium yttrium oxide, reported by Kurosaki et al. [79]

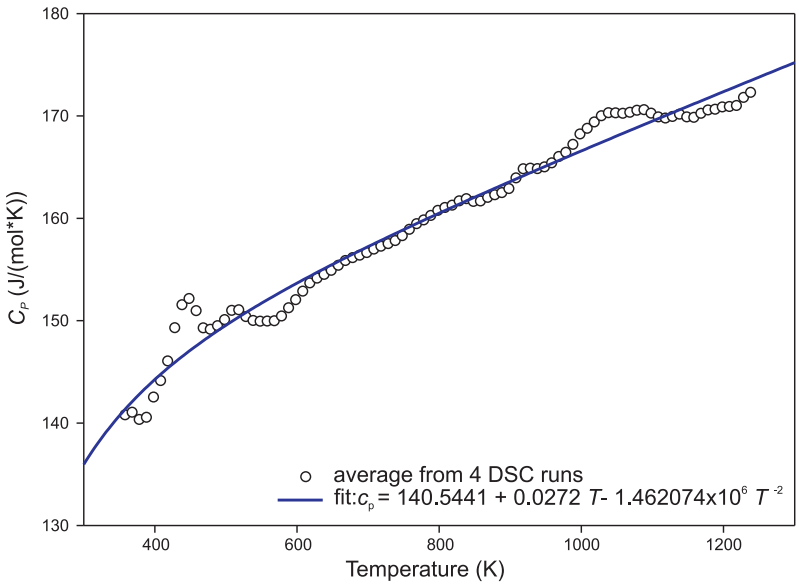

Figure 4.14: Heat capacity (at constant pressure) of a CS2 SCF as a function of the temperature.

Chapter 5

Fiber crystal growth

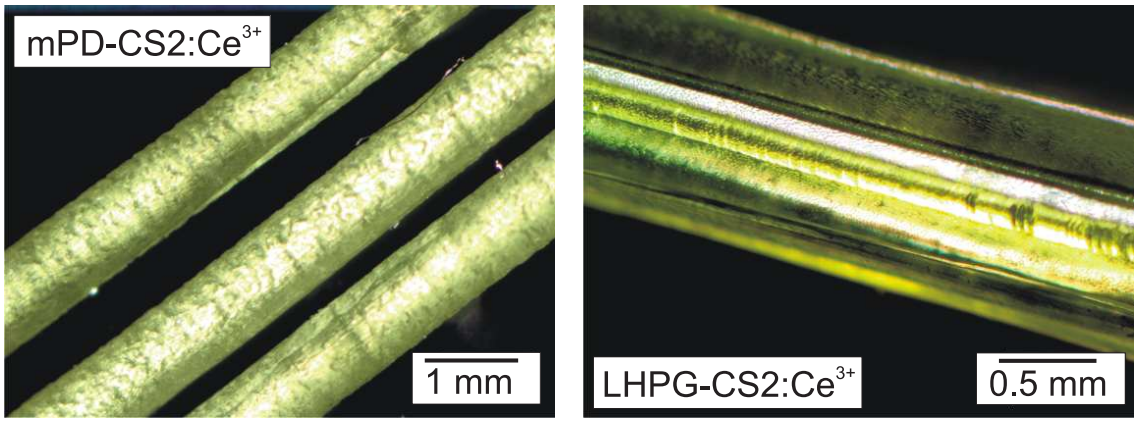

Figure 5.1: Two single crystal fibers of CS2:Ce. The left fiber was grown using micro-pulling-down method. The right fiber was grown using laser-heated pedestal growth (right) with optimized growth conditions (table 5.3).

This chapter summarizes the fiber crystal growth of cerium doped (and Ce-free) $CaSc_2O_4$, SrY_2O_4, and Sr_3SiO_5. The main part of this chapter deals with the investigation of cerium doped calcium scandate fibers that were grown using the LHPG technique, as shown in figure 5.1 (right). The pictured fiber was crystallized using optimized growth conditions (section 5.3) and is homogeneous and monocrystalline (sections 5.4, 5.6). Luminescence and absorption results will show that the major amount of cerium inside this fiber is trivalent (5.8). In contrast to the even surface of the LHPG fiber, the mPD fiber, figure 5.1 (left), has got a rough surface. This is generated by Ca evaporation and condensation at the crystallization interface (section 5.5). The discussion will show that LHPG is superior to mPD technique regarding the crystal growth of CS2:Ce. The optimized growth conditions for CS2:Ce SCF are given in table 5.3.

Strontium yttrium oxide was grown with the same crystal growth conditions as calcium scandate. Yellow-orange colored fibers, figure 5.2, show homogeneous extinction between cross-polarized light. The color arises from trivalent cerium, as the absorption measurement will show (section 5.8). The materials properties are similar to CS2:Ce, despite trivalent cerium is presumably incorporated onto the Y position instead of the alkaline earth metal position (Sr and Ca, respectively). Because of stronger Sr evaporation, in comparison to Ca evaporation, the fiber

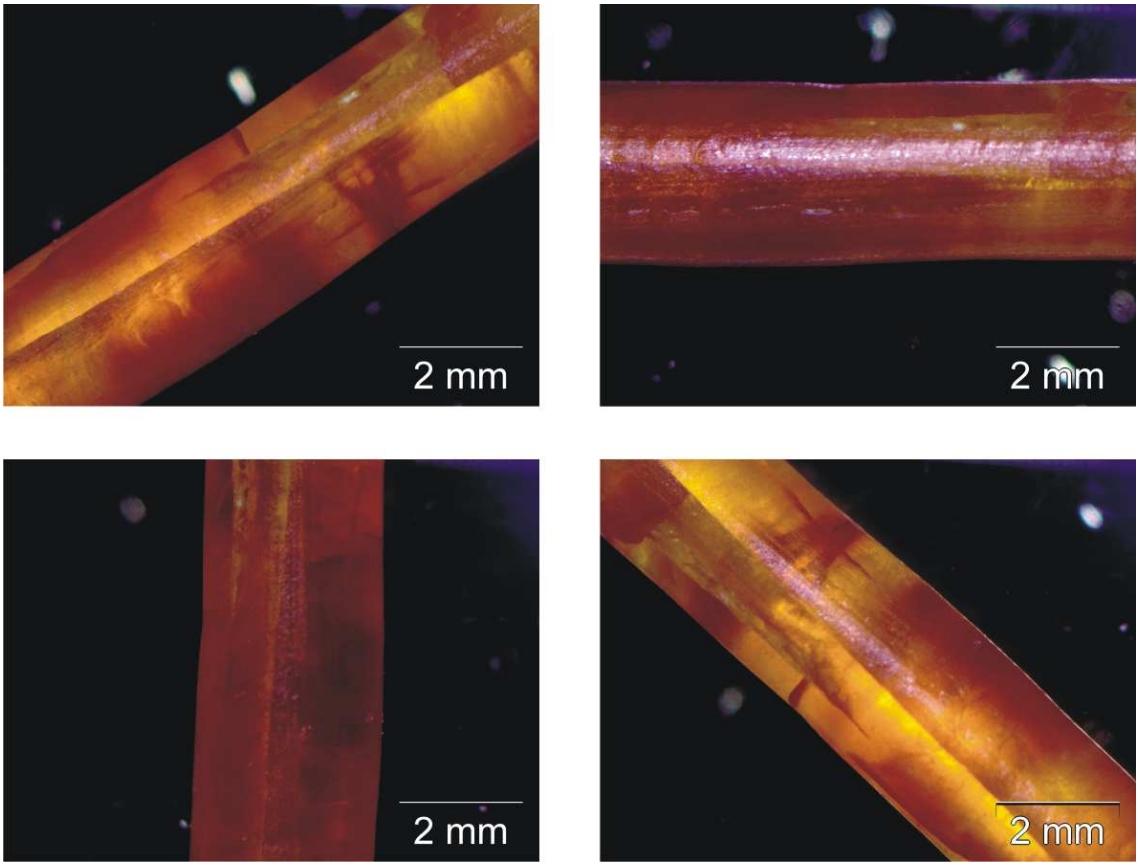

Figure 5.2: A yellow-orange SY2:Ce SCF shows homogeneous extinction between cross-polarized light. We used the same parameters as for the optimized calcium scandate growth (table 5.3).

crystal growth of SY2 and TSS is more challenging. Monocrystalline TSS fibers could only be fabricated using mPD technique, as depicted in figure 5.3. Both fibers, the cerium-free (left) and cerium doped (right), contain single crystalline segments that could be used for structure analysis. The results are presented in section 5.6.3. Prior to the crystal growth experiments the following two sections summarize the thermodynamic conditions during crystal growth.

5.1 Calculation of growth conditions

A thorough study of the thermodynamic conditions and phase relations during LHPG and mPD growth is advantageous for finding suitable crystal growth conditions. More precisely, the calculated fugacities f_i point out possible evaporating species as well as their quantities. These lead to composition deviations of the SCFs that are presented in section 5.5. By comparing the calculations with the kinetic HTMS measurements and equilibrium-near growth experiments, an overview of the mass flows during the crystallization process can be given. Despite of the evaporation, the cerium valence is affected by the chemical nature of the atmosphere, described in figure 5.4:

No atmosphere is free of oxygen. Even for a technical gas with 5 N purity the residual gas supplies a background of typical $f_{O_2} \approx 2 \times 10^{-6}$ bar (see Tab. 3.2).

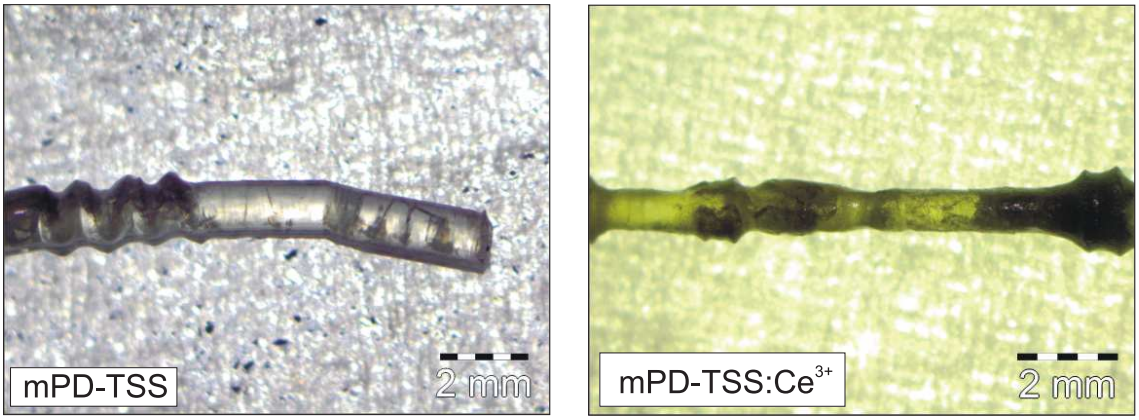

Figure 5.3: Cerium-free (left) and cerium doped (right) crystal fibers of tristrontium silicate. Both fibers contain monocrystalline fragments.

For the incorporation of trivalent cerium into the fiber the oxygen fugacity must be located within the stability region of Ce_2O_3. In figure 5.4, this region has an upper limit $< 10^{-20}$ bar at 1000 °C and extends to almost 0.1 bar at the maximum $T = 2400$ °C shown there. If $f_{O_2}(T)$ exceeds these limits, the higher oxides $Ce_{18}O_{31}$, Ce_6O_{11}, or even CeO_2 will be formed which contain less or no Ce^{3+}. It is desirable, to remain in the Ce^{3+} phase fields not only at the growth temperature and slightly above (because the melt zone is overheated), but also at lower T, because even if Ce^{3+} is stable at T_f, it might be subsequently oxidized at lower T, when the grown fiber is removed from the melt zone.

The reducing atmosphere III (3.2) meets this condition over a wide temperature range, and consequently fiber growth in this atmosphere is preferable with respect to the Ce^{3+} content. The inert atmosphere (5N Ar) and reducing atmosphere I (5N N_2) are less advantageous regarding the valence of cerium, but hold down to several 100 K below T_f. The less significant drop of $f_{O_2}(T)$ also for Ar results from the partial dissociation of O_2. If an identical residual gas impurity $p_{O_2} = 2 \times 10^{-6}$ bar is assumed for both gases, nitrogen will be superior to argon, because at high T f_{O_2} is reduced due to the formation of nitrogen oxides (mainly NO). Oxidizing atmospheres do not cross the stability region of Ce_2O_3 (figure 5.4), but reduce the evaporation, especially of calcium and strontium. This aspect will be demonstrated in in the following section. The Ce–O_2 predominance diagram is adapted for the crystal growth of all three relevant materials inside this work grown either with LHPG or mPD technique.

5.1.1 Growth conditions for CS2:Ce

Several restrictions of these equilibrium calculations have to be acknowledged, for the LHPG these are: 1. Only a small volume of the system is at the estimated melt zone temperature of 2250 °C. 2. Within the melt zone there is a high temperature gradient (figure 3.4). 3. Because of the high growth rates, the system might not be in perfect equilibrium. Other than LHPG, mPD technique means direct pulling from a melt (section 2.1.5). Therefore, the whole material is liquid. Smaller temperature gradients and pulling rates shift the system closer to equilibrium, however, due to the very high temperatures in both systems, mPD as well as LHPG, might be

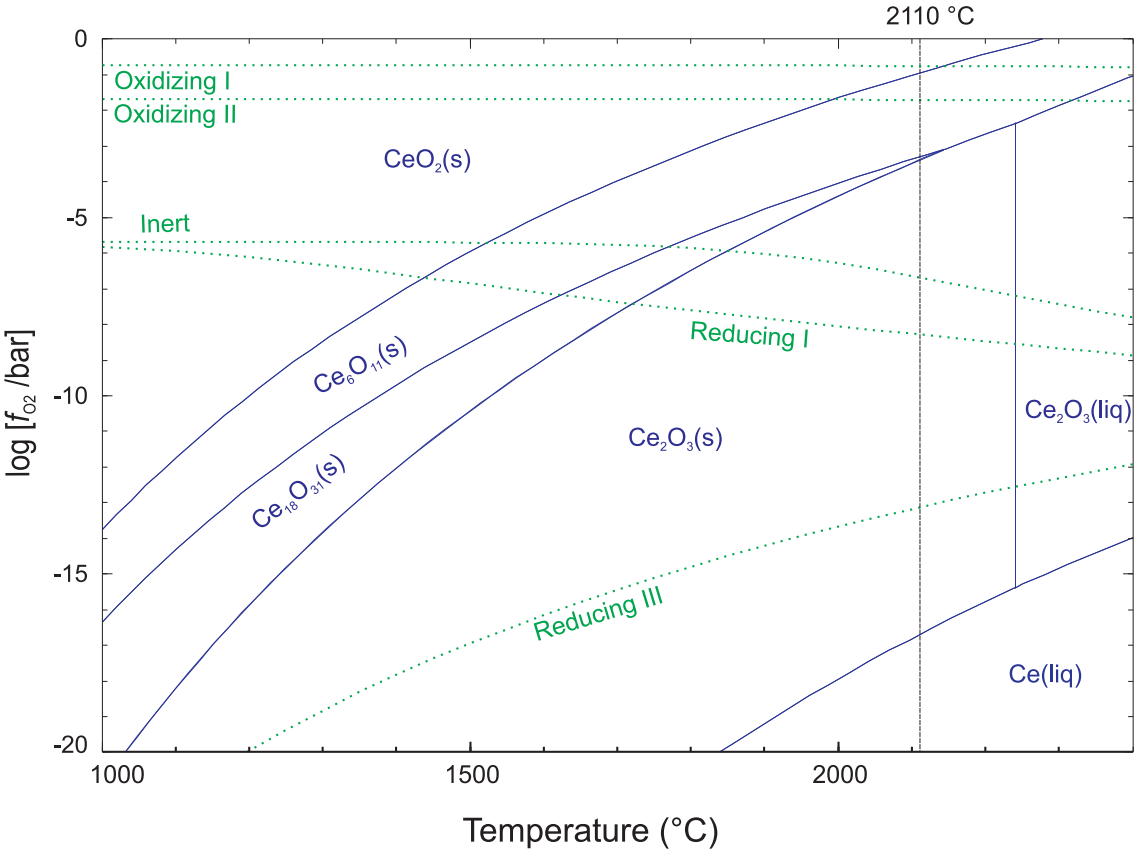

Figure 5.4: Predominance diagram Ce–O_2 (blue solid lines) showing the stability regions of Ce and its oxides as functions of oxygen fugacity f_{O_2} and temperature T. The green dotted lines show the $f_{O_2}(T)$ that are supplied by different atmospheres used during LHPG growth. The dashed vertical line indicates the melting point of calcium scandate $T_f = 2110\,°C$ [101].

considered as equilibrium-near.

Table 5.1 summarizes the fugacities f of a CS2:Ce melt at 2250 °C in different atmospheres. These atmospheres were used in LHPG and mPD setups. Only fugacities with a maximum value $\geq 1.0 \times 10^{-8}$ are shown here. We assume that lower fugacities do not affect the growth process. Although the amount-of-substance ratio $(n_{melt}/n_{atmosphere})_{lhpg}$ and $(n_{melt}/n_{atmosphere})_{mpd}$ differed from each other, the calculated fugacities did not change significantly. According to table 5.1 metallic Ca and CaO can be expected as the main evaporating species. While the fugacities of CaO and ScO only show minor changes with respect to the atmosphere, the values of the other species change significantly. The strongest evaporation might be under reducing conditions (reducing III). Therefore, the composition of a SCF should deviate to lower values of Ca and Ce. For inert gases the fugacity of CeO is almost two orders of magnitude smaller than Ca, but the initial Ce content within the fiber is also two orders of magnitude smaller. Therefore, a comparable deficit of Ca and Ce within the fibers can be expected.

We want do discuss the deviations in crystal fibers using elemental analysis and HTMS. It is necessary to consider the different p and T values: The ambient pressures for HTMS and LHPG/mPD are $\approx 1.0 \times 10^{-7}$ bar and 1 bar, respectively. Figure 5.5 shows the fugacities depending on the temperature for both pressures.

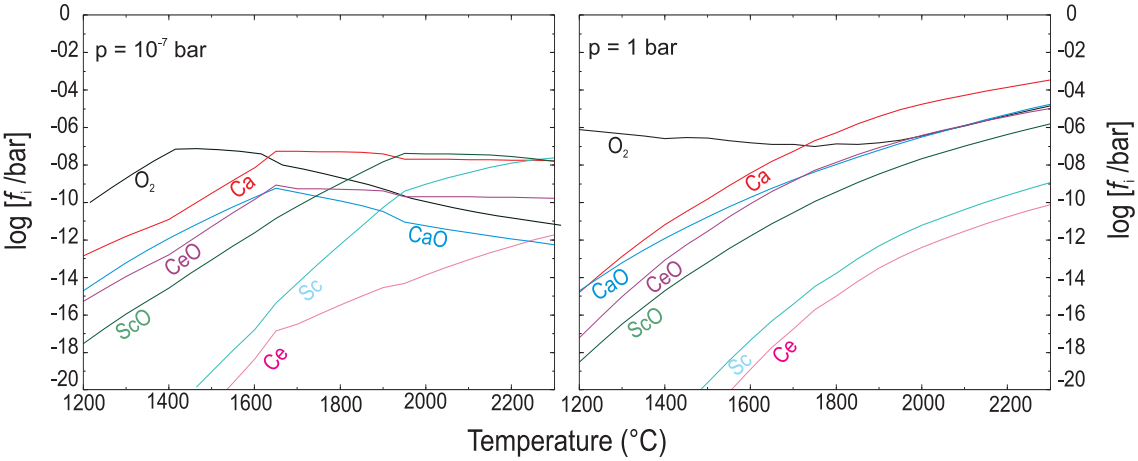

Figure 5.5: Calculated fugacities f_i of a CS2:Ce composition as functions of the temperature, given for different pressures referring to a HTMS setup ($\approx 1.0 \times 10^{-7}$ bar) and referring to LHPG/mPD setup (1 bar).

Atm.	Fugacities (bar)				
	Ca	CaO	ScO	CeO	CaOH
Oxidizing I	1.4×10^{-6}	9.3×10^{-6}	6.4×10^{-8}	2.8×10^{-7}	-
Oxidizing II	4.6×10^{-6}	9.3×10^{-6}	1.2×10^{-7}	7.5×10^{-7}	-
Inert	1.2×10^{-4}	9.3×10^{-6}	6.1×10^{-7}	4.8×10^{-6}	-
Reducing I	2.2×10^{-4}	9.3×10^{-6}	8.1×10^{-7}	6.4×10^{-6}	-
Reducing II	9.0×10^{-4}	9.3×10^{-6}	1.6×10^{-6}	1.0×10^{-5}	6.8×10^{-5}
Reducing III	9.5×10^{-4}	1.9×10^{-6}	3.7×10^{-6}	9.9×10^{-6}	3.4×10^{-5}

Table 5.1: Fugacities f_i of species evaporating from the CS2:Ce melt at 2250 °C in different atmospheres. A background oxygen fugacity of $f_{O_2} = 2 \times 10^{-6}$ bar was added always [101].

Both diagrams are similar to each other regarding the species sequence and their ratios over a long temperature range. There are some changes at temperatures above 1650 °C, f_{CaO} and f_{CeO} slopes are reduced. Note that under vacuum conditions f_{ScO} will show the highest value, if the temperature increases 1850 °C. At higher temperatures, the fugacities for the vacuum condition reach a plateau, because the total amount $\sum(f_i)$ must not exceed the total pressure.

5.1.2 Growth conditions for SY2:Ce and TSS:Ce

Compared to the CS2:Ce system some similarities for the SY2:Ce fugacities can be marked (table 5.2). The alkaline earth metals (Sr) and its oxide species (SrO, Sr_2O) seem to be the main evaporating species. Through an increased oxygen partial pressure (oxidizing II), the fugacity of metallic Strontium is lowered. The values for the REE single oxides (CeO, ScO, YO) are similar. The total amount of the fugacities for a SY2:Ce melt is higher than for the CS2:Ce melt. A stronger shift of composition will be expected, if SY2:Ce is crystallized analogously to the CS2:Ce conditions. f_i as functions of the temperature are depicted in figure 5.6, which is similar to figure 5.5. Strong evaporation of the alkaline earth metal and its oxides can be expected. Because of $f_{SrO}/f_{CeO} \approx f_{CaO}/f_{CeO}$. Therefore, similar cerium

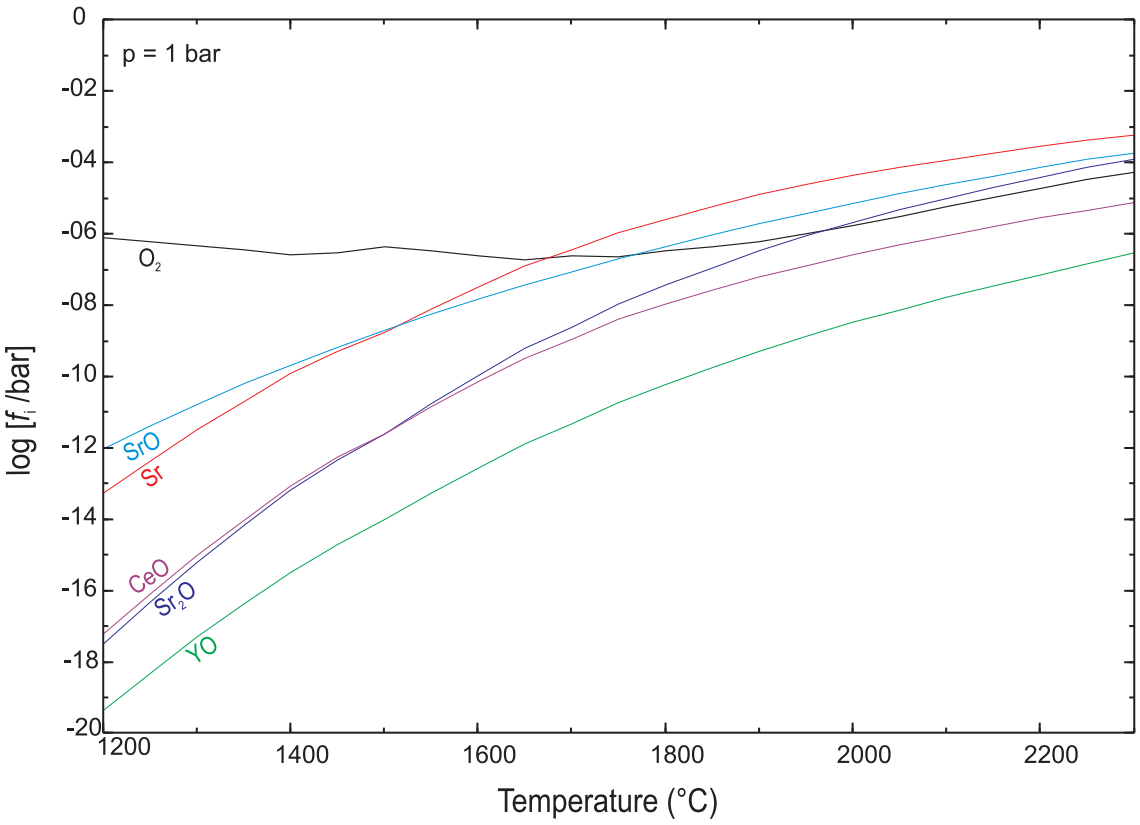

Figure 5.6: Fugacities f_i of a SY2:Ce composition dependent on the temperature referring to LHPG/mPD setup.

Atm.	Fugacities (bar) for SY2:Ce				
	Sr	SrO	Sr_2O	CeO	YO
Oxid. I	1.7×10^{-5}	1.2×10^{-4}	3.0×10^{-6}	7.3×10^{-7}	2.8×10^{-8}
Inert	2.6×10^{-4}	1.2×10^{-4}	4.5×10^{-5}	3.5×10^{-6}	1.1×10^{-7}
Red. I	4.2×10^{-4}	1.2×10^{-4}	7.3×10^{-5}	4.5×10^{-6}	1.4×10^{-7}

Atm.	Fugacities (bar) for TSS:Ce					
	Sr	SrO	Sr_2O	CeO	SiO	SiO_2
Oxid. I	3.3×10^{-5}	2.0×10^{-4}	7.4×10^{-6}	1.6×10^{-6}	6.7×10^{-7}	1.9×10^{-7}
Inert	3.9×10^{-4}	2.0×10^{-4}	8.7×10^{-5}	5.8×10^{-6}	8.0×10^{-6}	1.9×10^{-7}
Red. I	5.9×10^{-4}	1.8×10^{-4}	1.2×10^{-4}	7.3×10^{-6}	1.5×10^{-5}	2.2×10^{-7}

Table 5.2: Fugacities f of species evaporating from a SY2:Ce melt at 2250 °C and TSS:Ce melt at 2300 °C in different atmospheres.

evaporation can be expected for SY2:Ce and CS2:Ce growth. The fugacities match the monitored ion intensities during HTMS (figure 5.8).

Because of the higher melting point of tristrontium silicate (≈ 2170 °C), the calculations for a TSS:Ce melt were performed at 2300 °C (table 5.2). Due to the higher temperature, the fugacities are increased. Therefore, strong evaporation (Sr, SrO) will be expected, if TSS:Ce is grown in a LHPG setup.

Considering both the calculated fugacities of evaporating species f_i and the predominance diagram of Ce-O_2 two diametral issues become obvious. For attaining maximum concentration of trivalent cerium the reducing atmosphere III is suitable. On the other hand, oxidizing atmosphere II minimizes the evaporation for all materials. The inert or slightly reducing atmosphere I might be a compromise for achieving both aims. This aspect will be discussed in the following sections.

5.2 High-temperature mass spectrometry

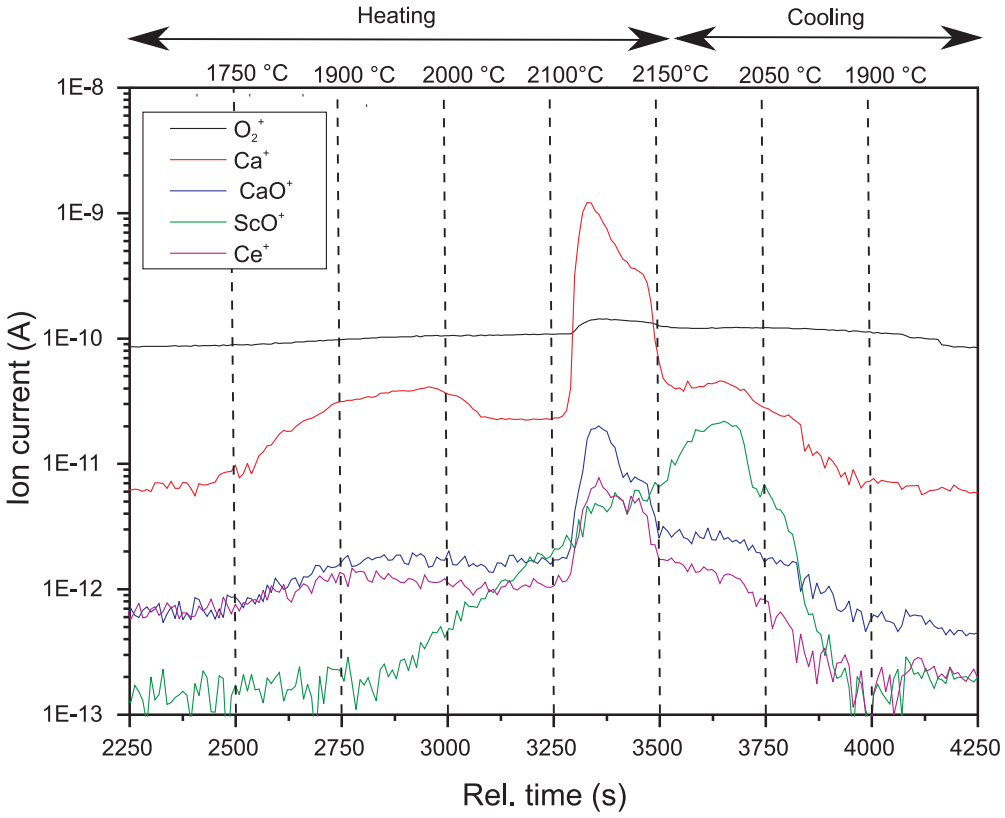

Figure 5.7: Monitored ion intensities of O_2^+ (black), Ca^+ (red), CaO^+ (blue), ScO^+ (green), and Ce^+ (purple) during heating of a $CaSc_2O_4$:Ce SCF up to 2150 °C. The dashed lines show the temperature, which was adjusted manually [101].

The calculated fugacities (5.1) indicate possible evaporating species from the melt. The combination of high-temperature mass spectrometry and elemental analysis (5.5) can confirm these calculations. While elemental analysis with ICP-OES and EDX gives evidence about the quantity of loss after growth experiments, HTMS measurements reveal the evaporating species directly during heating of crystal fibers.

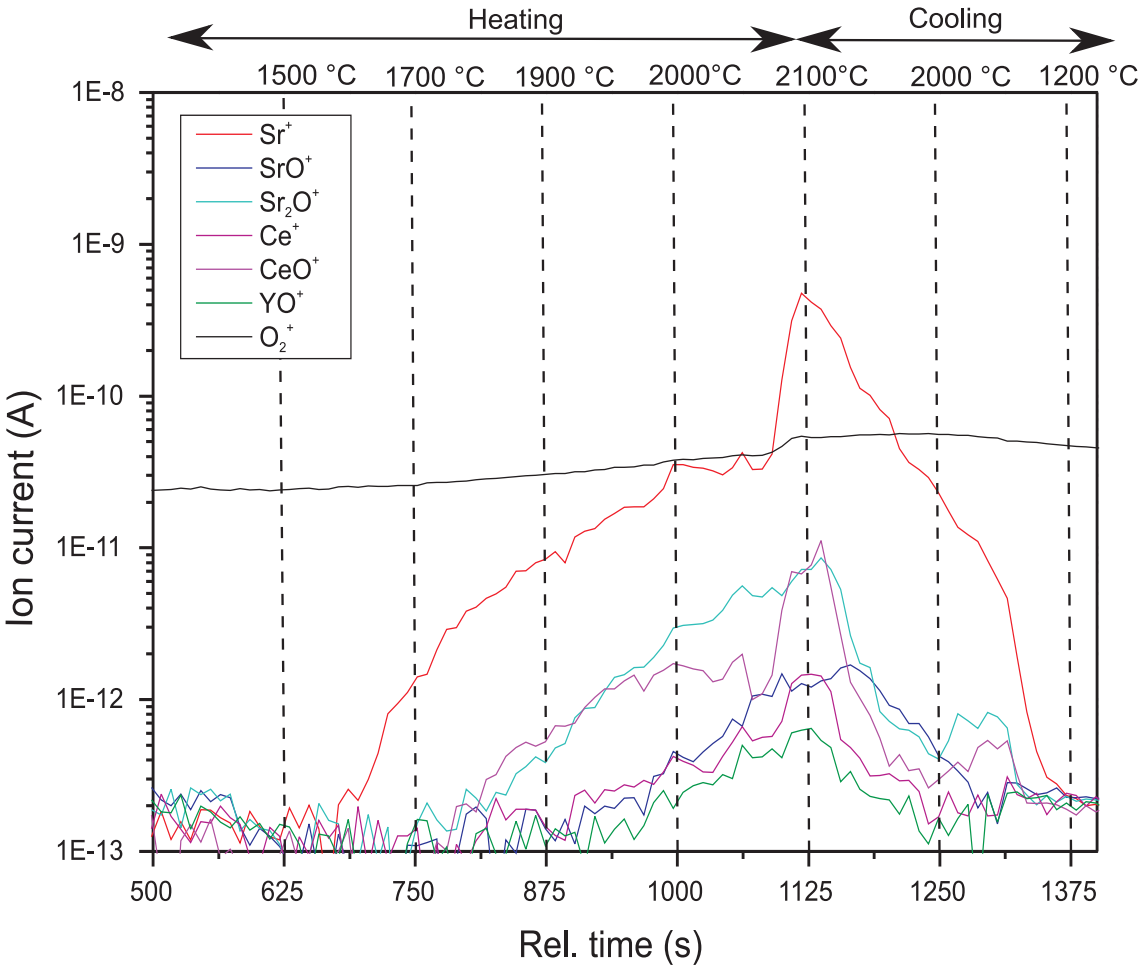

Figure 5.8: Monitored ion intensities of O_2^+ (black), Sr^+ (red), SrO^+ (blue), Sr_2O^+ (cyan), Ce^+ (purple), CeO^+ (rose), and YO^+ (green) during heating of a SrY_2O_4:Ce SCF up to 2150 °C.

Figure 5.7 shows the monitored ion intensities of evaporating calcium, calcium oxide, scandium oxide, and cerium during heating of a CS2:Ce SCF. The O_2^+ signal acts as a reference value. All evaporating species shown in the diagrams of this section show significant signal-to-noise ratios. Other calculated species were monitored, but are not shown here, because their signals were too low. Evaporation of metallic calcium started at ≈ 1800 °C. The values of CaO^+ and Ce^+ increased between 1750 °C and 2000 °C, respectively. The ScO^+ signal increased eventually after evaporation of Ca at ≈ 2030 °C. When the melting point of the material was exceeded (2110 °C), the main evaporating species Ca, CaO, and Ce showed a strong signal. These results of the kinetic measurements are in agreement with the predicted calculations under equilibrium conditions. The HTMS measurement detected signals of three species showing the highest calculated fugacities (see table 5.1). Ce instead of CeO is detected. This can be related to the high-temperature decomposition CeO→Ce+O. The simultaneous increase of the O_2^+ signal supports this assumption. The strongest signal-to-noise ratio of Ca fits to the highest value of f_{Ca}. By comparing the ion intensities (figure 5.7) with the temperature dependency of f_i (figure 5.5) the increase of the ScO^+ signal becomes obvious. When the pressure is lowered, f_{ScO} exceeds f_{CaO} and f_{Ce}. Additionally, the formation of gaseous ScO is supported

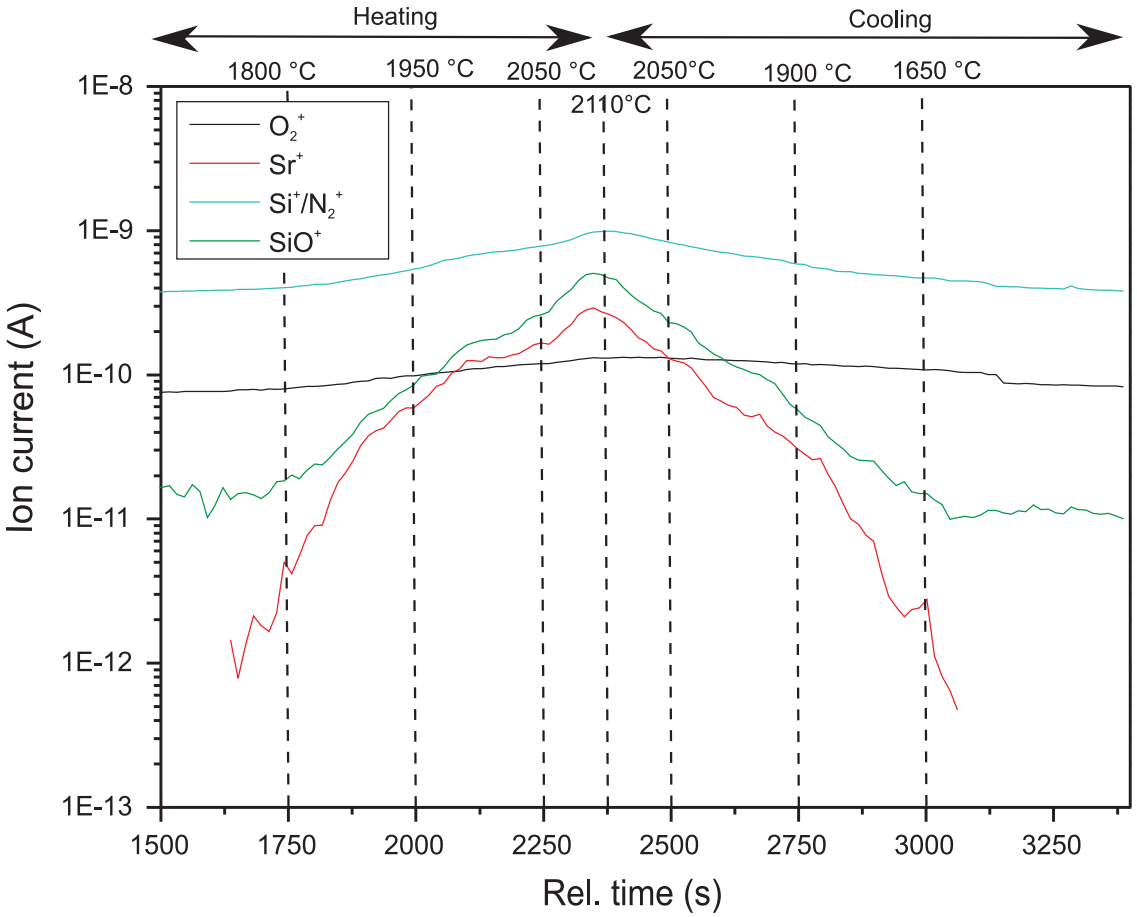

Figure 5.9: Monitored ion intensities of O_2^+ (black), Sr^+ (red), SiO^+ (green), and Si^+ (cyan) during heating of a Sr_3SiO_5:Ce SCF up to 2110 °C. Si^+ and N_2^+ interfere because of their identical m/z value (mass-to-charge ratio).

by partial melt of the fiber surface that is depleted of Ca. The melting point at the fiber surface is lowered and seems to be at ≈ 2030 °C, accompanied by a decrease of the Ca^+ signal. High amounts of Ca, CaO, and Ce are evaporating when the bulk of the fiber melts near 2110 °C. The equilibrium calculations can explain the detected species in good agreement.

Similar to the CS2:Ce results evaporation of the alkaline earth metal ion (Sr^+ signal) in a SY2:Ce SCF (figure 5.8) started at temperatures far below the melting point of the material (that is ≈ 2170 °C). Increase of Sr_2O^+ and CeO^+ signals were monitored at 1750 °C while Ce, SrO, and YO evaporation started at temperatures close to the melting point. In comparison to the CS2:Ce fiber cerium oxide instead of metallic cerium was the main evaporating species containing cerium. Significant evaporation of Sr starts at lower temperatures compared with Ca. Compared to the calculated fugacities (table 5.2) the signal-to-noise ratios fit to the values f_i. Moreover, the onsets of the ion intensities are in accordance with the temperature dependency (figure 5.6). Unlike the Ce^+ signal in the CS2:Ce intensities, a CeO^+ signal fits to f_{Ce}. In contrast to the CS2 measurement, the SY2 fiber was only partially melted after HTMS run.

The TSS:Ce fiber (figure 5.9) showed no cerium signals. At temperatures below 1800 °C, the Sr^+ signal increased, eventually followed by an increase of SiO^+.

The Si^+ signal interfered with N_2^+, because they have identical m/z (mass-to-charge ratio) values, however, a signal that started at $\approx 1800\,°C$ could be marked. The missing of a Ce^+/CeO^+ signal can be explained by the segregation and evaporation that is described in section 5.5. Because of the very low distribution coefficient and Ce evaporation, the HTMS fiber did not contain a commensurable Ce concentration. The TSS:Ce measurement did not indicate the melting point of the material (2170 °C). After HTMS run the fiber was not melted.

In general, the accordances of the calculated fugacities and the monitored ion intensities of the relevant species point out boundary conditions for the crystal growth experiments: Regarding the evaporation, a slightly oxidizing atmosphere (oxidizing II) seems to be appropriate, but for stabilizing trivalent cerium a reducing atmosphere is required. With reference to the HTMS results it seems reasonable that Ce^{3+} is stabilized by the formation of Ca vacancies as it is suggested for the $CaSc_2O_4$:Ce phosphor [113, 23]. The elemental analysis of the SCFs in section 5.5 will discuss the assumptions that arise from the calculations and HTMS measurements.

5.3 Growth parameters

Atmosphere	reducing I
ν_{seed}	1 mm/min
ν_{feed}	1 mm/min
r_{feed}	≈ 1.25 mm
r_{scf}	≈ 1.00 mm
Aspect ratio	≈ 1.5
$T_{\max}$	$\approx 2250\,°C$
Steady state length	≈ 25 mm

Table 5.3: The optimized LHPG growth conditions for CS2:Ce SCFs.

Table 5.3 summarizes the optimized growth conditions for CS2:Ce SCFs using LHPG growth. Nitrogen atmosphere (reducing I) is suitable with respect to the stabilization of Ce^{3+} and reduced evaporation. An oxidizing atmosphere could minimize the evaporation, but steady state growth was disturbed by an unsteady melt zone. This phenomenon, the oscillating thermocapillary convection (OTC) is discussed in section 5.7. Reducing atmosphere stabilizes trivalent cerium, but OTC occurred and the formation of dendrites disturbed the crystal growth process. This phenomenon is also discussed in section 5.7. By adjusting the translation rates for the seed rod ν_{seed} and the feed rod ν_{feed} to 1 mm/min a suitable reduction ratio of ≈ 0.8 was attained. By this, a feed with ≈ 1.25 mm radius is crystallized to a SCF with ≈ 1.00 mm radius. The crystal diameter for LHPG processes is limited due to the large nonlinear temperature gradients in the furnace; as presented in section 3.2.2. Thus, thermal stress is induced into the fibers during crystallization and cooling. It might be possible to increase the fiber diameter by installing an afterheater or by enlargement of the laser beam size, but such work was outside of the scope of this study. The laser power was adjusted to attain an aspect ratio of ≈ 1.5. Consequently, the maximal temperature of the melt surface was $\approx 2250\,°C$. Larger aspect ratios caused instabilities, whereas during crystallization with smaller aspect ratios the melt zone pulled apart. Under such conditions, the process was

stable, reached quasi-steady state quickly, and evaporation losses were small. The fiber length, in which steady state was attained, reached ≈ 25 mm. Fibers that had been grown much longer than the steady state length were disturbed by OTC.

Strontium yttrium oxide was crystallized using similar parameters. For cerium doped tristrontium silicate the parameters could not be optimized. But best results were attained using mPD method in nitrogen atmosphere (reducing I), 0.5 mm/min growth rate and ≈ 200 μm melt meniscus. Fibers with a maximum radius of ≈ 0.4 mm could be crystallized. The following sections will demonstrate the process of parameter optimization. The dependencies of the parameters will be explained by resulting fiber properties.

5.4 Phase analysis

XRD of tristrontium silicate

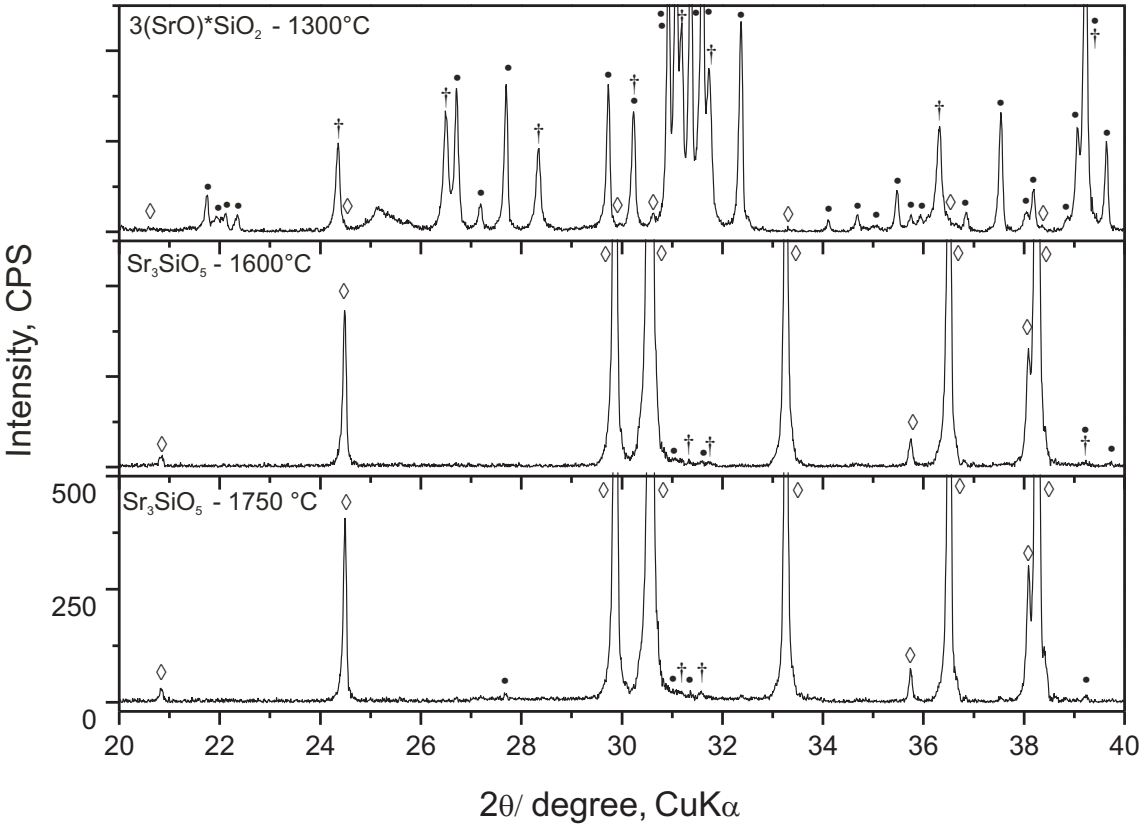

Figure 5.10: XRD patterns of the composition 3(SrO)×SiO_2 powder samples that were sintered at 1300 °C (top), 1600 °C (middle) and 1750 °C (bottom). Reflections referring to Sr_3SiO_5, Sr_2SiO_4, $Sr(OH)_2 \times H_2O$ are marked with ⋄, •, and †, respectively.

Powder compositions consisting of 3(SrO)*SiO_2 react to tristrontium silicate only at high sintering temperatures. In accordance with the DTA measurements (feed preparation, figure 3.1), the XRD patterns of a powder sintered at 1300 °C in figure 5.10 indicate a mixture of the following phases: $Sr(OH)_2 \times H_2O$ (†) and Sr_2SiO_4 (•) as main phases and Sr_3SiO_5 (⋄) as subordinated phase. The powder

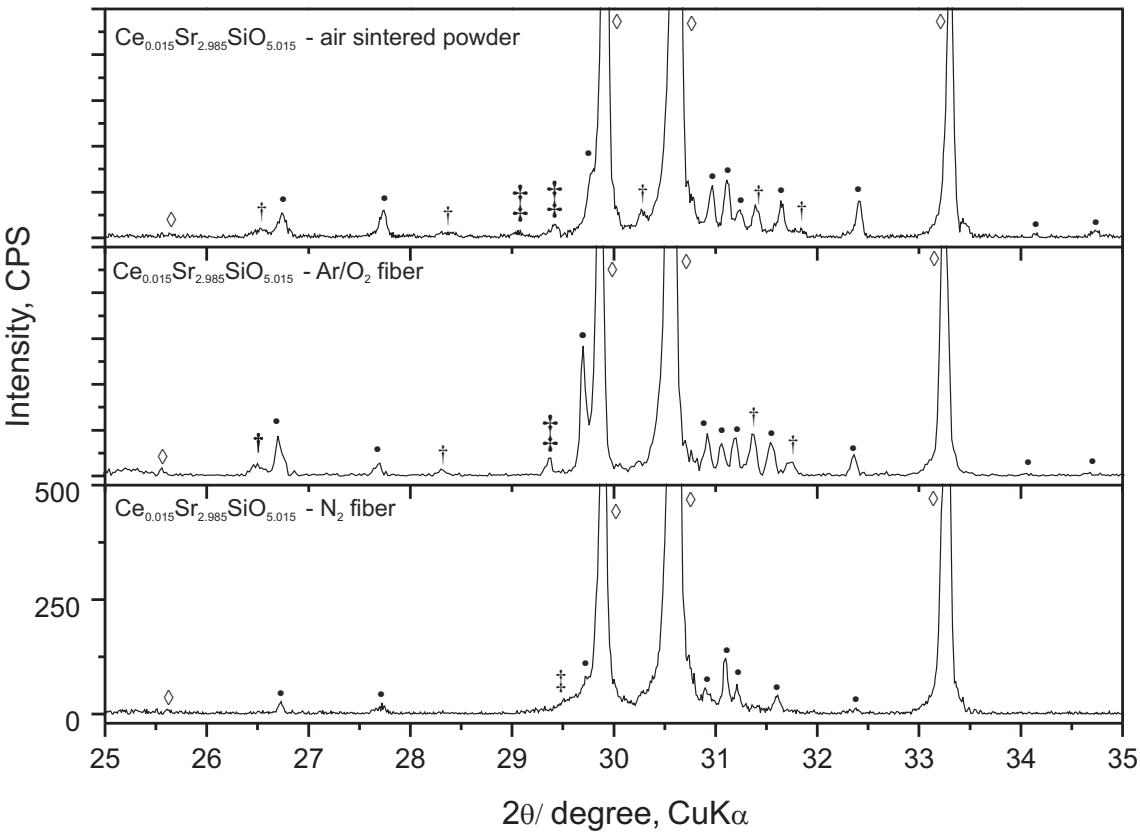

Figure 5.11: XRD patterns of air sintered Sr_3SiO_5:Ce powder (top) and two fibers, crystallized in oxidizing atmosphere (oxidizing I, middle) and reducing nitrogen atmosphere (reducing I, bottom). Sr_3SiO_5 (◇), $Sr(OH)_2 \times H_2O$ (†), $SrCeO_3$ (‡), and Sr_2SiO_4 (●).

samples were sintered for 24 h. Between 25 and 26 degree 2θ a reflection with a large FWHM value of 1638 arcsec cannot be indexed. However, this reflection does not occur in the XRD patterns of powders sintered at 1600 °C and 1750 °C. At these high temperatures, tristrontium silicate is the only main phase. Traces of $Sr(OH)_2 \times H_2O$ and Sr_2SiO_4 can be determined (figure 5.10). It is noteworthy that the reflections of the Sr_2SiO_4 phase are higher in the powder sample sintered at 1750 °C. This is because of the evaporation of Sr and SrO at high temperatures (5.2). Through the Sr deficiency, the phase Sr_2SiO_4, which has a smaller amount of Sr compared to TSS, crystallizes. The preparation of TSS feed rods required samples free of strontium oxide and its hydroxides. Otherwise, the ceramic feed rods tend to burst because of the hygroscopic behavior of SrO.

Homogeneous cerium-free feed rods could be prepared for LHPG devices. But when the samples contain cerium, the sintered powders showed inhomogeneities. As it can be seen in figure 5.11 (top), the air sintered powder consists of the phases Sr_3SiO_5 (◇) as main phase and $Sr(OH)_2 \times H_2O$ (†), $SrCeO_3$ (‡), and Sr_2SiO_4 (●) as minor phases. The following curves in figure 5.11 depict the XRD patterns of a cerium doped fiber that has been crystallized in oxidizing atmosphere (oxidizing I, middle) and slightly reducing atmosphere (reducing I, bottom). Whereas the Ce^{4+} containing phase $SrCeO_3$ is present after crystallizing in oxidizing atmosphere, this phase will be minimized, if a fiber is crystallized in nitrogen atmosphere: The strongest

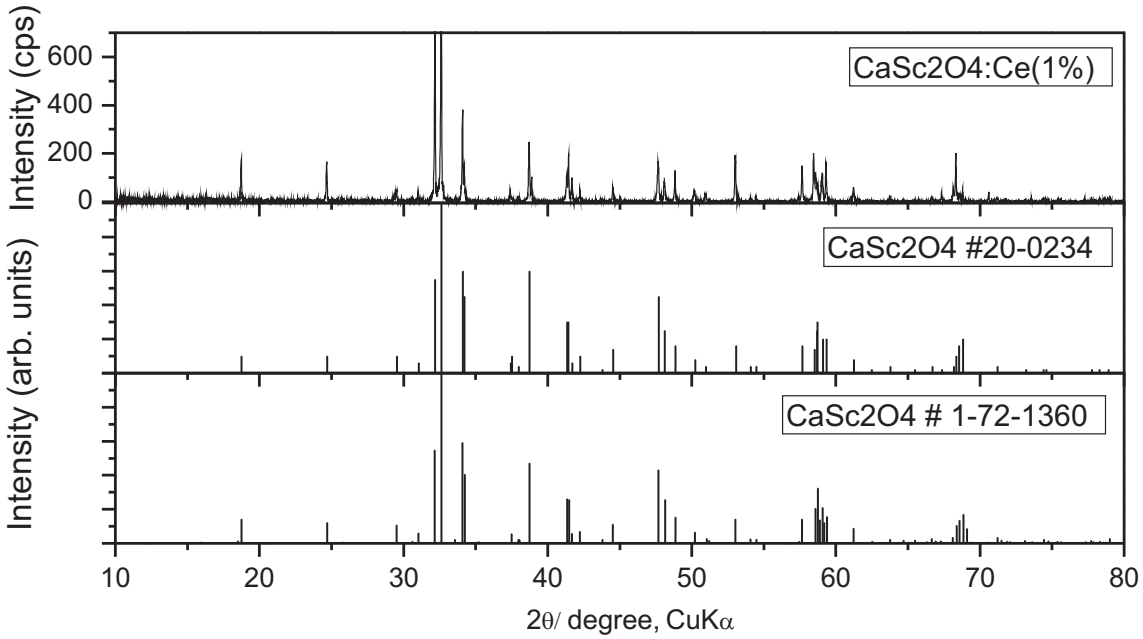

Figure 5.12: XRD patterns of a $CaSc_2O_4$:Ce SCF grown in inert atmosphere (top) compared to two PDF files [2] of $CaSc_2O_4$.

reflection of $SrCeO_3$ (‡) , (121) at 29.4 degree 2θ (PDF No. 01-081-0026 [2]), can be observed for the air-sintered powder and the oxidizing I fiber. This phase cannot be observed within the patterns of the fiber in the bottom panel. In general, fibers that were crystallized in nitrogen atmosphere, show sufficient homogeneity. It could be shown that trivalent cerium is stable at the crystallization temperature in nitrogen atmosphere, whereas the tetravalent cerium is stable in oxidizing atmosphere (figure 5.4). Tetravalent cerium is not incorporated into the TSS structure, but it formates a $SrCeO_3$ phase. The resulting deficiency of strontium is presumably balanced by the formation of Sr_2SiO_4 instead of Sr_3SiO_5. A remaining obstacle is the formation of Sr_2SiO_4 because of Sr evaporation. For the LHPG processing an excess of Sr cannot be achieved. Every excess of strontium that will formate a SrO phase after sintering will drastically reduce the stability of feed rods.

XRD of calcium scandate

Figure 5.12 compares the powder XRD patterns of a $CaSc_2O_4$:Ce SCF with literature data. Reflections referring to CaO and its hydroxides, to Sc_2O_3, and cerium oxides, or to other foreign oxide phases were not observed. All reflections except one at $2\theta = 38.8°$ can be indexed and referred to calcium scandate with the Powder Diffraction Files [2]. As this reflection occurs in all XRD patterns of $CaSc_2O_4$, it might be associated with an intermetallic ScPt phase (PDF No. 00-019-0910) as a result of the high sintering temperatures in Pt crucibles, or it could be a relict of the $K_{\alpha 2}$ 131 reflection of $CaSc_2O_4$ (PDF No. 00-020-0234).

Figure 5.13 gives a closer insight into the presence of impurities. Among these four powder XRD patterns, only the cerium doped powder [B] shows a peak at $2\theta = 28.68°$. This is the strongest reflection of CeO_2 (PDF No. 00-001-0800 [2]) that did not react completely after sintering at 1600 °C in air. Nonetheless, the cerium doped SCF that was grown in inert atmosphere does not show this reflection. The

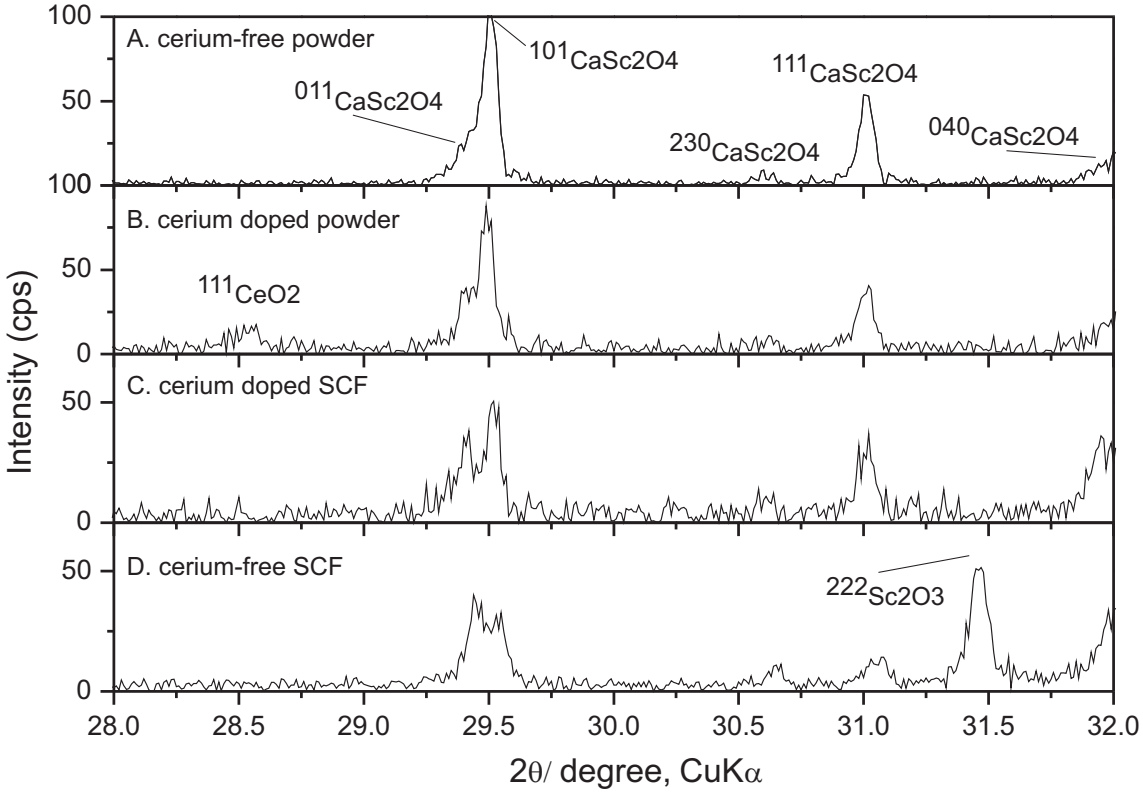

Figure 5.13: Powder XRD patterns of a cerium-free powder [A], cerium doped powder [B], cerium doped SCF [C], and cerium-free SCF [D] of $CaSc_2O_4$ and $CaSc_2O_4$:Ce(1 %). The powders were sintered at 1600 °C for 24 h in air; the SCFs were crystallized in inert atmosphere.

patterns [D] of the cerium-free SCF shows a reflection at 31.44°. This is the 222 reflection of Sc_2O_3. During LHPG growth of this fiber, time-dependent convection of the melt occurred (OTC) in accordance with evaporation of CaO (see section 5.7). Therefore, the presence of scandium oxide results from a shift of composition and could be related to the oscillation of the melt.

The XRD patterns in figure 5.13 demonstrate that LHPG is suitable for the growth of cerium doped $CaSc_2O_4$ fibers, without charge compensation by alkali metal ions, which is necessary, if phosphors are produced by the ceramic route [113]. The feasibility of doping without charge compensation is probably related to the tunnel structure of $CaSc_2O_4$, where the Ca^{2+} ions (112 pm, eightfold coordinated [110]) occupy the tunnels [92] (figure 2.9). Ce^{3+} ions (114 pm, when eightfold coordinated), have nearly the same radii. Moreover, the $CaFe_2O_4$ structure type is described as a loose packed structure with several possible coordination numbers for the alkaline earth metal ion site [93]. It seems to be plausible, that cerium doping works with the generation of Ca vacancies, as it is assumed in section 2.3.1.

5.5 Composition shift and segregation

The calculation of the growth conditions (5.1) and the measured evaporating components (5.2) indicate a composition shift during sintering and crystallization process. The resulting compositions were determined by using ICP-OES, REM-EDX, TEM-

EDX, and EMPA-WDX. The deviation of sintered feed rods, crystal fibers, frozen melt zone (LHPG), and residual melt (mPD) is demonstrated in this section. The processes that influence these deviations, a mutual interplay of segregation and evaporation, are investigated with respect to the crystal growth technique as well as the growth parameters.

5.5.1 Effective dopant distribution

Sample	Atmosphere	$k_{\mathrm{eff,ini}}$	$k_{\mathrm{eff,end}}$	Steady state
CS2_54	Oxidizing I	0.2	-	No
CS2_55	Inert	0.5	0.5	Yes
CS2_52	Reducing I	0.5	0.5	Quasi
CS2_53	Reducing II	0.4	0.4	Yes
CS2_51	Reducing III	0.4	0.4	Quasi
CS2_mpd_01	Inert	(0.7)	-	-
SY2_1	Inert	0.6	-	No
TSS_08	Inert	0.1	-	No
TSS_10	Oxidizing I	0.1	-	No

Table 5.4: Effective distribution coefficient calculated from the initial conditions $k_{\mathrm{eff,ini}}$ of LHPG/mPD experiments and the conditions at the end of a LHPG process $k_{\mathrm{eff,end}}$. Elemental analysis was measured with ICP-OES.

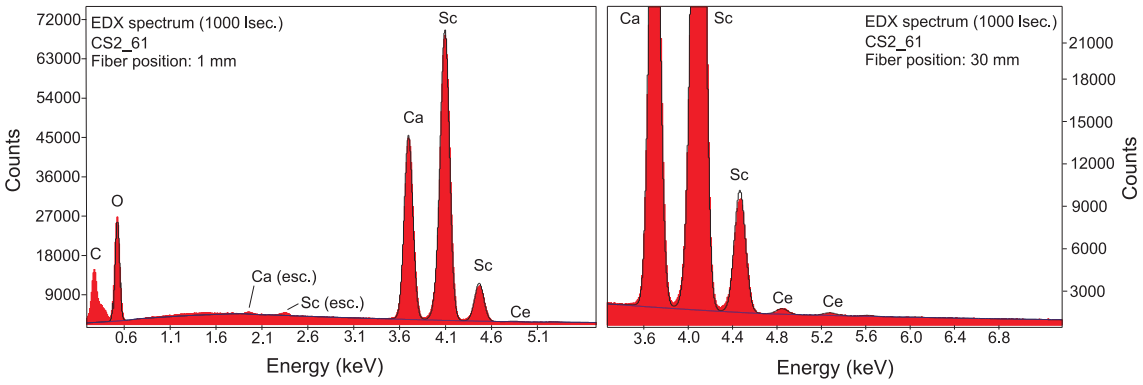

Figure 5.14: Two REM-EDX spectra of different positions in a CS2:Ce fiber. The acceleration voltage was 15 kV. The left spectrum contains the escape peaks for Ca and Sc Kα.

For LHPG setups the effective distribution coefficient k_{eff} can be estimated by:

$$k_{\mathrm{eff}}^{\mathrm{lhpg}} \approx \frac{C_{\mathrm{ini}}^{\mathrm{lhpg}}}{C_{0}^{\mathrm{lhpg}}} \approx \frac{C_{\mathrm{end}}^{\mathrm{lhpg}}}{C_{\mathrm{fz}}^{\mathrm{lhpg}}} \tag{5.1}$$

with $C_{\mathrm{ini}}^{\mathrm{lhpg}}$ and $C_{\mathrm{end}}^{\mathrm{lhpg}}$ as dopant concentration at the beginning and the end of the fiber, C_{0}^{lhpg} as dopant concentration within the feed rod, and $C_{\mathrm{fz}}^{\mathrm{lhpg}}$ as dopant concentration in the frozen melt zone [100]. This equation will be imprecise, if strong evaporation occurs. In this case, the steady state condition ($C_{\mathrm{end}}^{\mathrm{lhpg}} = C_{0}^{\mathrm{lhpg}}$) is never reached. However, a quasi-steady state is reached, if $C_{\mathrm{end}}^{\mathrm{lhpg}}$ reaches a constant

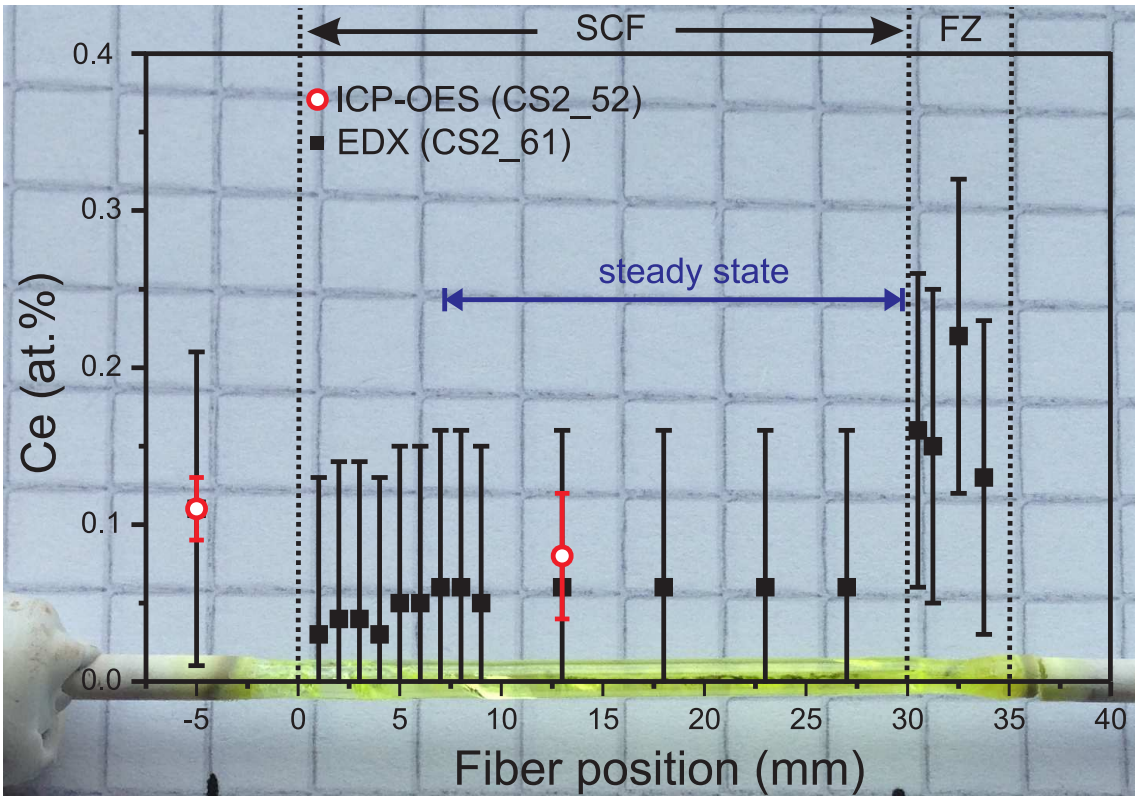

Figure 5.15: Cerium concentration measured with REM-EDX (CS2_61) and ICP-OES (CS2_52). The EDX values (black) belong to the fiber superimposed onto the x-axis.

value [101]. This is demonstrated in figure 5.15. For mPD setup equation 5.1 has to be changed to:

$$k_{\mathrm{eff}}^{\mathrm{mpd}} \approx \frac{C_{\mathrm{ini}}^{\mathrm{mpd}}}{C_{\mathrm{im}}^{\mathrm{mpd}}} \approx \frac{C_{\mathrm{end}}^{\mathrm{mpd}}}{C_{\mathrm{rm}}^{\mathrm{mpd}}} \tag{5.2}$$

with $C_{\mathrm{im}}^{\mathrm{mpd}}$, $C_{\mathrm{rm}}^{\mathrm{mpd}}$ as dopant concentration in the initial melt (im) and the residual melt (rm) at the end of the crystallization process [49]. The table 5.4 summarizes the values $k_{\mathrm{eff,ini}}$ and $k_{\mathrm{eff,end}}$, which were calculated from the initial and final conditions of LHPG/mPD experiments. The last column depicts the estimated growth conditions. Either ideal steady state conditions $C_{\mathrm{end}}^{\mathrm{lhpg}} = C_{0}^{\mathrm{lhpg}}$ (yes), quasi-steady state conditions $C_{\mathrm{end}}^{\mathrm{lhpg}} = \text{const.}$ (quasi) or no steady state conditions $C_{\mathrm{end}}^{\mathrm{lhpg}} \neq \text{const.}$ (no) were determined. All fibers that were used for table 5.4 were grown with the same crystallization rate of 1 mm/min and aspect ration. For cerium doped calcium scandate k_{eff} is between 0.4 and 0.5 for inert and reducing atmosphere, while it decreases in value for the oxidizing atmosphere. The high fugacity $f_{\mathrm{O_2}}$ stabilizes tetravalent cerium that seems to be less favorable incorporated into the calcium scandate structure. The mPD fiber (CS2_mpd_01) showed a higher k_{eff}. This can be related to a different kind of evaporation of cerium and will be discussed in section 5.5.2. For cerium doped strontium yttrium oxide $k_{\mathrm{eff}} = 0.6$ is higher than for CS2:Ce.

A LHPG CS2:Ce fiber (CS2_61) that had been crystallized with optimized growth conditions was sectioned, polished and embedded. Two EDX spectra of different fiber positions are shown in figure 5.14. At 1 mm, approximately 60 seconds after

the seeding process, the fiber contains only a small amount of cerium. At 30 mm fiber position, close to the frozen melt zone of the crystallization process, the cerium concentration is enhanced. The cerium Lα1 (4.840 eV) and Lβ2 (5.262 eV) emission lines can be used to quantify the composition. The standardless ZAF (atomic number, absorption, and fluorescence correction) quantification provides larger errors when compared to ICP-OES quantification. However, the calculated values can be used to demonstrate the cerium incorporation into a crystal fiber. This is shown in figure 5.15:

An axial cerium concentration profile (figure 5.15) has been determined using REM-EDX. Superimposed onto the x-axis of the concentration profile, the SCF including feed rod (left) and frozen melt zone (right) combines the fiber position with the concentration profile. All EDX values inhere large error bars. Therefore, more accurate ICP-OES values of a fiber crystallized with the same growth parameters are given for comparison. Within the feed rod (fiber position -5 mm), the atomic concentration of cerium is 0.12 at.%. At the early stage of the crystallization process (0-2 mm), cerium cannot be detected within the fiber. Between 5 and 30 mm, the cerium concentration is constant. The concentration measured with EDX (0.05 at.%) match the ICP-OES values (0.06 at.%). Within the frozen melt zone, the cerium concentration is enhanced ($\approx$ 0.22 at.%). This concentration profile fits to the calculated effective distribution coefficient $k_{\mathrm{eff}}^{\mathrm{lhpg}}$ that has been calculated based on ICP-OES values. Moreover, this profile is used for the steady state discussion in 5.5.4.

Tristrontium silicate does not incorporate high amounts of cerium. The small k_{eff} values fit to the phase analysis of crystal fibers (5.4). Only small amounts of cerium are incorporated into the fiber. When the melt zone exceeds a critical Ce concentration, a second phase $SrCeO_3$ crystallizes that has been detected using XRD (5.11). This phase can be minimized using reducing atmosphere I. Likewise the calcium scandate, the trivalent cerium is easily incorporated into the tristrontium silicate structure. The low k_{eff} value for TSS:Ce also explains the HTMS measurements (5.9). Because of the low cerium concentration no Ce^+ ion intensities could be measured. The following section discusses the composition shift of the crystal fibers with respect to the atmosphere and the growth method.

5.5.2 Composition shift

Elemental analysis (ICP-OES) of LHPG fibers gave further information on the composition shift. Table 5.5 shows the relative deviations from the weighed portion of the elements within a ceramic feed rod, single crystal fibers of CS2, CS2:Ce, CS2:Ce,Mg, and their frozen melt zones crystallized in different atmospheres (table 3.2). All relative values describe the deviations from the mole fractions of the elements. These deviations, supported by the calculated fugacities (table 5.1) and experimental HTMS results (figure 5.7), explain the shift of composition within the crystal fibers:

The feed rod that was sintered at 1600 °C shows a Ca and Ce deficiency, whereas Sc is enriched. This implies, calcium and cerium are already evaporating at sintering temperatures analogously to the HTMS signals (figure 5.7). Lower sintering temperatures (1200 °C) can minimize this loss as it is shown in table 5.7 for the strontium yttrium oxide. The cerium-free fiber (CS2_02) shows the smallest deviations. Note

Sample	Rel. deviation (%)			Sample number
	Ca	Sc	Ce	
SCF (inert)	-1.8	+0.9	-	CS2-02 mid
Feed rod	-0.9	+0.5	-5.4	CS2-P3
SCF:Ce (oxidizing I)	-2.8	+1.8	-80.6	CS2-54 begin
SCF:Ce (oxidizing I)	-2.0	+1.3	-57.6	CS2-54 end
SCF:Ce (inert)	-3.9	+2.1	-43.0	CS2-55 begin
SCF:Ce (inert)	-4.3	+2.5	-66.5	CS2-55 end
FZ (inert)	-6.4	+3.4	-36.3	CS2-55 frozen melt zone
SCF:Ce (reducing I)	-4.4	+2.5	-56.1	CS2-52 begin
SCF:Ce (reducing I)	-4.3	+2.3	-40.9	CS2-52 end
FZ (reducing I)	-4.4	+2.1	-11.6	CS2-52 frozen melt zone
SCF:Ce (reducing II)	-6.2	+3.4	-68.9	CS2-53 begin
SCF:Ce (reducing II)	-11.2	+5.5	-14.5	CS2-53 mid
SCF:Ce (reducing II)	-5.6	+2.9	-13.3	CS2-53 end
FZ (reducing II)	-14.1	+6.2	+146.7	CS2-53 frozen melt zone
SCF:Ce (reducing III)	-22.4	+11.4	-63.1	CS2-51 begin
SCF:Ce (reducing III)	-20.8	+10.5	-37.9	CS2-51 end
FZ (reducing III)	-20.2	+9.6	+66.1	CS2-51 frozen melt zone
SCF:Ce,Mg (inert)	-5.9	+3.1	+1.1	CS2-42 mid

Table 5.5: Relative deviations (from the weighed portion) of the elements within a ceramic feed rod, single crystal fibers of CS2, CS2:Ce, CS2:Ce,Mg, and their frozen melt zones crystallized in different atmospheres (composition: 3.2). Elemental analysis was measured with ICP-OES.

that the relative deviations of Ca and Sc compensate each other: $\Delta Ca \approx (-2) \times \Delta Sc$. This implies, that the deviations are not caused by an impurity but by evaporation of Ca.

The elemental analysis, supported by the HTMS measurements (section 5.2) and calculated growth conditions (section 5.1) lead to a further understanding of the mass flow during LHPG growth. The fiber CS2_54, crystallized in oxidizing atmosphere, shows a much higher deficiency of cerium than should be expected from the thermodynamic calculations. The incompatibility of tetravalent cerium, which is stabilized in oxidizing atmosphere, causes a high cerium deficiency inside the crystal fiber. The cerium content in the melt zone exceeds, but do not reach a high concentration because of the stronger evaporation inside the cerium-enriched melt zone. According to the calculated fugacities, the fibers show a greater loss of calcium, when crystallized in atmospheres containing more hydrogen: -4.4 % calcium deviation in reducing atmosphere I (CS2_52, no hydrogen), -6.2 % in reducing atmosphere II (CS2_53, 1 % hydrogen), and -22.4 % in reducing atmosphere III (CS2_51, 5 % hydrogen). However, a quasi-steady state is attained in fiber CS2_52 when Ca deviation stays constant alongside the crystallization process. Furthermore, fiber CS2_53 is close to steady state, because Ca as well as Ce deviations are constant. Taking account of the mass lost due to the evaporation, steady state conditions are reached and a constant mass flow from the feed to the melt zone and from the melt zone into the fiber is attained. Fiber CS2_42 has been prepared from a Ce^{3+} and Mg^{2+} doped feed rod. Under the assumption that valence-coupled diadochy takes place, $Ce^{3+} + Mg^{2+} \leftrightarrow Ca^{2+} + Sc^{3+}$, the fiber shows a higher concentration of

cerium. On the other hand, no Mg has been detected inside the SCF. The above mentioned assumption including Mg^{2+} co-doping does not work for LHPG growth. Note that co-doped elements (e.g. Mg^{2+}) can change k_{eff} of a species (e.g. Ce^{3+}), even if they are not incorporated into the crystal [121].

Composition shift of mPD fibers

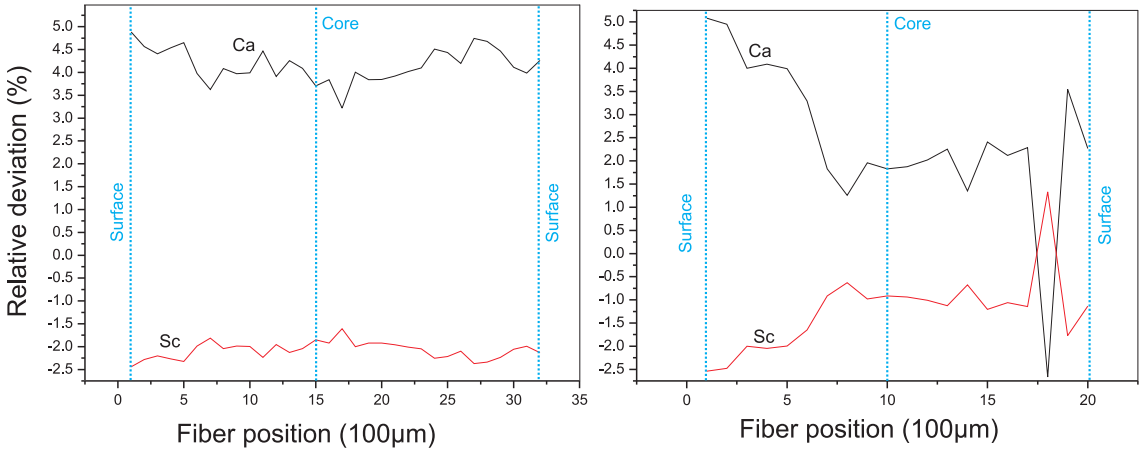

Figure 5.16: Radial composition shift of Ca and Sc inside a CS2 SCF at the beginning (left) and end (right) of the mPD crystallization. The composition was measured with EMPA-WDX. The reverse Ca and Sc deficiency at fiber position 17.5 is an outlier.

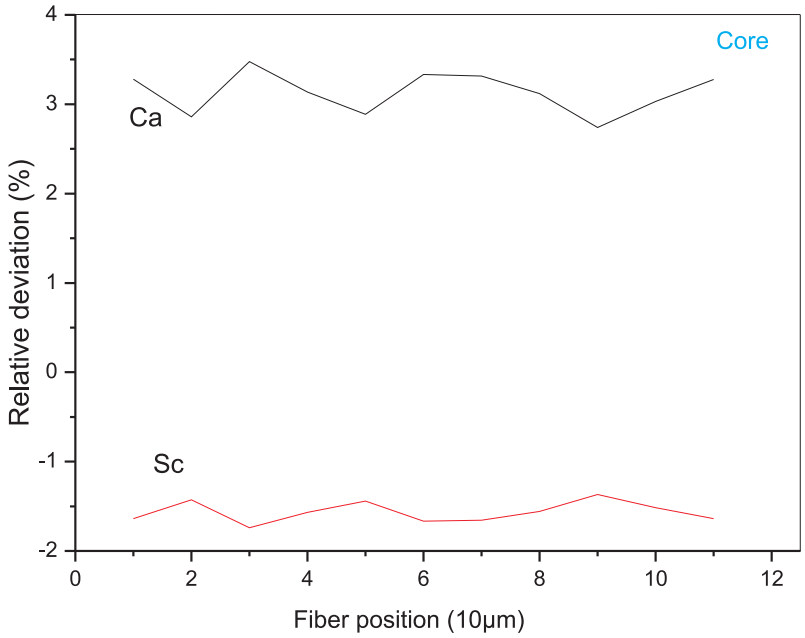

Figure 5.17: Radial composition shift of Ca and Sc at the core of a mPD fiber. The composition was measured with EMPA-WDX.

Fibers, crystallized in mPD setup, showed different deviations. The calcium content is higher than in the feed composition, cerium is reduced according to $k_{\text{eff}}^{\text{mpd}}$. From the beginning to the end of the crystallization process, both, the cerium and

Sample	Rel. deviation (%)			Sample number
	Ca	Sc	Ce	
SCF	+2.0	-0.9	-	CS2-S4 end
SCF	+3.7	-1.9	-	CS2-S4 begin
SCF:Ce	+4.4	-2.0	-21.4	CS2-mpd-01 begin
SCF:Ce	-0.1	-0.2	-33.2	CS2-mpd-01 end

Table 5.6: Relative deviation (from the weighed portion) of the elements within SCFs that were grown using mPD. All fibers were grown in inert atmosphere. The fiber CS2-S4 is undoped and used for EMPA measurements.

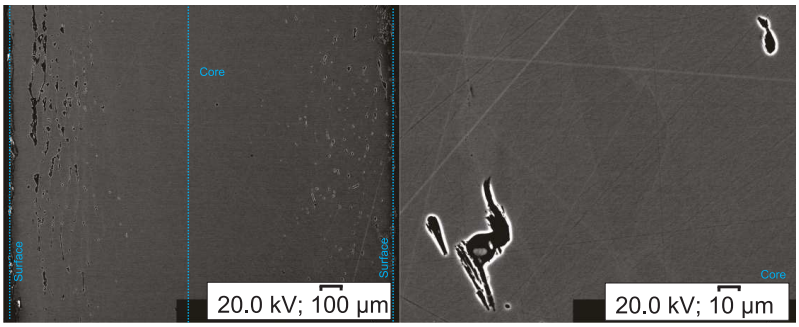

Figure 5.18: Two EMPA back-scatter electron images of a mPD CS2 fiber. Left side: Overall view of the axial-sectioned SCF (figure 5.17). Right side: View of the core (figure 5.16).

the calcium content, decrease (CS2_mpd_01). The decrease of the cerium content (-21.4 % to -33.2 %) does not fit to the $k_{\text{eff}}^{\text{mpd}}$ value given in table 5.4.

WDX-EMPA measurements can explain these deviations: Figure 5.16 depicts the radial composition of a cerium-free mPD-SCF. The EMPA measurements were performed by Dr. Rhede (Deutsches GeoForschungszentrum Potsdam, Germany). Calcium and scandium deviations are given at the beginning (left) and end (right) of the mPD crystallization. Alongside the radial direction of the CS2_S4 fiber, the calcium content is increased (figure 5.16). From the core to the surface of the fiber, the Ca content increases as well, the Ca deviation curves are U-shaped. The reverse Ca and Sc deficiency at fiber position 17.5 is an outlier. Apparently, Ca that evaporated from the melt re-condensed at the solid-liquid interface. The U-shaped deviation curve and the fact that the Ca deviation is lowered at the end of the crystallization process match the assumption of re-condensation. Moreover, re-condensed cerium from the gas phase can explain the high $k_{\text{eff}}^{\text{mpd}}$ value that is calculated from the ICP-OES results. If cerium evaporates and re-condenses in the same way as calcium, it becomes vivid that the crystal fiber CS2_mpd_01 is Ce depleted at the end of the crystallization process (table 5.6). This behavior can also explain the rough surface of mPD fibers. Note that also within the core of the fiber deficiencies are not constant (figure 5.17). The positive Ca deviation varies between +3 % and +3.5 %. Deviations of Ca and Sc are complementary to each other. The EMPA back-scatter electron images of a mPD CS2 fiber, figure 5.18, show inhomogeneities at the fiber surface. Moreover, different shades can be observed in the right picture of this figures. These arise from Ir impurities (up to 1 %) that could be detected using EMPA-WDX. The left image reveales macroskopic holes at the

fiber surface. These defects are not observed in LHPG fibers and might be caused by the Ca surplus.

Concerning the mass flows, LHPG and mPD differ from each other. Evaporated species during LHPG growth mainly condense at the inner surface of the recipient and do not interact with the crystal growth process. Species evaporating from the thin melt meniscus of an mPD setup re-condense at the fiber crystallization front. As of this writing, LHPG crystallization seems to be superior to mPD crystallization because of the different mass flows.

Composition shift of SY2

Sample	Rel. deviation (%)			Sample number
	Sr	Y	Ce	
Feed rod	-0.3	+0.2	+1.21	SY2-P1
SCF	-3.1	+2.0	-42.4	SY2-1 begin
SCF	-8.6	+4.7	-34.8	SY2-1 end
FZ	-25.3	+12.9	-20.0	SY2-1 frozen melt zone

Table 5.7: Relative deviation (from the weighed portion) of the elements within a SCF of SY2:Ce that were crystallized in inert atmosphere using LHPG.

The deviations of a SY2:Ce SFC (table 5.7), crystallized in inert atmosphere, are similar to the CS2:Ce results (table 5.5): Because $k_{\text{eff}}^{\text{lhpg}}(\text{CS2}) \approx k_{\text{eff}}^{\text{lhpg}}(\text{SY2})$, the fiber showed a significantly lower cerium content. Because of the small length of the fiber no steady state was attained. The melt zone is Sr and Ce depleted. In comparison with the CS2:Ce SCF, the strontium shift is greater than the calcium shift: $-8.6\,\%$ to $-4.3\,\%$ at the end of the crystallization process (SY2_1, CS2_55). This is in accordance with the HTMS measurements and the caclutated fugacities (sections 5.1 and 5.2). Evaporated species could be collected and determined as mainly SrO.

Composition shift of TSS

Sample (atm.)	Rel. deviation (%)			Sample number
	Sr	Si	Ce	
PCF (inert)	-1.5	+5.1	-45.3	TSS-p4-mpd-04
PCF (inert)	-3.3	+10.0	-83.6	TSS-p4-kr10
PCF (oxidizing I)	-2.1	+7.6	-92.5	TSS-p4-kr08

Table 5.8: Relative deviation (from the weighed portion) of the elements within polycrystalline fibers of TSS that were crystallized using mPD (TSS-p4-mpd-04) and LHPG (TSS-p4-kr08, TSS-p4-kr10).

Table 5.8 outlines the deviations within polycrystalline fibers of TSS:Ce. The sample TSS-p4-mpd-04 was crystallized in inert atmosphere. The fiber showed a small loss of strontium (-1.5 %) and a silicon surplus (+5.1 %), the cerium loss is 45.3 %. The massive cerium deviations (-82.6 %, -92.5 %) of the LHPG fibers point out a severe drawback. Because of high evaporation (section 5.1) and a small k_{eff} value only small amounts of cerium are incorporated into the fiber. Moreover, the

phase analysis via XRD (section 5.4) and the elemental analysis with EDX reported inhomogeneities of the Ce content. The LHPG method is not suitable for the growth of tristrontium silicate. Surprizingly, the deviations of CS2 and TSS fibers that were both crystallized with mPD, showed different deviations. Whereas the EMPA results revealed the re-condensation of evaporated Ca (and Ce), the cerium fibers in TSS are Sr depleted. Under the assumption of similar mass flows, Sr should be enriched inside the fibers. However, stronger evaporation of Sr prior to the crystallization process could explain this diametrically behavior.

5.5.3 Oxygen content of SCFs

Sample	Atm.	$w_{\mathrm{O}}^{\mathrm{icp-oes}}$	$w_{\mathrm{O}}^{\mathrm{cghe}}$	Rel. deviation (%)
CS2_22	inert	0.329	0.325	-1
CS2_52	reducing I	0.330	0.322	-3
SY2_2	inert	0.196	0.195	-1

Table 5.9: Comparison of the oxygen mass fraction w_O , calculated from the ICP-OES composition, with the oxygen mass fraction that was determined by carrier gas hot extraction (CGHE).

The elemental analysis (ICP-OES) was used to build a fiber composition from the mole fractions of the metal cations. The oxygen mass fraction within these compositions can be compared with the mass fraction that had been measured using carrier gas hot extraction (CGHE). CGHE is a method for oxygen (and nitrogen, sulfur, and hydrogen) quantification [54]. A sample is heated within an IR furnace. Samples with $\approx 100\,\mathrm{mg}$ weight can be analyzed in three fundamental steps [53]: 1. The amount of oxygen is quantitatively reduced by carbon, often assisted by metallic melt forming additives. 2. The gaseous reaction products are released with respect to t and T conditions. 3. Quantitative detection of the gaseous products is performed. Dr. Saurenz (Gfe Fremat GmbH, Freiberg, Germany) analyzed samples (table 5.9) using CGHE. The small deviations of the CS2:Ce fibers CS2_22, CS2_52, and the SY2:Ce fiber SY2_2 are in accordance with a good crystal quality. The oxygen mass fraction calculated from the ICP-OES results can only give an theoretical value. The CGHE values are directly measured. Therefore, the negative deviations of the CGHE values from the theoretical values could be related to oxygen vacancies. On the other hand, the crystallized fibers did not show black color related to a high amount of O vacancies. The errors for the CGHE measurement cannot be displayed, because the sample mass was below the mass ($\approx 100\,\mathrm{mg}$) for standard quantification.

5.5.4 Summary

With respect to the thermodynamic calculations, the HTMS measurements and the elemental analysis, the following results can be summarized: The LHPG method is suitable for the single crystal fiber growth of CS2:Ce and SY2:Ce, whereas no TSS:Ce SCFs could be fabricated by this method. However, with the micro-pulling-down method, TSS:Ce SCFs could be grown. The inert and reducing atmosphere I are suitable the for the stabilization of trivalent cerium with low evaporation. The

following section will present and discuss the crystalline quality of the SCFs from macroscopic to atomic scale.

5.6 Crystal quality

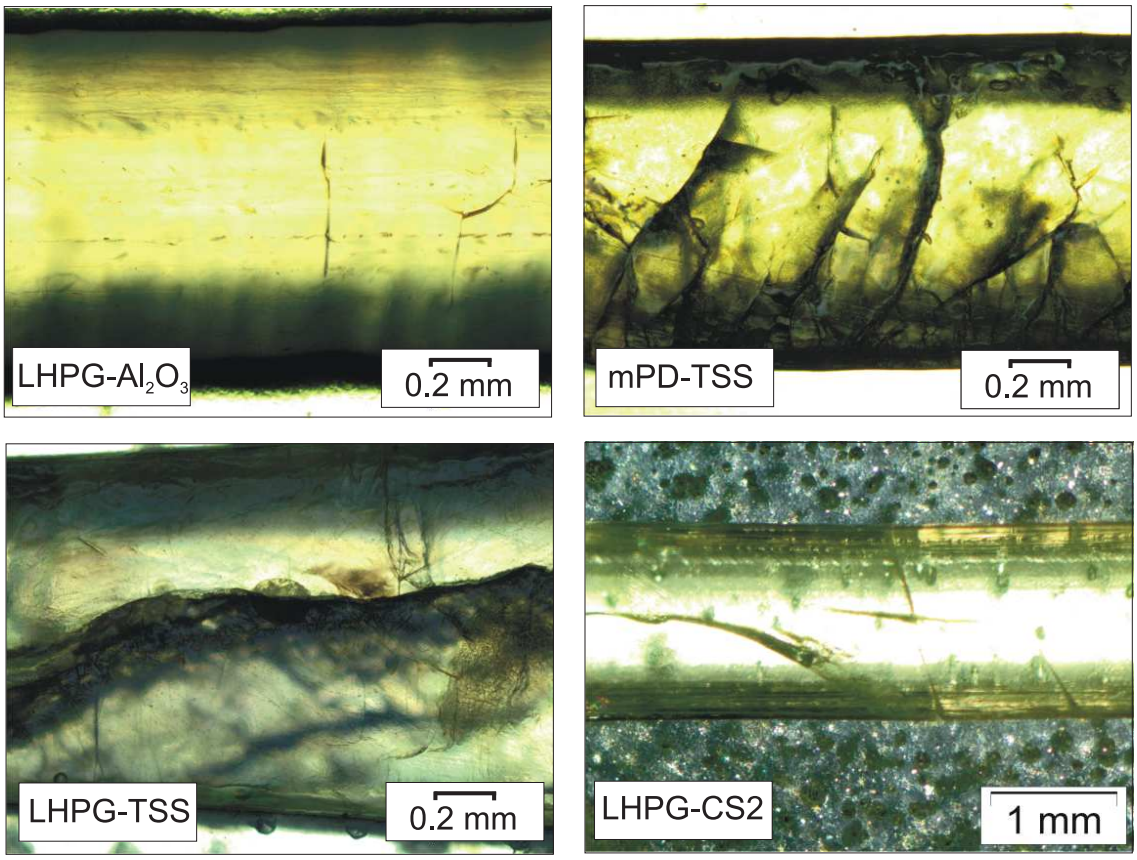

Figure 5.19: Optical microscope images of SCFs in a clockwise direction: LHPG Al_2O_3 as reference fiber, TSS:Ce mPD fiber (tss_p5_mpd_03), cerium-free TSS fiber (tss_p4_03), CS2:Ce LHPG fiber (cs2_61).

The main defects that degenerate the performance of melt-grown and float zone (laser) crystals are any which can absorb, reflect, refract or scatter light or electrical energy. Therefore, cracks, growth striations, facets, twins, inclusions, cellular structures, dislocations, color centers, and voids should be eliminated [27]. For determining macro-defects axial sections of SFC were examined using an optical and an electron microscope (SEM).

Axial sections of single crystal fibers are depicted in figure 5.19. Al_2O_3 was grown using LHPG technique as a reference fiber. In comparison to the reference, the LHPG fiber of tristrontium silicate (bottom left) reveals visible cracks and diameter variations. The fiber is semi-transparent. The mPD fiber of cerium doped TSS (top right) is transparent and could be grown with constant diameter. The fiber has visible cracks being radially oriented. The best quality regarding visible defects reveals the CS2 fiber (bottom right) that was grown with optimized LHPG parameters. The fiber has a constant radius, is nearly free of visible cracks, and is transparent.

5.6.1 Rocking curve

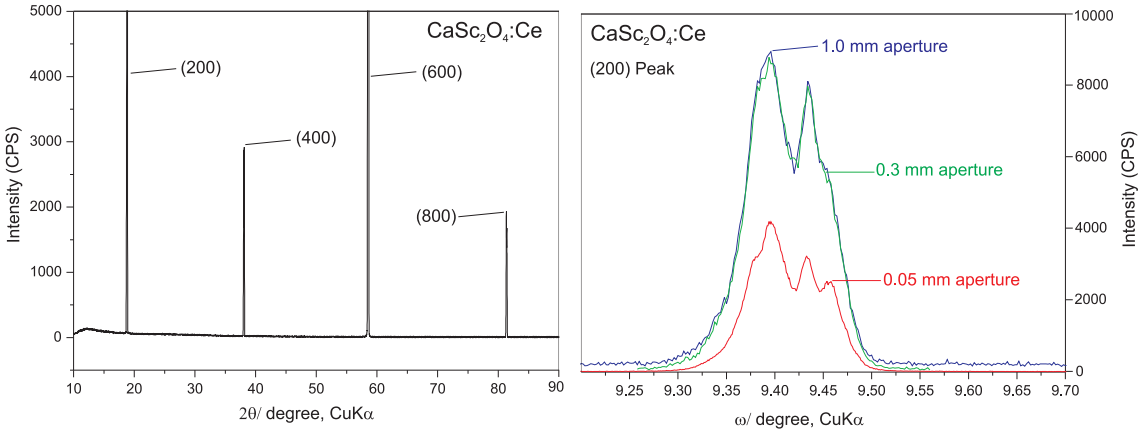

Figure 5.20: Theta-two theta (left) and a omega scan (rocking curve, right) of a (100) CS2:Ce sample. The rocking curves were measured with different apertures 1.0 mm (blue), 0.3 mm (green), and 0.05 mm (red).

Rocking curves are used to reveal details on the integral real structure of crystals [74]. Instead of rotating the detector, the Bragg angle is adjusted and the sample is rotated around the so called omega axis. Thus, it is possible to gain information about the crystal quality [115].

Figure 5.20 reveals a theta-two theta scan (left) and a rocking curve (right) of a (100) CS2:Ce sample. The 2θ scan shows the diffraction patterns of the sample with its (200), (400), (600), and (800) reflections that can be indexed with PDF No. 01-074-0449 [2]. The reflections are sharp and include small FWHM values (0.142 to 0.150°). Their intensities fit to the measured and calculated intensities in the PDF file. The diagram on the right side depicts the rocking curves for the (200) reflection. The measurement was performed using different apertures (1.0 mm (blue), 0.3 mm (green), and 0.05 mm (red)). The curve with a 0.05 mm aperture reveals the Bragg reflection for (at least) four different grains. These arise from low angle grain boundaries (LAGB). Neither evidence for crystal twinning nor polycrystallinity or high angle grain boundaries could be detected. The FWHM above all LAGBs is $\approx$ 343 arcsec. The LAGBs could be arising from induced thermal stress during LHPG growth because of the high temperature gradient.

5.6.2 Transmission electron microscopy

Whereas the omega scan (rocking curve) gave some indication about the integral crystal quality, transmission electron microscopy was used for atomic scale analysis. We wanted to determine possible crystal defects. Moreover, TEM could be used for a better understanding of the cerium doping mechanism. TEM measurements were performed by Toni Markurt (Leibniz Institute for Crystal Growth, Berlin, Germany). Note that the crystallographic array for TEM measurements of CS2 was *Pnam*, the corresponding CS2 structure in section 2.3.1 is *Pnma*. A (010) sample of a LHPG CS2:Ce crystal, grown with optimized growth conditions, was fabricated. Figure 5.21 depicts the oriented fiber (left) and the chemical mechanical polished (CMP) specimen (right). The fiber growth direction is [22$\bar{1}$]. The Nomarski image of

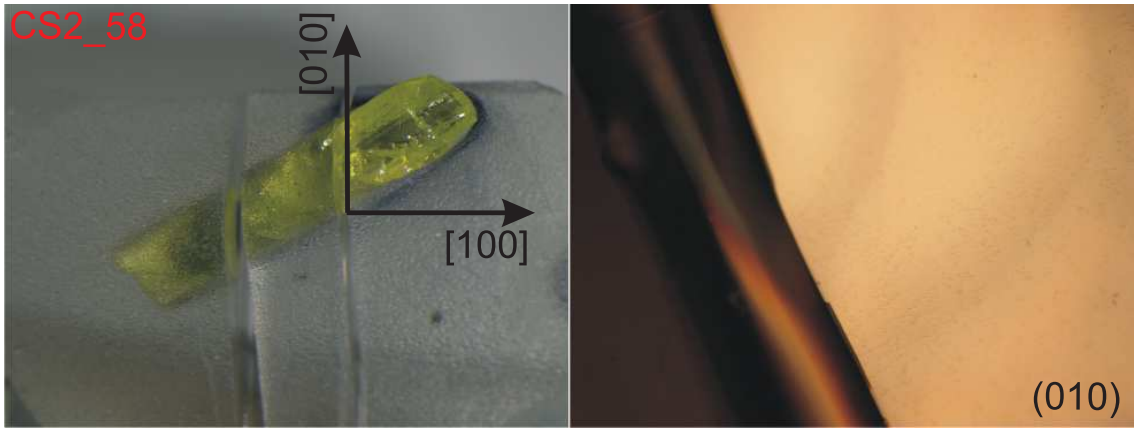

Figure 5.21: An oriented CS2:Ce SFC (left) was used for fabricating a (010) TEM sample. The Nomaski image of the CMP polished sample (right) reveals etch pits. Note that the crystallographic array for TEM measurements of CS2 was *Pnam*, the corresponding CS2 structure in section 2.3.1 is *Pnma*.

the CMP polished sample reveals etch pits. The STEM-HAADF image in figure 5.22 reveals good crystal quality in atomic scale. The draw at the top is the constructed supercell in [010] direction that was used for simulation of STEM-HAADF (bottom left). The simulation was performed using the multislice frozen phonon high angle annular dark-field image simulation [15]. The accumulated STEM-HAADF image of the sample (bottom left) matches the simulated image well. The atom columns of Sc and Ca are regularly arranged and correspond to the supercell structure. It was not possible to detect irregularities in the columns, which can be attributed to Ce incorporation. The regular structure, in combination with other measurements (XRD, spectroscopy, rocking curve), however, indicates homogeneous incorporation of Ce into the CS2 structure. No cerium inclusions, as detected for TSS:Ce, could be found. Also, the simulated and measured diffraction patterns of the sample, figure 5.23, are in good accordance to each other. The diffraction pattern was determined in $\approx$ [010] direction, with a 0.03° tilt. The diffraction image was monitored with a convergent beam (semi-convergence angle 1.3 mrad). Both images, the simulated and monitored diffraction patterns, are nearly identical. They reveal identical airy disks and Kikuchi lines. This implies, that the crystal structure of CS2:Ce is not disturbed by the incorporation of cerium.

We assume that trivalent cerium is incorporated on the Ca position. To confirm this assumption TEM-EDX analysis was performed. Figure 5.24 shows two TEM-EDX spectra that were monitored under different angles. The term k_x/g_{200} represents the relation of the in-plane component of the electron beam wave vector, k_x, to the reciprocal scattering vector of the (200) reflection, g_{200}. In comparison to SEM, the TEM electron beam has more energy (200 keV to 15 keV). Therefore, more accurate elemental analysis is possible via TEM-EDX. Analysis of the background corrected TEM-EDX spectra (figure 5.24) give cerium concentrations of 0.13 ± 0.02 at.%, independent on k_x/g_{200}. The concentration was calculated using Cliff-Lorimer Ratio technique [122]. This implies that the fiber that was used for TEM was grown with steady state conditions ($C_{\text{end}}^{\text{lhpg}} = C_0^{\text{lhpg}}$).

The TEM-EDX measurements were used for atomic site location by channeling enhanced microanalysis (ALCHEMI). ALCHEMI is a quantitative technique for

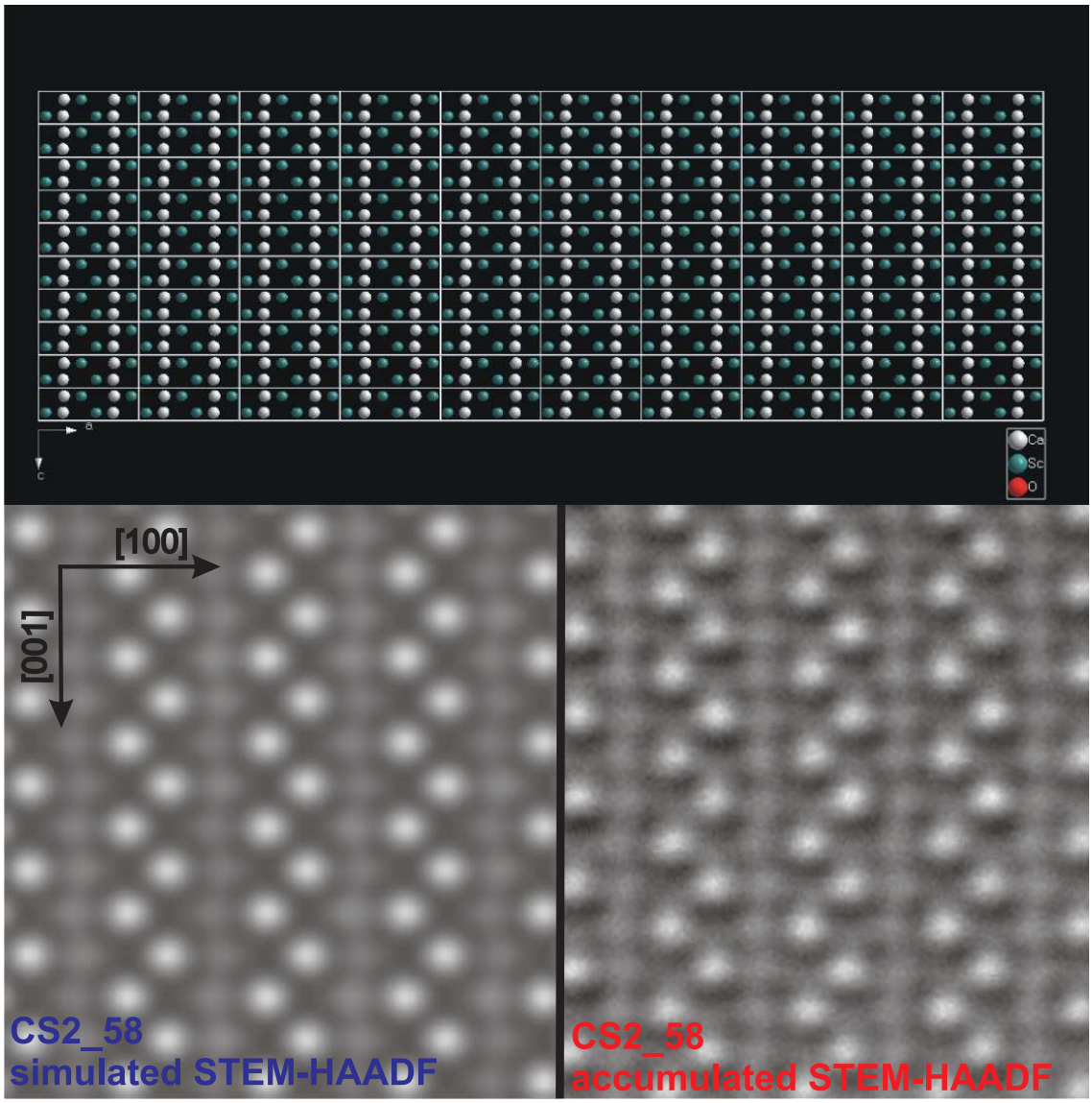

Figure 5.22: Top: (010) cluster of CS2 unit cells; only Ca (grey) and Sc (blue) atoms are illustrated. Bottom left: Simulated STEM-HAADF image. Bottom right: Accumulated STEM-HAADF image of a (010) CS2:Ce sample.

identifying the crystallographic sites and distribution in crystals. The method uses the effect that the X-ray emission is enhanced compared with kinematical conditions close to two-beam conditions in TEM [122]. The measurement characteristics are described in [84]. Thus, it was possible to determine the crystallographic position of trivalent cerium atoms in CS2:Ce. A comparison of the characteristic X-ray emission dependent on the sample orientation (with respect to the electron beam) reveals that trivalent cerium is located at the crystallographic site of calcium, as depicted in figure 5.25:

Integrated intensity ratios Sc K_α/Ca K_α (blue) and Ce L_α/Ca K_α (red) versus a scan across the (200) Kikuchi line (k_x/g_{200}) are depicted. The ratio Ce L_α/Ca K_α, with respect to the error bars, can be regarded as constant. The Sc K_α/Ca K_α instead shows different ratios for low k_x/g_{200} values. This is in accordance with simulated values (blue dashed line) that has been calculated using ICSC program [96].

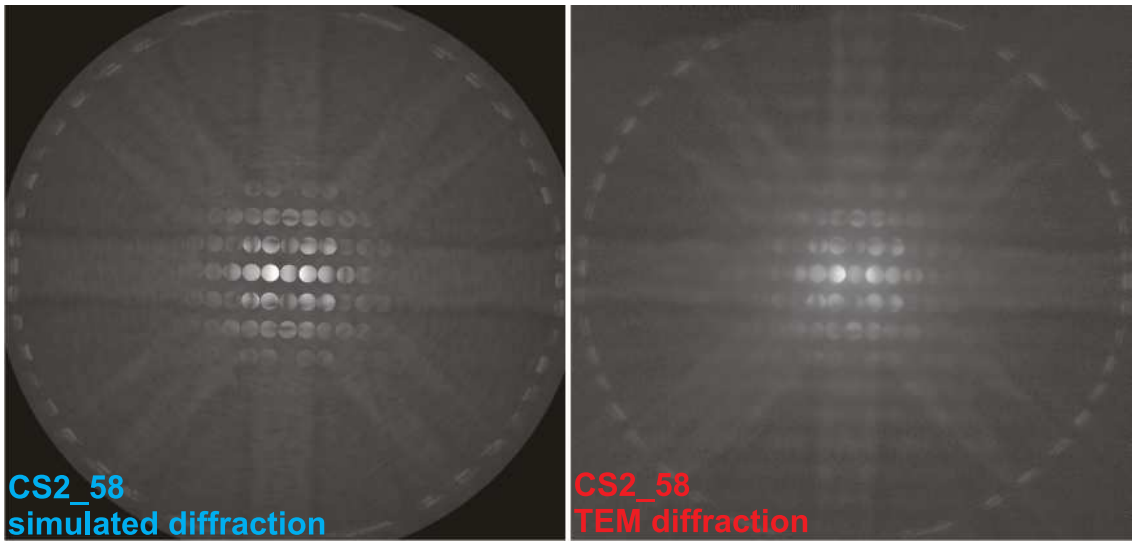

Figure 5.23: Simulated (left) and measured (right) diffraction pattern in ≈ [010] direction.

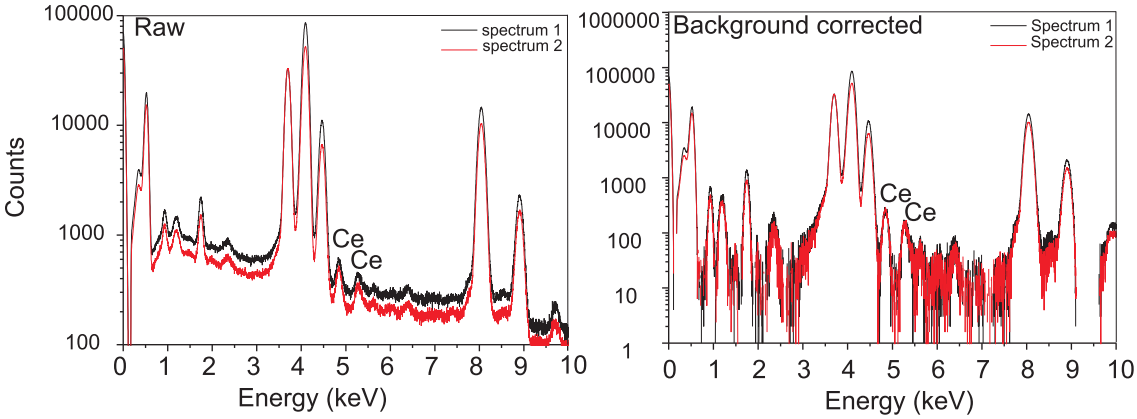

Figure 5.24: Two TEM-EDX spectra, raw (left) and background corrected (right), of the TEM sample CS2_58. Spectrum 2 is normalized to Ca K_α of spectrum 1. Spectrum 1 was measured at $k_x/g_{200} = 0.1$ and spectrum 2 at $k_x/g_{200} = 2.8$.

For this simulation the Ce atoms were assumed to be located on the Ca position. The measurement implies that cerium is incorporated homogeneously into the CS2 structure on Ca positions. Otherwise, if Ce was distributed onto the Sc position, the Ce L_α/Ca K_α ratio function would have a shape more similar to the Sc K_α/Ca K_α ratio function. The section 5.8 will discuss the valence state of cerium.

5.6.3 Crystal structure analysis of TSS

Single crystal structure refinement of a cerium-free and a cerium doped TSS SCF was performed by Dr. Irran (Technische Universität Berlin, Germany). Figure 5.26 depicts the unit cell of the Sr_3SiO_5 structure that was solved by Direct Methods and refined on F^2 using full-matrix least squares with SHELXL97 [112]. According to [26], the space group $P4/ncc$ (No. 130) was chosen, which was consistent with the systematic absences and confirmed by the successful solution of the structure. An overview of the lattice parameters and the atomic parameters is given in table 5.10.

Formula	Sr_3SiO_5			
Symmetry	tetragonal			
Space group	No. 130 ($P4/ncc$)			
Lattice constants (Å)	$a = 6.9353(3)$		$c = 10.7494(13)$	
Cell volume (Å^3)	517.03(7)			
Formula units/unit cell	4			
Density	4.766 g/cm^3			
Atom positions				
Atom	Wyck.	x	y	z
Sr(1)	4c	0.250	0.250	0.0092(1)
Sr (2)	8f	0.0624(1)	0.5624(1)	0.250
Si (1)	4b	0.250	0.750	0.000
O (1)	4c	0.250	0.250	0.2766(12)
O (2)	16g	-0.0925(9)	0.3502(10)	0.0933(6)

Table 5.10: Overview of the lattice parameters and the atomic parameters of the refined TSS structure.

Anisotropic displacement parameters (Å^2)						
Sr(1)	0.0117(6)	0.0117(6)	0.0071(7)	0.00000	0.00000	0.00000
Sr(2)	0.0098(5)	0.0098(5)	0.0067(6)	0.0001(4)	-0.0003(3)	0.0003(3)
Si(1)	0.0104(15)	0.0104(15)	0.007(2)	0.00000	0.00000	0.00000
O (1)	0.015(4)	0.015(4)	0.013(5)	0.00000	0.00000	0.00000
O (2)	0.012(3)	0.009(3)	0.008(3)	0.001(2)	-0.001(3)	0.002(3)

Table 5.11: Anisotropic displacement parameters of the refined TSS structure.

Refinement method	Full-matrix least-square on F^2
R indices (all data)	R1= 0.0733, wR2= 0.1387
Goodness-of-fit on F^2	1.236
Theta range	$3.79 - 29.96°$
Reflections collected	2163
Independent reflections	383
Crystal size	$0.61 \times 0.53 \times 0.21\,\mathrm{mm}^3$
Absorption coefficient	$31.002\,\mathrm{mm}^{-1}$

Table 5.12: Parameters for the crystal structure refinement based on TSS single crystal fibers, growth with mPD.

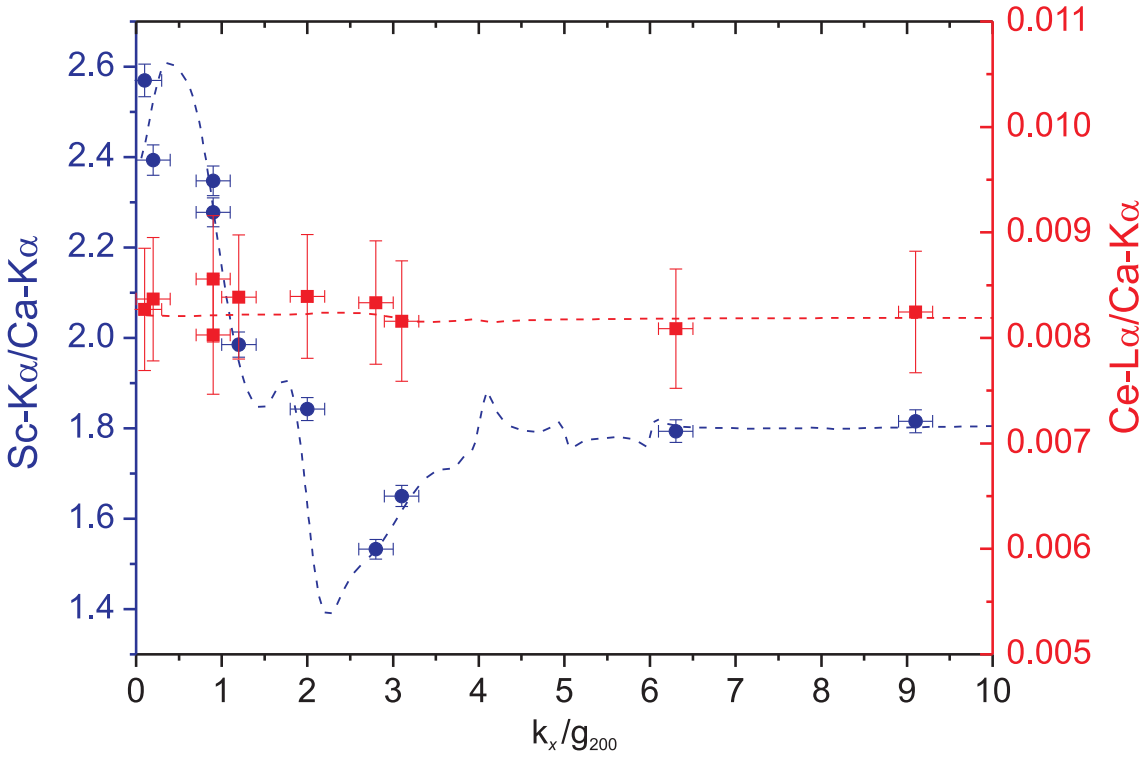

Figure 5.25: Ratios of the integrated characteristic X-ray intensities Sc K_α/Ca K_α (blue) and Ce L_α/Ca K_α (red) versus a scan across the (200) Kikuchi line (k_x/g_{200}). The dashed lines represent the simulated ionization cross section ratios.

The anisotropic displacement parameters of the refined TSS crystal structure and the parameters for the refinement are given in tables 5.11 and 5.12. The Si-O bond length of the tetrahedra (1.6376 Å) is larger than the length determined via room temperature neutron powder diffraction by Porras-Vázquez et al. [102]. The complete crystal data and structure refinement including the bond lengths will be published elsewhere.

According to the crystal structure analysis, it is possible to grow tristrontium silicate SCFs with suitable quality. Although the material has a low distribution coefficient for cerium (section 5.5), some cerium seems to be incorporated into the structure. This assumption is supported by the green color of the cerium doped SCF that was used for structure refinement. According to Mansmann the A_3MeX_5 struc-

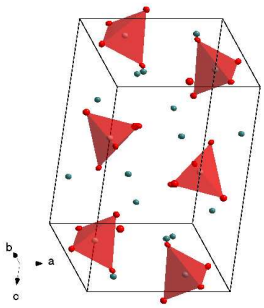

Figure 5.26: Unit cell in [131] direction of the Sr_3SiO_5 structure. The structure is a refinement from single crystal structure determination of a cerium free TSS SCF.

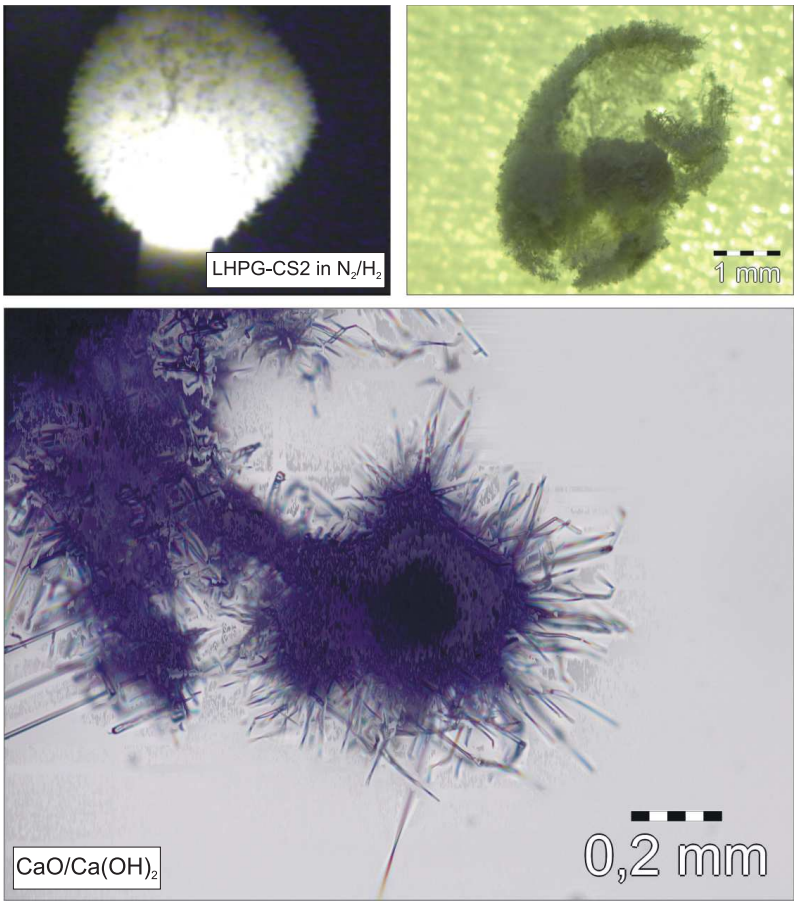

Figure 5.27: A CS2 SCF crystallizing in reducing atmosphere III (top left) shows dendritic crystallization covering the melt zone. The needles consist of $CaCO_3/Ca(OH)_2$ phases (top right, bottom).

ture type is stabilized by large cations on the A position [88]. This could be a reason for the low cerium distribution coefficient. However, spectroscopy (section 5.8) and the segregation (section 5.5) show that most cerium is not incorporated into TSS.

Cerium-free and cerium doped calcium scandate SCFs were measured in the same way, but are not shown within this work. Please note, according to the anisotropic displacement parameters changes, it seems reasonable that Ce^{4+} is incorporated on the Sc position.

5.7 LHPG melt zone studies

During crystallization of LHPG fibers, two phenomena occurred, which are related to interaction between the melt and gas phase:

Dendritic crystallization

Under strongly reducing atmospheres II and III (table 3.3) cerium forms almost exclusively Ce^{3+}, but the process became less controllable and strong evaporation was observed. Evaporating species from a calcium scandate melt condensed near the melt zone, forming a fine dendritic felt shielding partially the melt zone from laser

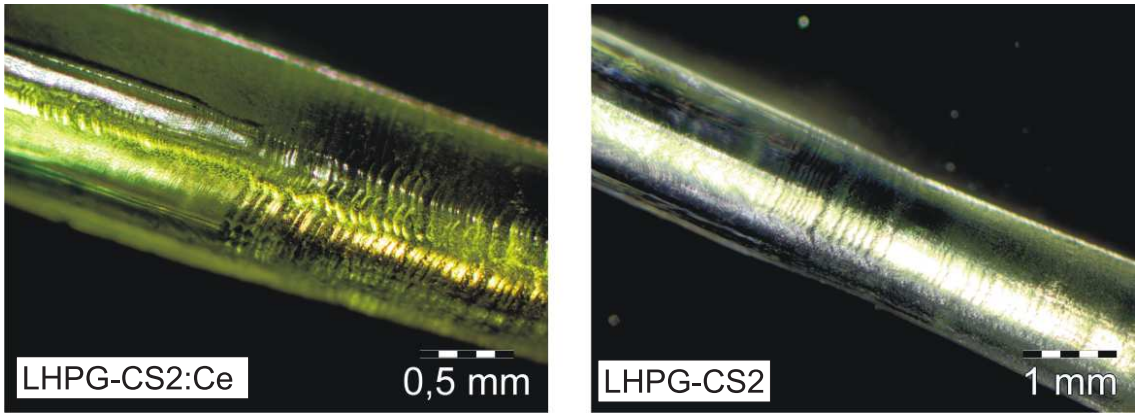

Figure 5.28: LHPG grown calcium scandate SCFs (left: $CaSc_2O_4$:Ce^{3+}; right: $CaSc_2O_4$).

irradiation (figure 5.27, left). The needle shaped crystals are $\approx 4\,\mu$m in diameter. This crystallization from the gas phase only occurred, if crystal growth had been undertaken in hydrogen containing atmosphere. Chemical analysis by ICP-OES indicated that calcium is the main constituent of this felt. Phase analysis was impossible due to its instability and minor quantity. It is striking that also during crystallization of cerium doped strontium yttrium oxide dendrites crystallized from the gas phase.

Factsage™ calculations revealed that the evaporating species react with other components of the atmosphere (mainly the rest oxygen $p_{O_2} \approx 2 \times 10^{-6}$ bar) under the formation of solid CaO ($> 98\,\%$) and small amounts of Ce_2O_3. It can be assumed that the dendrites consist of CaO, and under the influence of water and carbon dioxide from ambient air CaO disintegrates quickly to $Ca(OH)_2$ and $CaCO_3$. For the SCF CS2_51 the mass fractions of the SCF and the dendrites were weighted directly after LHPG run. The resulting mole fractions are $X_{\text{dendrites}} \approx 0.11$ and $X_{\text{scf}} \approx 0.89$. Approximately 11 % of the Ca content crystallized as dendrites. Taking the ICP-OES results for CS2_51, section 5.5, into account, this amount is the main body of overall evaporated calcium during crystallization. This implies, the dendritic formation is not only a minor effect, but rather a reference for the total evaporation from the melt.

Oscillatory thermocapillary convection

Figure 5.28 shows optical images of doped and undoped SCFs. During crystallization of both fibers oscillations of the temperature and the flow patterns caused diameter striations. Although, the fibers show homogeneous extinction under cross-polarized light and are free of visible cracks, the onset of this oscillations assign the end of steady state growth. Fiber fragments having been crystallized during oscillating convections showed a significantly lower amount of trivalent cerium. This is presented in the absorption measurements in section 5.8.2. When the convection of the melt was stationary, the fibers crystallized with planar side surface. Among other high melting oxides crystallized with the same LHPG apparatus, Sc_2O_3:Ce, Lu_2O_3, Sr_3SiO_5:Ce, only calcium scandate showed this oscillating convection. Within a strontium yttrium oxide melt oscillating convections could be induced through severe overheating of the melt. The following observations can be listed:

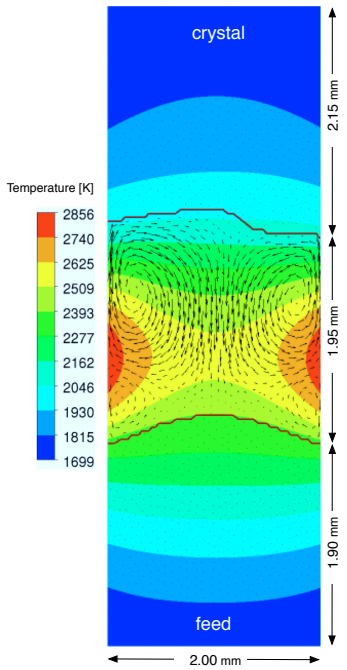

Figure 5.29: Numerical investigation: Temperature distribution and flow velocities in a quasi-LHPG setup. The crystal phase boundary does not match the isotherms.

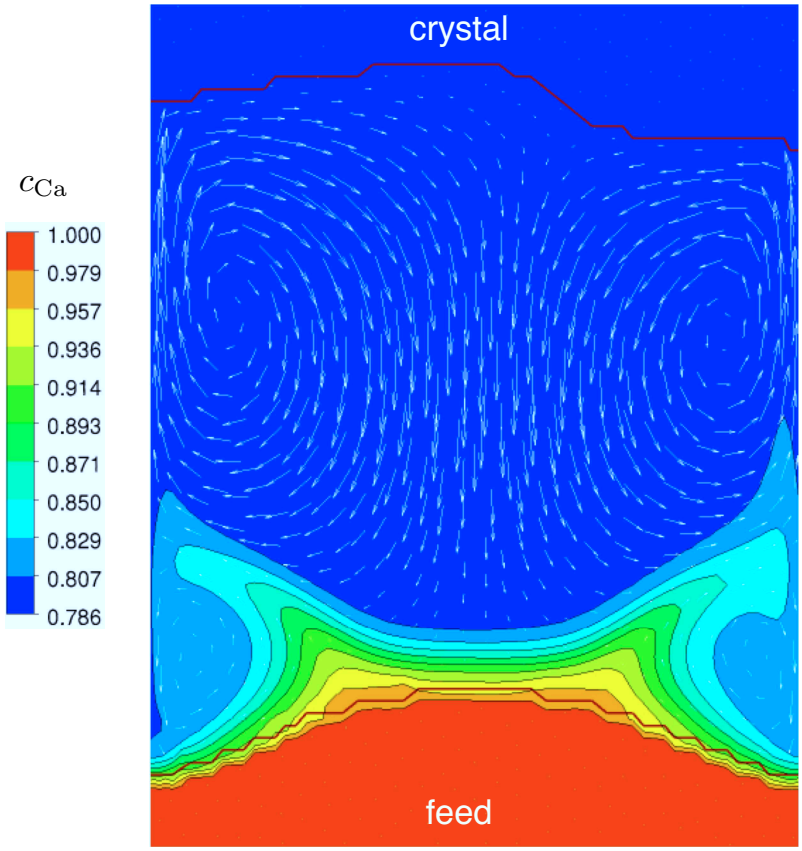

Figure 5.30: Numerical investigation: Flow velocities in a quasi-LHPG setup. The colors depict the distribution of Ca concentration within the melt (distribution after $t = 19.5\,\mathrm{s}$).

1. The temperature oscillations can be observed by a pyrometer. By video streaming the convective oscillations can be monitored. They result in frequent broadening and shrinkage of the zone length. 2. The observed frequency of the melt oscillations was $\approx 1\,\mathrm{Hz}$. 3. The oscillations in oxidizing atmospheres were stronger than in reducing atmospheres. 4. During crystallization in all installed atmospheres a characteristic onset of oscillations marked the end of steady state growth. 5. This onset occurred earlier with enlarged fiber diameter and reduced crystallization rate. 6. Once the onset of oscillations occurred, the time-dependent convection could not be eliminated, neither by adjusting the growth parameters nor by cooling and remelting.

In a LHPG setup Marangoni convection is dominant. According to Schwabe and Scharmann [107], oscillatory thermocapillary convection (OTC) results from exceeding some critical Marangoni number. The observed frequency of 1 Hz fits with the non-steady thermocapillary convection described by Jurisch and Loeser [69]. We could minimize the oscillation by reducing the fiber diameter and increasing the growth rate. Several effects resulted in these changes: 1. Evaporation was reduced because of a higher mass flow. 2. Fibers having been crystallized with smaller diameter showed a remarkably low amount of cracks. If these cracks are induced by thermal stress, they depend on the second derivative of the temperature field. The reduction of induced thermals stress could be related to a reduction of the radial temperature gradient for smaller diameters according to Prokofiev et al. [103].

We assume that a change in the melt composition caused these oscillations. As a preliminary step towards understanding, a numerical investigation of the melt zone was performed by Dr. Miller. A quasi-LHPG setup was constructed with 1 mm in diameter, a melt zone of $\approx 2\,\mathrm{mm}$, and an initial feed and crystal length of $\approx 3.5\,\mathrm{mm}$ and $\approx 0.5\,\mathrm{mm}$, respectively. The setup includes a moving phase boundary. The following boundary conditions were applied: $T_{\mathrm{bottom}} \approx 1700\mathrm{K}{+}1.0K\mathrm{t}$ and $T_{\mathrm{top}} \approx 1800\mathrm{K}{-}2.0\mathrm{K}t$ for the temperatures at bottom and top of the cylinder. A small symmetry deviation was implemented in the rate of heat flow. An evaporation (of calcium) at the free surface of the melt, temperature and concentration dependent, was implemented. Parameters were adjusted in such a way that the Ca concentration in the grown crystal was $\approx 20\,\%$ lower than in the feed.

The resulting temperature distribution and flow velocities are depicted in figure 5.29. Two convection rolls above and below T_{max} can be observed. The phase boundary between the melt and the feed is symmetrical and parallel to the isotherms. The crystal-melt boundary, on the other hand, is non-symmetrical and does not match the isotherms. This is induced by the symmetry deviation of the rate of heat flow, but amplified through the non-symmetric distribution of the Ca concentration, caused by convection and evaporation, in the vicinity of the interface. Because the melting point temperature depends on the calcium concentration via $T_{\mathrm{m}} = 2388\mathrm{K} - 4 \times 10^4 (1 - c_{\mathrm{Ca}})^3\mathrm{K}$ the interface is also strongly asymmetric. At the lower interface the Ca concentration (c_{Ca}) is almost equal to one and the interface correspond with the isoline of $T = 2388\,\mathrm{K}$. If the Ca content is reduced, the melting point of the material will be lowered. Figure 5.30 illustrates the calcium concentration distribution and flow velocities. The lines with constant Ca concentration are non-symmetrical. These deviations induce the non-symmetry in the crystal-melt phase boundary.

Summarizing the results of this preliminary numerical investigation, the convec-

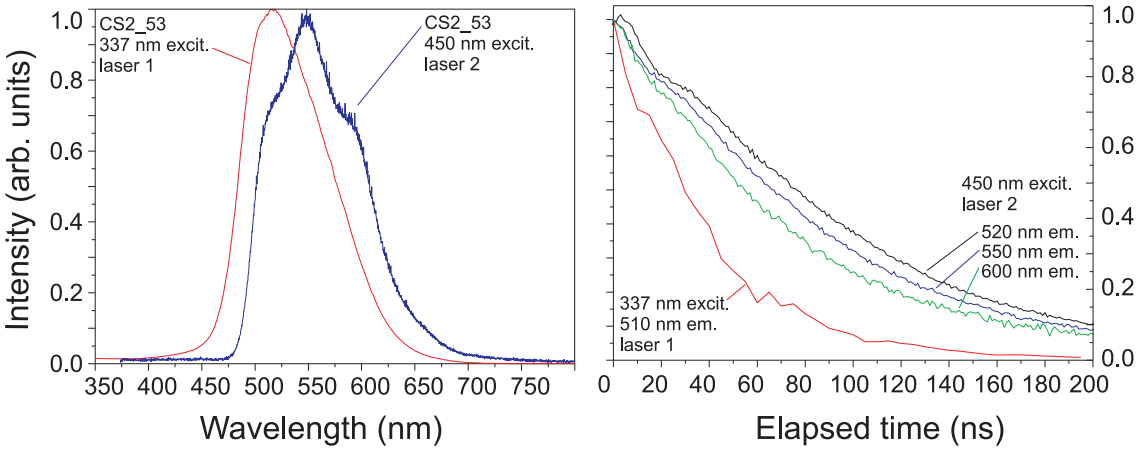

Figure 5.31: Laser fluorescence spectra and radiative lifetime of a CS2:Ce SCF. The fluorescence excitation was at 337 nm (laser1), 450 nm (laser2).

tion rolls in a Marangoni convection dominated system are stable. However, if a small deviation from azimuthal rate of heat flow is implemented and evaporation in the system occurs, these deviations will be amplified and induce a non-symmetry inside the crystal-melt boundary. An oscillation of this boundary could not be calculated. Note that the system investigated for the quasi-LHPG setup for this work is more complex than the systems described in [107, 69]. To investigate the interplay between composition shift and time-dependent flow velocities a comprehensive numerical investigation is required.

5.8 Spectroscopy

Spectroscopic measurements gave information on the homogeneity and crystal quality of the three materials. Through laser fluorescence measurements, the dependency of the Ce^{3+} concentration on the growth atmosphere could be revealed. The lifetime measurements indicated the 4f-5d transition of trivalent cerium within CS2, SY2, and TSS. Absorption measurements gave further information on the crystal quality. Combination of the spectroscopic measurements with elemental analysis and TEM provide a discussion on the Ce^{3+}/Ce^{4+} ratio.

5.8.1 Laser fluorescence and lifetime

Laser fluorescence and radiative lifetime measurements at room temperature were performed using three different laser setups (excitation properties) that are shown in table 3.6. The fluorescence emission spectra as well as their lifetimes depend on the pulse energy, the pulse duration, and the laser wavelength. Because of time limitation the exact influence of the excitation properties on the fluorescence was not investigated. But some differences are presented in the following: The left diagram in figure 5.31 shows the laser fluorescence of a CS2:Ce SCF that has been excited with 337 nm (laser 1) and 450 nm (laser 2). Both curves show a broad emission band. In the blue curve (laser 2) three different subbands with local maxima at 516 nm, 551 nm, and 584 nm can be detected. The red curve (laser 1) of the same sample that was measured using laser 1 setup reveals a broad 516 nm band with two

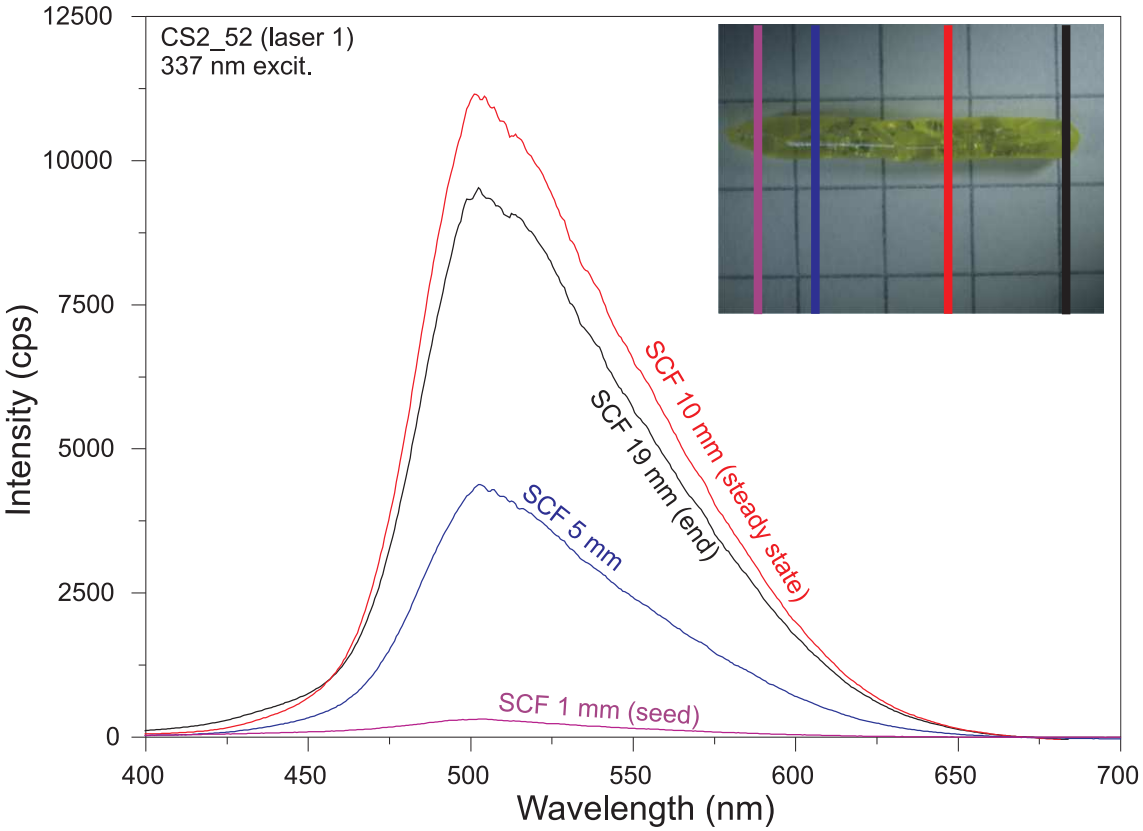

Figure 5.32: Laser fluorescence spectra of CS2:Ce SCFs that were crystallized in reducing atmosphere I. The fluorescence excitation was at 337 nm (laser 1). The colors of the curves represent spectra of different sections of the fiber (above right corner).

small shoulders at 551 nm and 584 nm. The radiative lifetimes (5.31, right diagram) differ from each other. For the laser 2 setup we obtained $\tau_{520\,\mathrm{nm}}$=81 ns, $\tau_{550\,\mathrm{nm}}$=78 ns, and $\tau_{580\,\mathrm{nm}}$=73 ns. The lifetime at 510 nm emission for the laser 1 setup is shorter ($\tau_{510\,\mathrm{nm}}$=42 ns). The range of the determined lifetimes in in the same order of magnitude, when compared to the isostructural SY2:Ce by Maninavannan et al. (37 ns at 300 K) [87].

The influence of the growth conditions

The influence of the crystal growth state on the cerium incorporation can be explained by figure 5.32: Fiber CS2_52 was crystallized in nitrogen atmosphere (reducing I). ICP-OES results revealed $k_{\mathrm{eff,ini}} \approx k_{\mathrm{eff,end}} = 0.5$ and quasi-steady state (table 5.4). At the beginning of the crystallization process (1 mm, purple curve), only a small amount of (trivalent) cerium is incorporated into the fiber because of $k_{\mathrm{eff,ini}} \approx 0.5$. Only a low fluorescence intensity could be measured. It is possible that the cerium concentration at the beginning of the fiber crystallization is further lowered through evaporation from the initial melt droplet. Additionally, the lower crystal quality at the first mm of the fiber crystal could be an explanation for the low fluorescence. Within the first millimeters of the fiber, the fluorescence intensity increased (blue curve) and reached a maximum at ≈ 10 mm, once steady was attained (red curve). Summarizing, figure 5.32 gives information on the cerium incorporation.

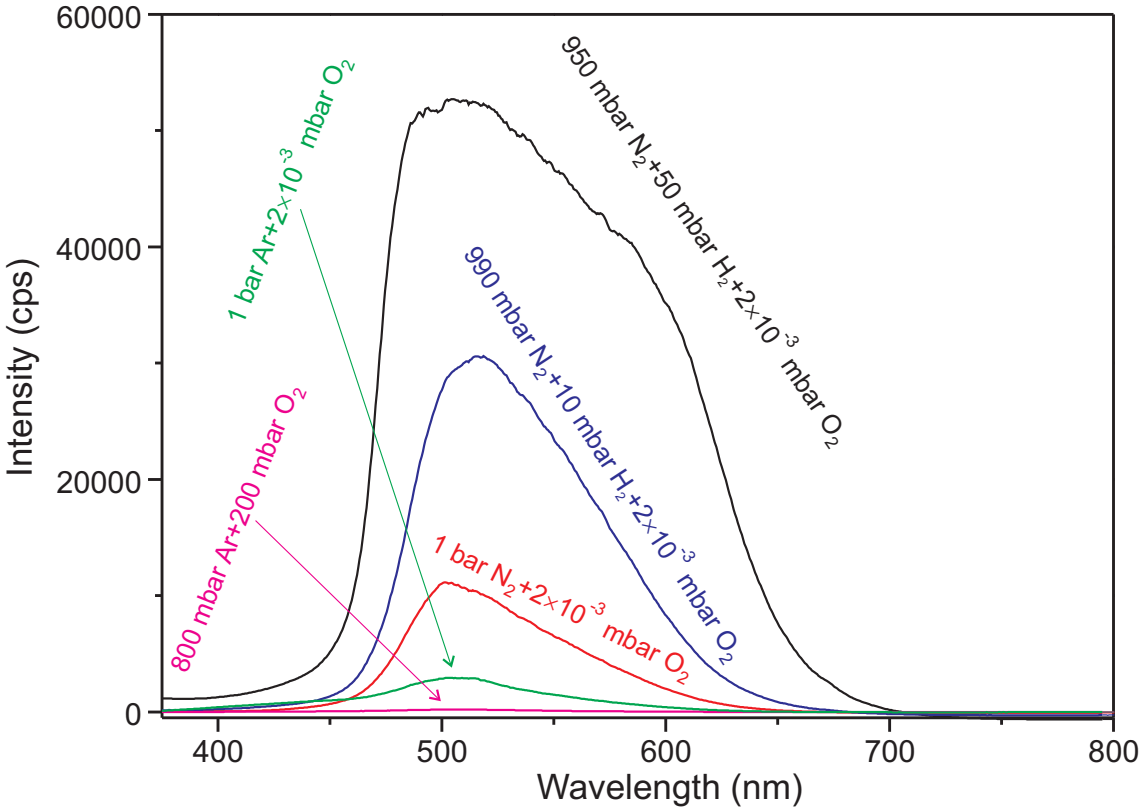

Figure 5.33: Laser fluorescence spectra of CS2:Ce SCFs that were crystallized in different atmospheres. The fluorescence excitation was at 337 nm (laser 1) [101].

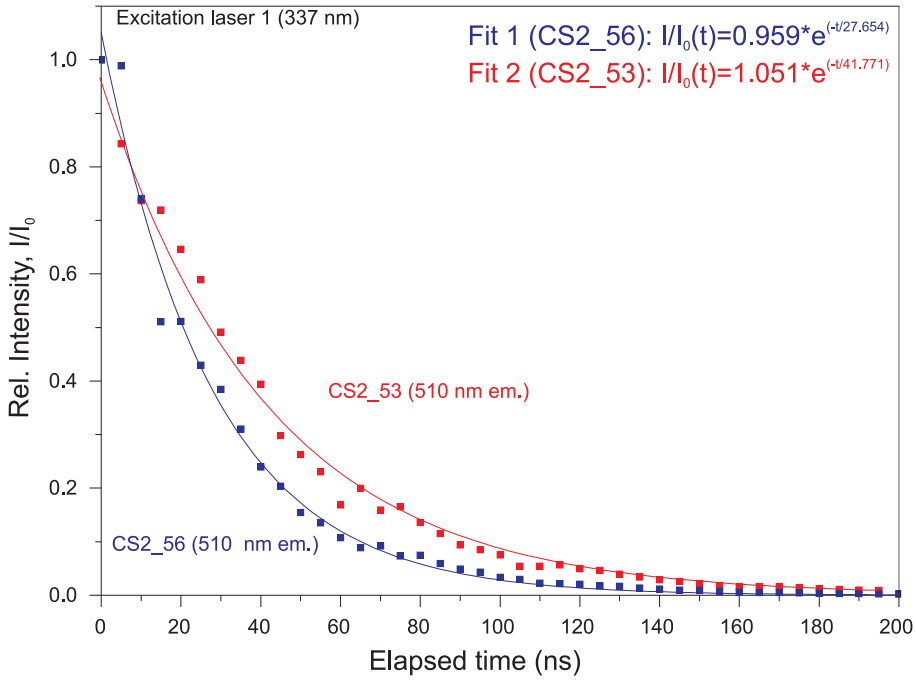

Figure 5.34: Radiative lifetime measurements of two CS2:Ce SCFs with $\approx 0.8\,\%$ (CS2_53) and $\approx 3.5\,\%$ (CS2_56) cerium concentration.

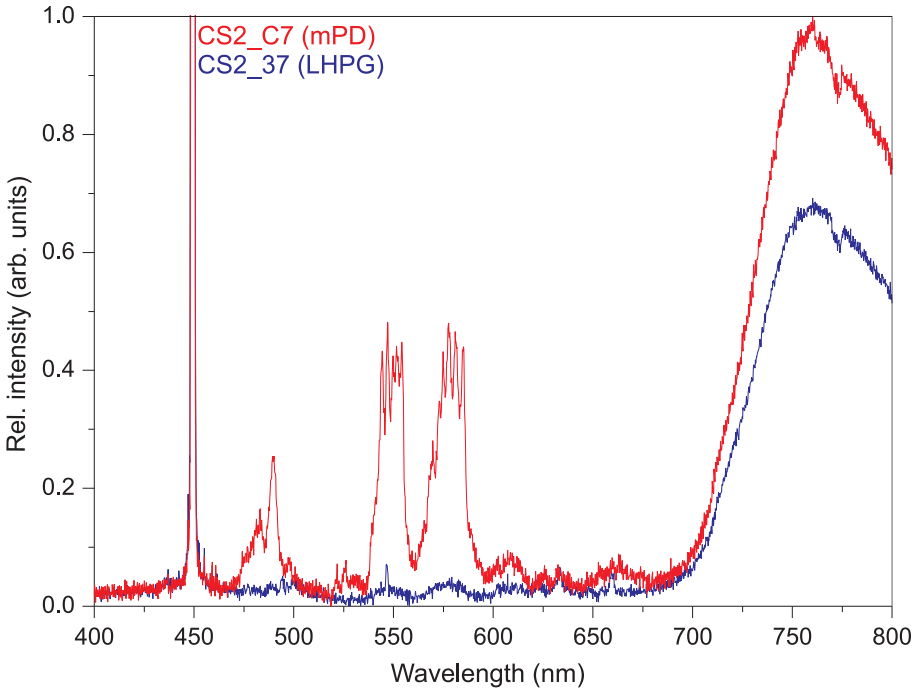

Figure 5.35: Laser fluorescence spectra of cerium-free CS2 SCFs that were crystallized using LHPG (blue) and mPD (red). The fluorescence excitation was at 450 nm (laser 2).

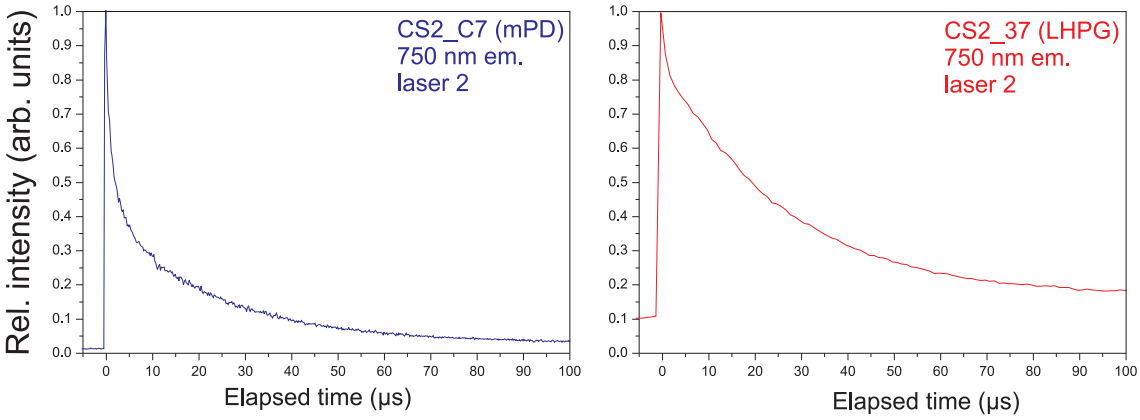

Figure 5.36: Radiative lifetime measurements of cerium-free CS2 SCFs that were crystallized using LHPG (red) and mPD (blue). The fluorescence excitation was at 450 nm (laser 2.)

Note that all fluorescence measurements in this sections are either caused by trivalent cerium or lattice defects. No Ce^{4+} fluorescence was detected. The dependency of the Ce^{3+}/Ce^{4+} ratio on the atmosphere is explained by figure 5.33: By investigating CS2:Ce SCFs that were crystallized in different atmospheres (see table 3.2) the relation between the oxygen fugacity and the resulting content of trivalent cerium becomes vivid. Figure 5.33 shows the laser fluorescence (excitation at 337 nm, laser 1) of SCFs, grown in the atmospheres that were already discussed regarding the fugacity and deviation from the weighed portion in sections 5.1 and 5.5. All fibers were grown with the same crystal parameters, except of the atmosphere. The depicted fluorescence curves represent the maximum intensity (steady state) according to the intensities in figure 5.32. Especially the black luminescence curve of a fiber, crystallized in the reducing atmosphere with 5 % hydrogen (reducing III), has the same shape as the curve of the $CaSc_2O_4$:Ce phosphor that has been investigated by Shimomura et al. [113]. Apparently, the doping of trivalent cerium into the CS2 structure works without charge compensation of alkali metal ions. The broadened structure with its maximum at 515 nm is due to the ground state spliting of the Ce^{3+} ion [113]. The amount of trivalent cerium is strongly influenced by the oxygen fugacities of the atmospheres (as it is also demonstrated by the Factsage™ calculations in 5.1). The laser fluorescence is lowered with higher values of f_{O_2} and cannot be detected in a SCF that crystallized in an oxidizing atmosphere (purple curve in figure 5.33). Crystallizing in 5N nitrogen atmosphere (reducing I) caused a significant luminescence (red curve), but a certain amount of Ce^{4+} had to be taken into account. In combination with elemental analysis (ICP-OES), the cerium incorporation due to segregation and evaporation, and the dependency of the cerium valence on f_{O_2} the Ce^{3+}/Ce^{4+} ratio can be estimated (such as mainly Ce^{3+}, mainly Ce^{4+}). As of this writing, a quantification of this ratio was not possible.

The cerium concentration affects the radiative lifetime, as demonstrated in figure 5.34. Both fibers, CS2_53 and CS2_56, were crystallized in reducing atmosphere I with identical crystal growth parameters. Shorter lifetimes occurred, when the amount of trivalent cerium was increased. Exponential decay fit revealed the lifetimes. Compared to fiber CS2_53, fiber CS2_56 has ≈ 3.5 % cerium and the lifetime was dropped from ≈ 42 ns to ≈ 28 ns.

Figure 5.35 shows the emission spectra of cerium-free SCFs that were crystallized using LHPG (blue) and mPD (red). The signal at 450 nm is the excitation wavelength (laser 2). Although the luminescence intensities are low compared to the strong Ce^{3+} 5d-4f luminescence shown previously, several emission bands can be determined. Three emission bands are located at 480 nm, 550 nm, and 580 nm. These bands might arise from a cerium impurity. Their lifetime are within the same order of magnitude, if compared to the 4f-5d emission bands that are presented above. A broad emission band can be detected between $\approx 700 - 800$ nm. This near-infrared band (NIR) can be detected in cerium doped SCFs as well. The emission bands emitted from the sample CS2_C7 that was crystallized in mPD setup showed higher intensities. The radiative lifetime measurements of NIR bands are shown in figure 5.36. The emission is probably caused by calcium scandate lattice defects.

Laser fluorescence and lifetime measurements of SY2

Laser fluorescence emission and radiative lifetimes of SY2:Ce SCFs can be compared to calcium scandate measurements: In figure 5.37, the laser fluorescence spectra of

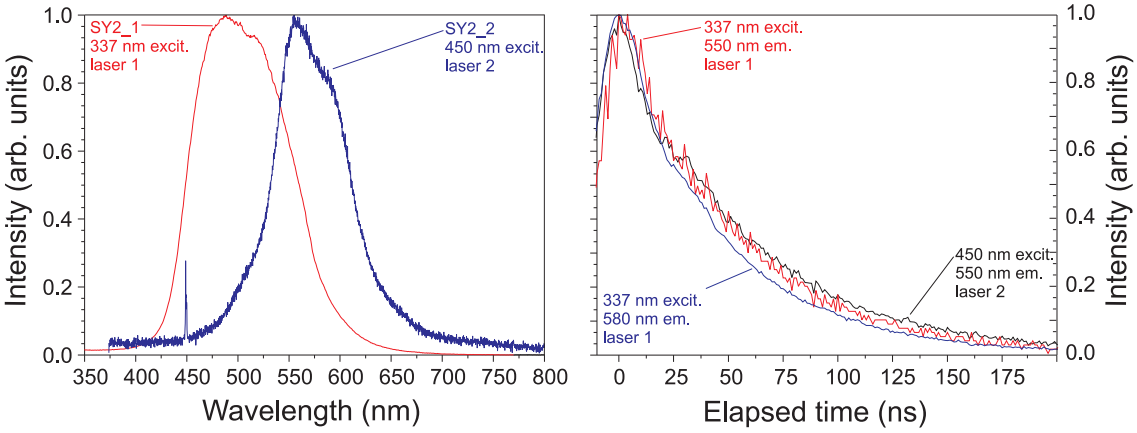

Figure 5.37: Laser fluorescence spectra and radiative lifetime of two SY2:Ce SCFs. The fluorescence excitation was at 337 nm (laser 1) and 450 nm (laser 2).

two strontium yttrium oxide crystal fibers, SY2_1 and SY2_2, are given. Measurements were done with different setups (laser 1 and laser 2). When excited with 337.1 nm (laser 1), a broad emission band occurred with a peak wavelength at 489 nm. When excited with 450 nm (laser 2), an emission band with subbands at $\approx$ 505 nm, $\approx$ 556 nm, and $\approx$ 588 nm occurred. Both fluorescence curves vary because of different excitation properties (table 3.6). These differences are stronger, as in the case of the calcium scandate sample (figure 5.31). The radiative lifetimes show a single exponential decay with $\tau_{550\,\mathrm{nm}}$=46 ns, $\tau_{580\,\mathrm{nm}}$=46 ns when excited with 337 nm (laser 1), and $\tau_{550\,\mathrm{nm}}$=65 ns when excited with 450 nm (laser 2).

The SY2:Ce laser fluorescence and lifetime, which is depicted in figure 5.37, will be compared to the work by Manivannan et al. [87], who investigated the nature of luminescent centers of this material: The authors describe a blue emission band, located at $\approx$ 475 nm, and a green emission band, located at $\approx$ 520 nm for λ_{ex} = 310 nm. They refer the blue band to the Ce^{3+} 4f-5d transition and the green band to a $Ce^{4+} - O^{2-}$ charge transfer with ($\tau_{520\,\mathrm{nm}}$=275 μs). This luminescent transfer has priorly been reported by Danielson et al. for the material Sr_2CeO_4 [25]. The luminescence curves in figure 5.37 do not resemble the described $Ce^{4+} - O^{2-}$ charge transfer because of the different lifetimes. No evidence for Ce^{4+} luminescence was found. Both monitored fluorescence curves and their lifetimes are similar to the Ce^{3+} transition, described by Manivannan et al. [87] ($\tau \approx$ 46 ns). This indicates that Ce^{3+} is incorporated on the Y position in strontium yttrium oxide, as it is described by Blasse et al. for the powder [13]. The SY2:Ce crystal fibers were crystallized in inert and reducing atmosphere and probably do not show any tetravalent cerium. This is stated by the calculation of the cerium valence (figure 5.4).

Laser fluorescence and lifetime measurements of TSS

The Ce^{3+}/Li^{+} co-doped light phosphor shows a strong broad emission band at 465 to 700 nm, when excited under 360 nm [65]. In figure 5.38, the sample TSS_p4_mpd-_04 that was crystallized in inert atmosphere using mPD setup reveals a similar fluorescence spectrum. It can be shown that, even without co-doped lithium ions, the luminescence properties are similar to the light phosphor [65]. The different sub band structures of the TSS_p4_mpd_03 and TSS_p4_mpd_04 fluorescence could be

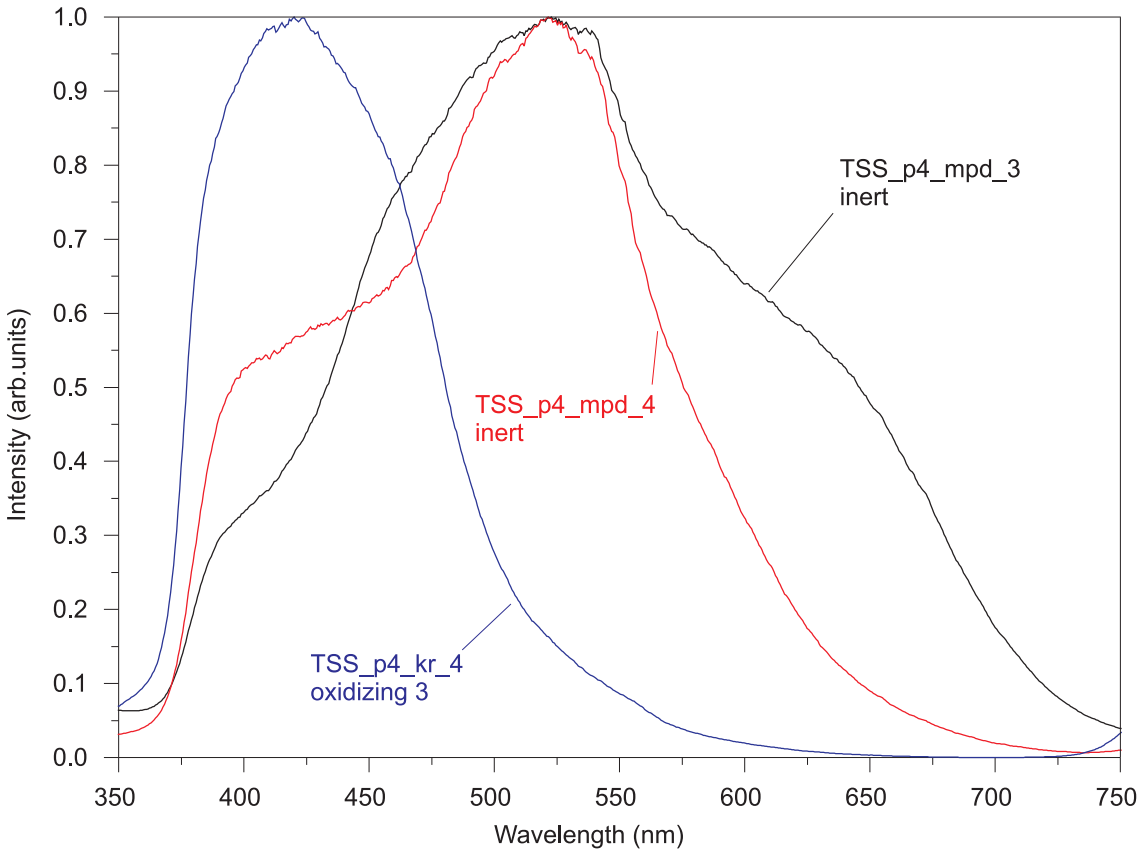

Figure 5.38: Laser fluorescence spectra of TSS:Ce crystal fibers that were grown using mPD (TSS_p4_mpd_03, TSS_p4_mpd_04) and LHPG (TSS_p4_kr04). The fluorescence excitation was at 337 nm (laser 1).

arising from different Ce^{3+} concentration (atmosphere, segregation). The resulting intensity-shift of the subbands, located at $\approx$ 405 nm, $\approx$ 460 nm, $\approx$ 520 nm, and $\approx$ 630 nm, is discussed in [66]. Jang et al. report the fine-tuning of TSS:Ce^{3+}/Li^{+} luminescence by manipulating the Ce concentration.

The LHPG sample TSS_p4_kr04 has been crystallized in oxidizing atmosphere (oxidizing III) and showed an emission peak at $\approx$ 410 nm. As it is discussed in section 5.4, LHPG TSS:Ce fibers that were grown in oxidizing and inert atmospheres are inhomogeneous (figure 5.11). The emission band is presumably not related to trivalent cerium, incorporated into tristrontium silicate. The emission peak of the sample TSS_p4_kr04 at $\approx$ 410 nm could be related to the formation of $SrCeO_3$ or Sr_2CeO_4 phases including tetravalent cerium. For the latter phase, the luminescence arising from a Ce^{4+} charge transfer is reported [120].

5.8.2 Transmission and absorption

Ground state absorption (GSA) of CS2:Ce SCFs were measured by Fechner [39] using a double-beam spectrophotometer (Varian Cary 500 UV-VIS, Agilent, USA). Figure 5.39 depicts two GSA curves (absorption coefficient α versus wavelength) that were crystallized with similar growth conditions. Fiber CS2_10 was crystallized with a higher crystallization rate ($\nu_{\text{seed}} = 2.0$ mm/min, $\nu_{\text{feed}} = 0.5$ mm/min), compared to CS2_15 ($\nu_{\text{seed}} = 1.2$ mm/min, ν_{feed} =0.6 mm/min). During crystallization of CS2_10,

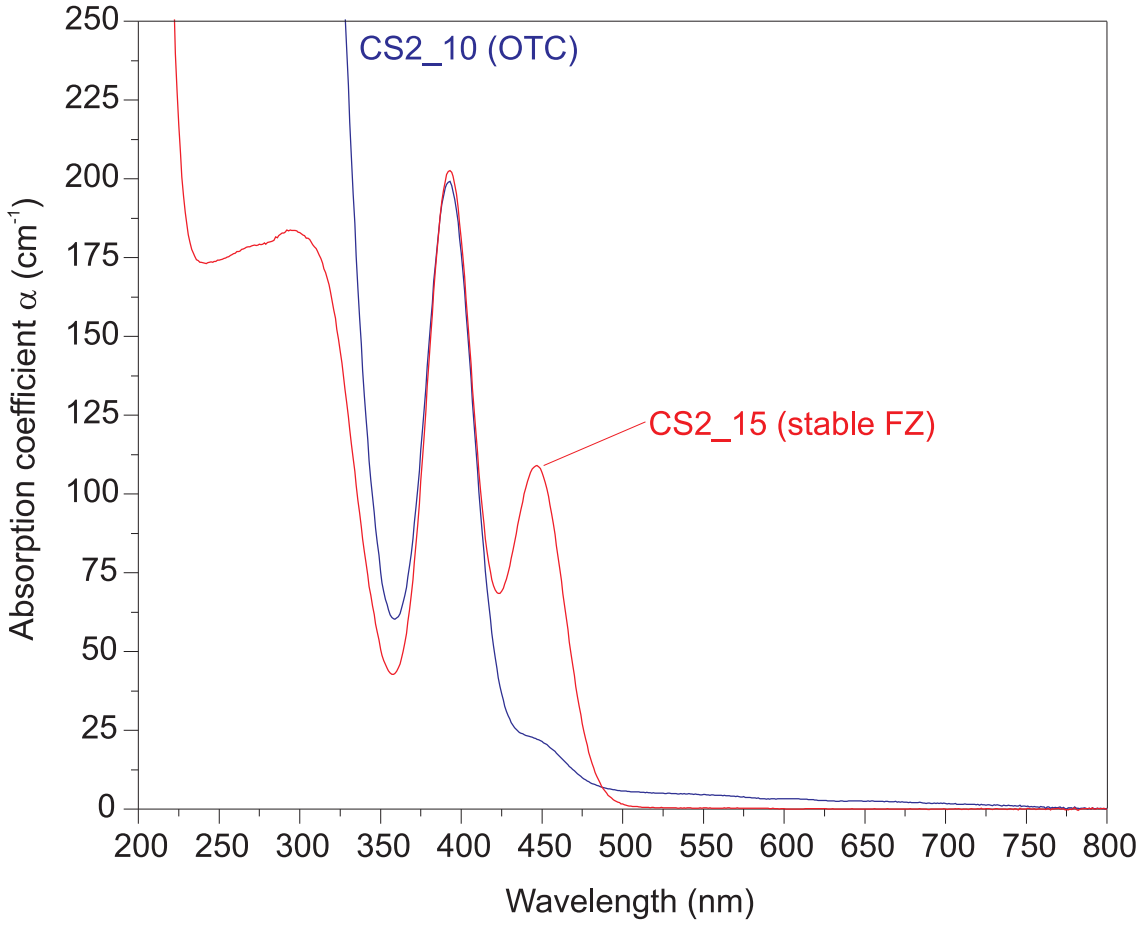

Figure 5.39: Ground state absorption of two CS2:Ce SCFs that has been crystallized in Ar atmosphere from a time-independent melt zone (CS2_15) and a melt zone under influence of OTC (CS2_10). This absorption measurement was performed by Fechner [39].

a spontaneous onset of oscillating thermocapillary convection (OTC) occurred. The convection inside the melt zone became time-dependent. This phenomenon is discussed in section 5.7. Apparently, the OTC causes a significant change concerning the incorporation of trivalent cerium into the fiber. As a result, the GSA spectra of both fibers vary from each other: The GSA of CS2_15 shows an absorption band located at 450 nm. This band is the Ce^{3+} 4f-5d transition, as it is discussed by Shimomura [113]. A second absorption band with a maximum at 395 nm occurs in both fibers. Fechner assigns this band to a Ce^{4+}-O^{2-} charge transfer [39]. This charge transfer is discussed for the material $SrY_2O_4Ce^{3+}$ [87]. Moreover, CS2_15 is transparent for wavelengths greater than 500 nm, for CS2_10 α decreases slowly and is close to zero at 750 nm. In the UV region (250-300 nm), sample CS2_10 absorbs stronger than sample CS2_15. Both fibers contain trivalent and tetravalent cerium, but the ratio Ce^{3+}/Ce^{4+} within fiber CS2_15 is greater. If a crystallizing fiber is periodically remelted at the crystallization front (OTC), this region will become cerium depleted because of k_{eff} <1. Therefore, a smaller total amount of cerium in fiber CS2_10 can be expected. On the other hand, a composition change within the melt zone can cause OTC. This composition change could be caused by overheating of the melt zone that is demanded for higher crystallization rates (avoidance of

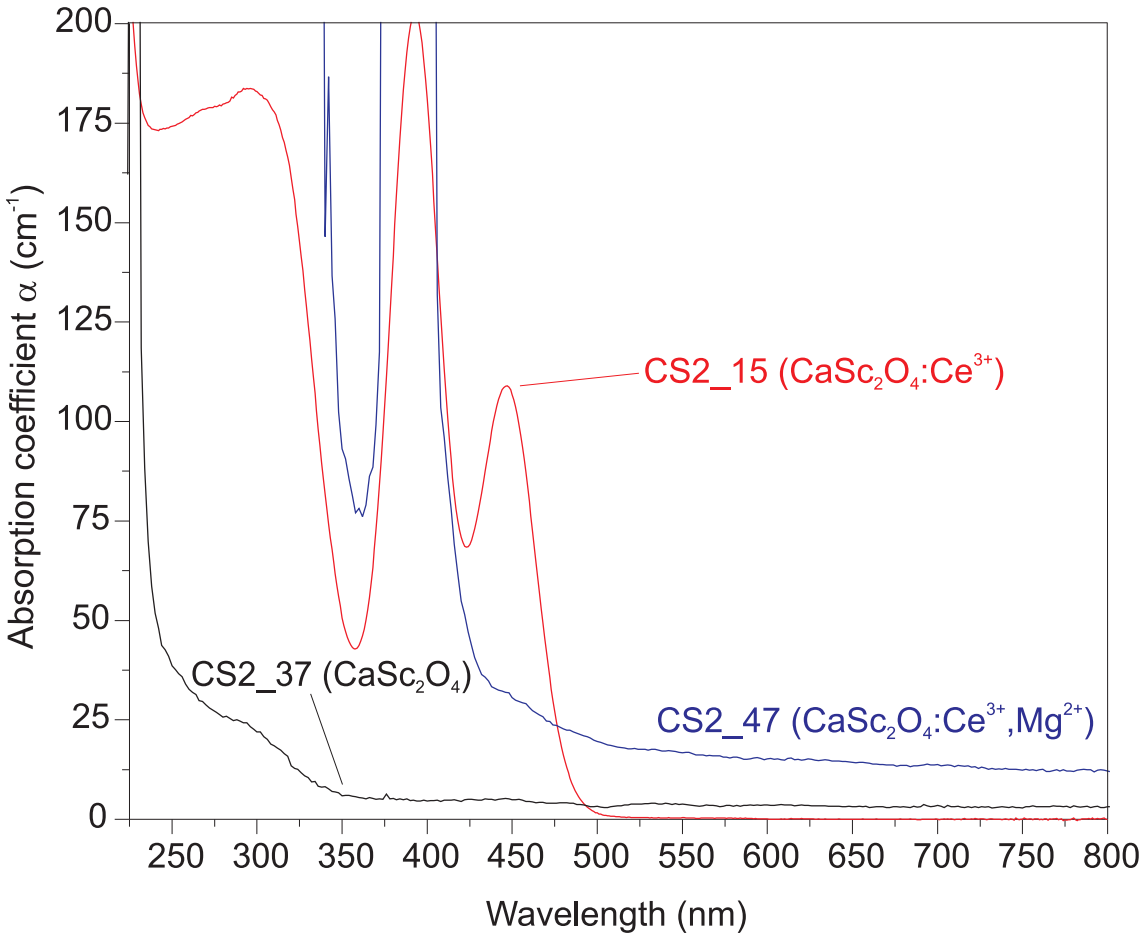

Figure 5.40: Ground state absorption of three CS2:Ce SCFs with different compositions of the feed material. The CS2_15 feed contains ≈ 1 % cerium (P3), CS_47 ≈ 0.3 % cerium, ≈ 0.3 % magnesium (P4), CS_47 is cerium-free (P1). Powder compositions are given in table 3.1. Note that the curve CS2_15 taken from figure 5.39 as reference.

freezing of the melt zone). A satisfying explanation for the interaction of OTC and Ce^{3+}/Ce^{4+} ratio is not yet clear. k_{eff} is a function of the molar diffusivity. If a different diffusion coefficient for Ce^{3+} and Ce^{4+} was assumed, the Ce^{3+}/Ce^{4+} ratio would be a function of the crystal growth rate ν_{scf}. Thus, this ratio would not be constant, if OTC occurred. It is noteworthy that fiber CS2_15 reveals an absorption behavior that is desired for a cerium containing laser material (strong Ce^{3+} absorption band and transparent above 500 nm wavelength).

Between 250 and 350 nm, CS2_37 only shows weak absorption (figure 5.40). This band will be stronger, if cerium is incorporated (CS2_15, CS2_47). On the one hand, this band matches the Ce^{3+} absorption also occurring in YAG:Ce^{3+} [56]. On the other hand, oxide structures containing Ce^{4+} show strong absorption in this wavelength region [52]. Therefore, this band cannot be directly connected either to Ce^{3+} or to Ce^{4+} absorption.

Feed CS2_47 has been prepared from powder P4 (table 3.1). ≈ 0.3 % magnesium had been substituted in exchange for scandium, according to ≈ 0.3 % cerium in exchange for calcium. The SCF that was crystallized with the same parameters, as used for CS2_15, shows significant absorption at 395 nm (Ce^{4+}-O^{2-} CT) and only

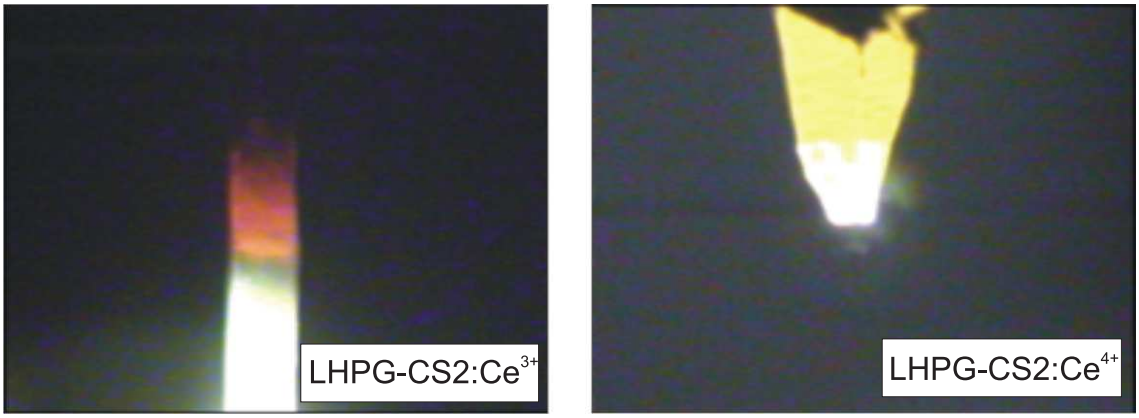

Figure 5.41: Two cerium doped calcium scandate fibers during crystallization in the LHPG furnace. The red (left) and yellow (right) glow are arising from the different valence of the dopant.

weak absorption at 450 nm. Magnesium is not incorporated into the fiber (ICP-OES measurements), it is either incompatible or, more likely, evaporating from the melt zone. Thermodynamic calculation revealed high Mg and MgO fugacities. Therefore, a co-doping with magnesium is not suitable for LHPG growth.

The incorporation of Ce^{3+} into the CS2 crystal can be observed indirectly during LHPG growth. Figure 5.41 depicts two CS2:Ce SCFs. The left fiber, depicted during an early LHPG stage, shines with a red glow. This is related to a high Ce^{3+}/Ce^{4+} ratio. The fiber was crystallized in nitrogen atmosphere (reducing I). This glow could be related to high-temperature absorption shift. Trivalent cerium absorbs at 450 nm (figure5.39); therefore fibers at room temperature are green colored. If the fiber absorbs longer wavelengths at higher temperatures, the color will also shift to longer wavelengths (complementary color). Therefore, a crystal fiber, illuminated by the thermal radiation of the melt zone, would shine in red color instead of green. The fiber, depicted on the right, contains mainly tetravalent cerium. No red shine occurred during crystal growth. Note, that the colors of fibers at room temperature depend on the Ce^{3+}/Ce^{4+} ratio. Whereas Ce^{3+} rich fibers are yellow-greenish, the color of Ce^{4+} rich fibers are pale green. This observation fits to the different absorption of CS2:Ce^{3+} and CS2:Ce^{4+}.

Ground state absorption of a SY2:Ce SCFs is shown in figure 5.42. In comparison to the CS2:Ce absorption, the Ce^{4+} band shifts to ≈ 10 nm longer wavelengths (410 nm), while the Ce^{3+} band shifts to $\approx$ 30 nm longer wavelengths (480 nm). Within CS2, trivalent cerium will be incorporated on the Ca position, tetravalent cerium presumably on the Sc position. In SY2, both ions, Ce^{3+} and Ce^{4+}, will be incorporated on the Y position. Therefore, the Ce^{3+} band should shift to longer wavelengths (as it is described in [13]). The Ce^{4+} band, however, should remain on approximately the same position because of the same coordination sphere (CeO_6 polyhedra, section 2.3.1). The Ce^{3+} absorption shifts to longer wavelengths result in a yellow-red color of the SY2:Ce crystals. Because of the high overlap of absorption and emission of SY2:Ce the material does not seem to be an appropriate material for laser (self-absorption, ESA).

Although the Ce^{3+}/Ce^{4+} ratio could not be quantified, it could be estimated by combining elemental analysis (total Ce), TEM measurements (Ce position), fluores-

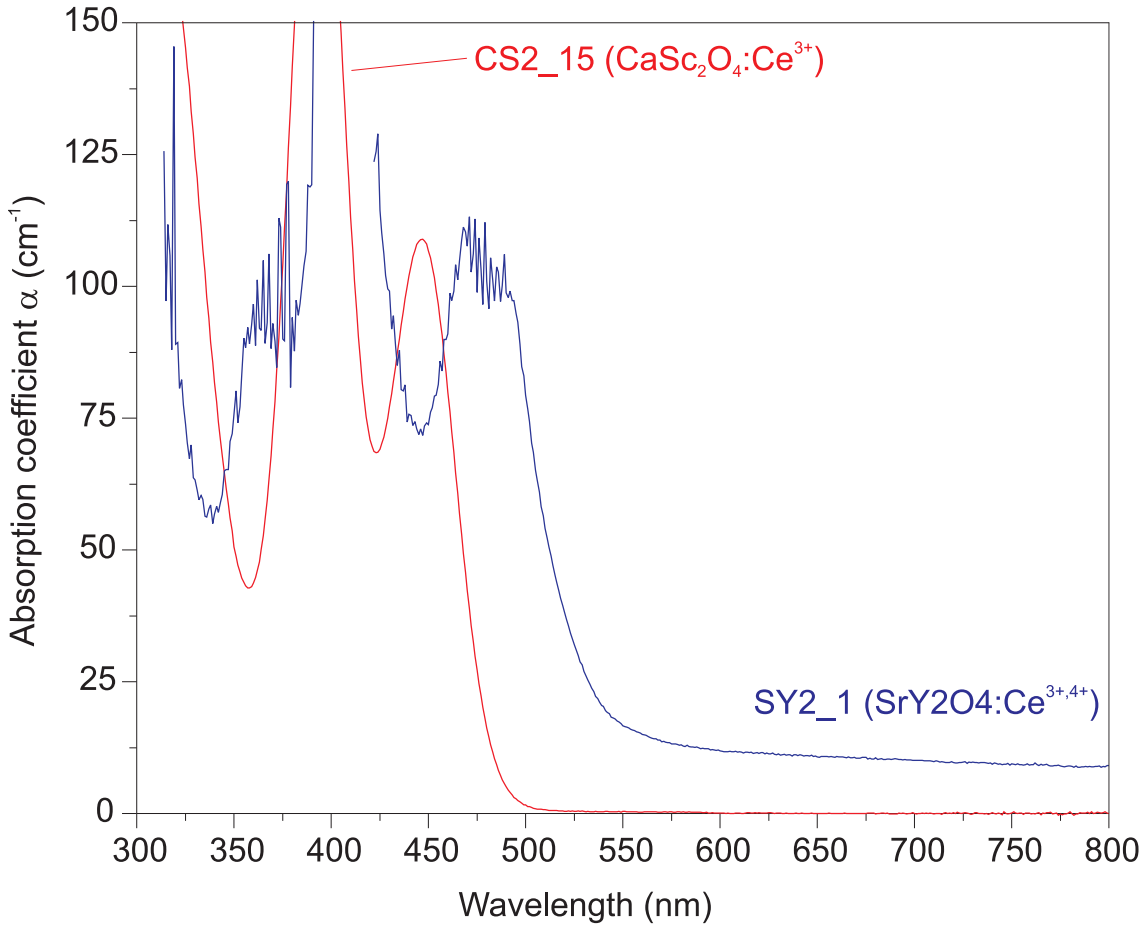

Figure 5.42: Ground state absorption of a SY2:Ce SCFs that has been crystallized in Ar atmosphere; the absorption of CS2_15 is depicted as reference from figure 5.39.

cence and absorption measurements (relative intensities). King et al. demonstrate a method to determine the Ce^{3+}/Ce^{4+} ratio by examining the Ce L_3-edge XANES spectra [73]. The cerium concentrations in titanate samples match the concentrations of SCFs in this work (≈ 0.6 wt.%). In cerium doped calcium scandate, SCFs the cerium valence is strongly affected by f_{O_2} during crystallization. As of this writing, a comprehense theory for the interaction of Ce^{3+}/Ce^{4+}, Ca vacancies (and possible O interstitials), and their dependency on the growth atmosphere is still desirable.

Chapter 6

Conclusion

This work demonstrates the significance of fiber crystal growth techniques to the investigation of new materials with high melting points. Calcium scandate, strontium yttrium oxide, and tristrontium silicate were successfully grown. Calcium scandate, doped with trivalent cerium, is a promising material for laser applications. The growth parameters were optimized for the laser-heated pedestal growth technique. Pure nitrogen atmosphere is a reasonable choice for the growth process. Under such conditions the amount of species evaporation (mainly CaO and CeO) is limited, and a significant amount of trivalent cerium is incorporated into the material. The ratio between trivalent and tetravalent cerium can be manipulated by the oxygen fugacity. This was predicted by thermodynamic calculations and experimentally confirmed by optical spectroscopy. Transmission electron microscopy revealed that trivalent cerium is incorporated on the calcium position. Despite the influence of the dopant, a high crystal quality can be achieved. Fluorescence and absorption measurements reveal properties that match the requirements for a laser material within the green light region. The occurrence of oscillating convection in the melt could be minimized by reducing the evaporation from the melt. Through reduced evaporation, steady state growth of the fibers is possible. This steady state, the crystallization with constant mass flows from the feed into the melt and from the melt into the crystal fiber, is limited by the onset of oscillating thermocapillary convection. In comparison with the micro-pulling-down technique, the LHPG technique is superior for the growth of cerium doped calcium scandate. The high thermal gradients in the LHPG setup support rapid growth rates and by this the incorporation of trivalent cerium. In mPD growth, the re-condensation of evaporated calcium oxide from the melt is disadvantageous for the crystal quality.

For a better understanding of the growth process the unknown phase system calcium oxide–scandium oxide was investigated. A phase system with two eutectic points on either side of the only intermediate phase calcium scandate was revealed. Moreover, the congruent melting of calcium scandate was confirmed. The isostructural material strontium yttrium scandate was grown with the same crystal parameters. Single crystal fibers, doped with trivalent cerium on the yttrium position, were fabricated for the first time. Absorption and fluorescence measurements revealed yellow-green luminescence generated by trivalent cerium. The evaporation of mainly SrO and Sr was calculated and confirmed with high-temperature mass spectrometry. Single crystal fibers of cerium doped tristrontium silicate can be grown using the micro-pulling-down method. In inert argon atmosphere and with a pulling

rate of 0.25 mm/min, crack-free fibers can be crystallized up to 0.5 mm in diameter. The fibers were used for crystal structure refinement. The distribution coefficient for cerium into the host material is remarkably lower, if compared to the cerium incorporation into calcium scandium oxide and strontium yttrium oxide. Tetravalent cerium is not incorporated into the structure. The LHPG method is not suitable for this material because of evaporation from the free surface.

For each material the significance of phase relations to the crystal growth process is demonstrated. Thermodynamic calculation revealed evaporating species. These species could be confirmed by high temperature mass spectrometry. Evaporation and segregation explained the composition shift in the crystallized fibers. An approach to the investigation of new materials is given. The experimental work reveals and confirms material properties and phase relations. On the other hand, several questions concerning the fiber growth, the materials properties, and phase relations arouse during this work. They are presented in the following chapter.

Chapter 7

Critical review and outlook

This thesis summarizes the outcome of my working time at IKZ Berlin from 2010 to 2013. The prior working title, as mentioned in the exposé, was phrased *growth of Sr_3SiO_5 single crystal fibers with the LHPG method*. It was motivated by laser crystal research by the Institute of Laser-Physics (University of Hamburg, Germany). Studies revealed that tristrontium silicate is not a suitable laser material. Therefore, the focus of my work shifted to the cerium-doped materials calcium scandate and recently strontium yttrium oxide.

A critical parameter affecting each material is the ratio of trivalent and tetravalent cerium. Although the manipulation of this ratio by altering the oxygen fugacitiy of the growth atmosphere was demonstrated, a quantification of this ratio was not performed. A promising way to measure this ratio is X-ray Absorption Near Edge Structure analytics (XANES) or X-ray photoelectron spectroscopy (XPS), as discussed in chapter 5. With melting points above 2100 °C, the thermal analysis and crystal growth is disturbed by evaporation and corrosive degeneration of the tungsten crucibles. The TG signals, which were monitored for all DTA measurements, could not be evaluated because of too high signal-to-noise ratios. For a comprehensive investigation of the phase relations affecting CS2:Ce growth, the ternary system CaO-Sc_2O_3-CeO_x should be examined. If the DTA is measured within tungsten crucibles, also the phase relations CaO-WO_3 should be taken into account. The data that was revealed by thermal analysis inside this work seem to be suitable for thermodynamic assessment of the phase diagram CaO-Sc_2O_3.

Although the fabricated CS2:Ce crystals showed good quality, stimulated emission could not be realized yet. The growth experiments demonstrate one possibility to fabricate CS2:Ce single crystals. For scaling and quality enhancement high-pressure optical floating zone method could be a reasonable choice. Crystallizing in high-pressure atmospheres reduces evaporation. A forced rotation of the seed could prevent the onset of oscillatory states within the melt. The preliminary numerical investigation of a quasi-LHPG setup can be expanded. The relation between composition shift, arising from segregation and evaporation, and presumably oscillating thermocapillary convection has not been investigated yet. For the LHPG apparatus the possibility of reducing the thermal gradient, by installing an afterheater, was considered. Taking the growth experiments of this work into account, the installation of an afterheater does not seem to be reasonable. This apparatus is suitable for growth experiments of high-melting compounds, which are affected by evaporation. The evaporation can be minimized by reducing the fiber radius and rapid growth

rates. Rapid growth rates demand high thermal gradients. The LHPG growth is assumed to be equilibrium-near. The high temperature mass spectrometry measurements monitored effective evaporation that is a kinetic effect. Non-equilibrium calculations could explain the accordance of HTMS results, thermodynamic equilibrium calculation, and LHPG crystallization.

Calcium scandate and strontium yttrium oxide crystallize in $CaFe_2O_4$ structure. For basic research studies, it seems worthwhile to investigate further materials with $CaFe_2O_4$ structure concerning crystal growth and lanthanide doping. Many of these materials have high melting points. Therefore, an approach with fiber crystal growth methods seems reasonable. Moreover, the crystal growth investigation of light phosphors that are currently deployed for LED research could be expanded. Single crystals of these phosphors enable the determination of material properties that cannot be determined from ceramics or powders.

Bibliography

[1] Thermische Analyse TA - DIN 51005:2005-08.

[2] Powder Diffraction Files. *The International Centre for Diffraction Data*, 2011.

[3] FactSage(TM) 6.3, 2012. www.factsage.com.

[4] V. Agafonov, A. Kahn, and D. Michel. Crystal structure of $BaSc_2O_4$; its relation with perovskite. *Mat. Res. Bull.*, 18:975–981, 1983.

[5] M. Alshourbagy. *Development of Single Crystal Fibers for Optics, Scintillation and Mechanical Applications*. PhD thesis, Universitá Di Pisa, 2005.

[6] E.R.M. Andreeta, M.R.B. Andreeta, and A.C. Hernandes. Laser heated pedestal growth of Al_2O_3 / $GdAlO_3$ eutectic fibers. *Journal of Crystal Growth*, 234:782–785, 2002.

[7] M.R.B. Andreeta, E.R.M. Andreeta, A.C. Hernandes, and R.S. Feigelson. Thermal gradient control at the solid-liquid interface in the laser-heated pedestal growth technique. *Journal of Crystal Growth*, 234:759–761, 2002.

[8] D.R. Ardila, M.R.B. Andreeta, S.L. Cuffini, A.C. Hernandes, J.P. Andreeta, and Y.P. Mascarenhas. Single-Crystal $SrTiO_3$ Fibers Grown by Laser Heated Pedestal Growth Method: Influence of Ceramic Feed Rod Preparation in Fiber Quality. *Mat. Res.*, 1(1):11–17, 1998.

[9] P. Atkins and J. Paula. *Atkins' Physical Chemistry*. Oxford University Press, 2002.

[10] R. Atkins and L.D. Diaz. Investigation of host-to-activator energy transfer and surface losses in SrY_2O_4:Eu^{3+} under VUV excitation. *Journal of Luminescence*, 128(9):1463–1470, 2008.

[11] C.W. Bale, P. Chartrand, S.A. Degterov, G. Eriksson, K. Hack, R. Ben Mahfound, J. Melancon, A. D. Pelton, and S. Petersen. FactSage Thermochimical Software and Database. *Calphad*, 2:189–228, 2002.

[12] G. Blasse and Grabmaier B.C. *Luminescent Materials*. Springer-Verlag Berlin Heidelberg New York, 1994.

[13] G. Blasse and A. Bril. Investigation of Some Ce^{3+}-Activated Phosphors. *Chemical Physics*, 378(1966):5139–5145, 1967.

[14] G. Blasse and A. Bril. Luminescence of europium-activated strontium yttrium oxide (SrY_2O_4-Eu). *J. inorg. nucl. Chem.*, 31:1521–1523, 1969.

[15] D.A. Blom. Multislice frozen phonon high angle annular dark-field image simulation study of Mo-V-Nb-Te-O complex oxidation catalyst "M1". *Ultramicroscopy*, 112(1):69–75, 2012.

[16] J. Bohm. *Realstruktur von Kristallen*. E. Schweizerbart'sche Verlagsbuchhandlung Stuttgart, 1995.

[17] G. Boulon. Fifty years of advances in solid-state laser materials. *Optical Materials*, 34:499–512, July 2011.

[18] J.R. Carter and R.S. Feigelson. Preparation and Crystallographic Properties of $A^{2+}B_2^{3+}O_4$ Type Calcium and Strontium Scandates. *Journal of the American Ceramic Society*, 47(1960):141–144, 1964.

[19] J. Chen and Y.-C. Lee. The influence of temperature distribution upon the structure of $LiNbO_3$ crystal rods grown using the LHPG method. *Journal of Crystal Growth*, 208:508–512, 2000.

[20] L. Chen, A. Luo, X. Chen, F. Liu, E. Zhao, Y. Wang, Y. Jiang, Z. Yao, W. Zhang, and S. Chen. Controlled nucleation and crystal growth through nano SiO_2 for enhancing the orange luminescence of $(Sr,Ba)_3SiO_5$: Eu^{2+} in white LEDs application. *Ceramics International*, accepted manuscript, April 2013.

[21] P.-Y. Chen, C.-L. Chang, C.-W. Lan, W.-H. Cheng, and S.-L. Huang. Two-Dimensional Simulations on Heat Transfer and Fluid Flow for Yttrium Aluminium Garnet Single-Crystal Fiber in Laser-Heated Pedestal Growth System. *Japanese Journal of Applied Physics*, 48(11):115504, November 2009.

[22] P.-Y. Chen, C.L. Chang, K.Y. Huang, C.W. Lan, W.H. Cheng, and S.L. Huang. Experiment and simulation on interface shapes of an yttrium aluminium garnet miniature molten zone formed using the laser-heated pedestal growth method for single-crystal fibers. *Journal of Applied Crystallography*, 42(4):553–563, Aug 2009.

[23] Y. Chen, K. Wai Cheah, and M. Gong. Low temperature quenching and high efficiency Tm^{3+}, La^{3+} or Tb^{3+} co-doped $CaSc_2O_4$:Ce^{3+} phosphors for light-emitting diodes. *Journal of Luminescence*, 131(8):1770–1775, August 2011.

[24] W.Y. Ching, Y.-N. Xu, and B. K. Brickeen. Ab-initio calculation of excited state absorption of Cr^{4+} in $Y_{3+}Al_5O_{12}$. *Applied Physics Letters*, 74(25):3755, 1999.

[25] E. Danielson, M. Devenney, D.M. Giaquinta, J.H. Golden, R.C. Haushalter, E.W. McFarland, D.M. Poojary, C.M. Reaves, W.H. Weinberg, and Wu X.D. A Rare-Earth Phosphor Containing One-Dimensional Chains Identified Through Combinatorial Methods. *Science*, 279:837–839, 1998.

[26] L.S. Dent Glasser and F.P. Glasser. Silicates M_3SiO_5. I. Sr_3SiO_5. *Acta Cryst.*, 18:453–454, 1964.

[27] G. Dhanaraj, K. Byrappa, V. Prasad, and M. Dudley, editors. *Springer Handbook of Crystal Growth*. Springer, Heidelberg, 2010.

[28] P. Dorenbos. 5*d*-level energies of Ce^{3+} and the crystalline environment . I. Fluoride compounds. *Phys. Rev. B*, 62:15640–15649, Dec 2000.

[29] P Dorenbos. The $4f^n$-$4f^{n-1}5d$ transitions of the trivalent lanthanides in halogenides and chalcogenides. *Journal of Luminescence*, 91(1-2):91–106, September 2000.

[30] P Dorenbos. The 5d level positions of the trivalent lanthanides in inorganic compounds. *Journal of Luminescence*, 91(3-4):155–176, November 2000.

[31] P. Dorenbos. 5d-level energies of Ce^{3+} and the crystalline environment . IV. Aluminates and "simple" oxides. *Journal of Luminescence*, 99:283–299, 2002.

[32] P. Dorenbos. Systematic behaviour in trivalent lanthanide charge. *Condensed Matter*, 15:8417, 2003.

[33] Y. Du, Z.P. Jin, and P.Y. Huang. Thermodynamic Calculation of the $YO_{1.5}$-CaO System. *Chin. J. Met. Sci. Technol.*, 8:453–456, 1992.

[34] T. Duffar, editor. *Crystal Growth Processes Based on Capillarity*. Wiley and Sons, 2010.

[35] D.J. Ehrlich, P.F. Moulton, and R.M. Jr. Osgood. Ultraviolet solid-state Ce:YLF laser at 325 nm. *Opt. Lett.*, 4(6):184–186, Jun 1979.

[36] D.J. Ehrlich, P.F. Moulton, and R.M. Jr. Osgood. Optically pumped Ce:LaF_3 laser at 286 nm. *Opt. Lett.*, 5(8):339–341, Aug 1980.

[37] J. Eichler and H.J. Eichler. *Laser*. Springer Berlin Heidelberg, 2003.

[38] K. Eickhoff and K. Gürs. Tiegelfreies Zonenschmelzen von Rubinkristallen durch Aufheizen der Schmelzzone mittels Laser. *Journal of Crystal Growth*, 6(1):21–25, December 1969.

[39] M. Fechner. *Seltenerd-dotierte Oxidkristalle für Festkörperlaser im sichtbaren Spektralbereich*. PhD thesis, Universität Hamburg, 2011.

[40] R. S. Feigelson. Pulling optical fibers. *Journal of Crystal Growth*, 79:669–680, 1986.

[41] R.S. Feigelson. Opportunities for Research on Single-crystal Fibers. *Mat. Sci. Eng. B*, 1:67, 1988.

[42] M.M. Fejer, J.L. Nightingale, G. Magel, and R.L. Byer. Laser-heated miniature pedestal growth apparatus for single-crystal optical fibers. *Review of Scientific Instruments*, 55(11):1791, 1984.

[43] M. Ferriol, Y. Terada, T. Fukuda, and G. Boulon. Laser heated pedestal growth and characterization of zinc lithium niobate crystals. *Journal of Crystal Growth*, 197(1-2):221–227, February 1999.

[44] J.M. Fields, P.S. Dear, and J.J. Brown. Phase Equilibria in the System BaO-SrO-SiO_2. *Journal of the American Ceramic Society*, 55:585–588, 1972.

[45] L. Fornasiero, E. Mix, V. Peters, K. Petermann, and G. Huber. New Oxide Crystals for Solid State Lasers. *Cryst. Res. Technol.*, 34:255–260, 1999.

[46] T. Fukuda and V.I. Chani, editors. *Shaped crystals*. Springer, 2009.

[47] T. Fukuda, P. Rudolph, and S. Uda, editors. *Fiber crystal growth from the melt*. Springer Berlin Heidelberg, 2004.

[48] P. Gabbott, editor. *Thermal Analysis*. Blackwell Publishing, 2008.

[49] S. Ganschow, D. Klimm, and R. Bertram. On the effect of oxygen partial pressure on the chromium distribution coefficient in melt-grown ruby crystals. *Journal of Crystal Growth*, 325(1):81–84, June 2011.

[50] R. Gaume. Spectroscopic properties of Yb-doped scandium based compounds Yb:$CaSc_2O_4$, Yb:$SrSc_2O_4$ and Yb:Sc_2SiO_5. *Optical Materials*, 22(2):107–115, April 2003.

[51] O.I. Get'man, V.V. Panichkina, and Z.P. Rud'. Effect of the Phase Composition of Barium-Calcium Alumoscandates on the Emission Properties of Impregnated Cathodes. *Powder Metallurgy and Metal Ceramics*, 39(11):584–589, 2000.

[52] F. Goubin, X. Rocquefelte, M. Whangbo, Y. Montardi, and R. Brec. Experimental and Theoretical Characterization of the Optical Properties of CeO_2, $SrCeO_3$, and Sr_2CeO_4 Containing Ce^{4+} (f^0) Ions. *Chem. Mater.*, 16(4):662–669, 2004.

[53] W. Gruner. Determination of oxygen in oxides by carrier gas hot extraction analysis with simultaneous CO_x detection. *Fresenius' Journal of Analytical Chemistry*, 365:597–603, 1999.

[54] W. Gruner and A. John. Determination of oxygen in solids using a modified carrier gas-hot extraction method. *Fresenius' Journal of Analytical Chemistry*, 342(1-2):51–53, 1992.

[55] C. Guguschev. *In situ Untersuchungen von Kristallwachstums- und Reinigungsprozessen im System Al-N-O-C-H*. PhD thesis, Technische Universität Berlin, 2012.

[56] D.S. Hamilton, S.K. Gayen, G.J. Pogatshnik, R.D. Ghen, and W.J. Miniscalco. Optical-absorption and photoionization measurements from the excited states of Ce^{3+}:$Y_3Al_5O_{12}$. *Phys. Rev. B*, 39:8807–8815, May 1989.

[57] Z. Hao, J. Zhang, X. Zhang, S. Lu, and X. Wang. Blue-Green-Emitting Phosphor $CaSc_2O_4$:Tb^{3+}: Tunable Luminescence Manipulated by Cross-Relaxation. *Journal of The Electrochemical Society*, 156(3):H193, 2009.

[58] W. Hempel. *Struktureigenschaftsbeziehungen in Erdalkalisilikat basierenden Leuchtstoffen*. PhD thesis, Universität Augsburg, 2007.

[59] B. Henderson and R.H. Bartram. *Crystal-field engineering of solid-state laser materials*. Cambridge University Press, 2000.

[60] B. Henderson and G.F. Imbusch. *Optical spectroscopy of inorganic solids*. Oxford University Press, 1989.

[61] G. Höhne, W. Hemminger, and H.-J. Flammersheim. *Differential scanning calorimetry*. Springer-Verlag Berlin Heidelberg New York, 2003.

[62] J. Hölsa, A. Kotlov, T. Laamanen, M. Lastusaari, M. Lindstöm, and M. Malkamäki. Yellow Persistent Luminescence of the Sr_3SiO_5:Eu^{2+},R^{3+} Materials. *HASYLAB annual report*, 20111914, 2011.

[63] M.E. Huntelaar, H.P. Cordfunke, and A. Scheele. Phase relations in the SrO-SiO_2-ZrO_2 system I. The system SrO-SiO_2. *Journal of Alloys and Compounds*, 191:87–90, 1993.

[64] S. Ishibashi. Cr, Ca :$Y_3Al_5O_{12}$ laser crystal grown by the laser-heated pedestal growth method. *Journal of Crystal Growth*, 183(4):614–621, February 1998.

[65] H.S. Jang and D.Y. Jeon. Yellow-emitting Sr_3SiO_5:Ce^{3+},Li^+ phosphor for white-light-emitting diodes and yellow-light-emitting diodes. *Applied Physics Letters*, 90(4):041906, 2007.

[66] H.S. Jang, H. Yang, S.W. Kim, J.Y. Han, S.-G. Lee, and D.Y. Jeon. White Light-Emitting Diodes with Excellent Color Rendering Based on Organically Capped CdSe Quantum Dots and Sr_3SiO_5:Ce^{3+} ,Li^+ Phosphors. *Advanced Materials*, 20:2696–2702, 2008.

[67] W. Jia, H. Yuan, L. Lu, H. Liu, and W.M. Yen. Crystal growth and characterization of Eu^{2+}, Dy^{3+} :$SrAl_2O_4$ and Eu^{2+}, Nd^{3+}:$CaAl_2O_4$ by the LHPG method. *Journal of Crystal Growth*, 200:179–184, 1999.

[68] Z. Jin and Y. Du. Thermodynamic calculation of the ZrO_2-$YO_{1.5}$-CaO phase diagram. *Calphad*, 16(4):355–362, 1992.

[69] M. Jurisch and W. Loeser. Analysis of periodic non-rotational W striations in Mo single crystals due to nonsteady thermocapillary convection. *Journal of Crystal Growth*, 102(1-2):214–222, April 1990.

[70] A.A. Kaminskii. Modern developments in the physics of crystalline laser materials. *Physica Status Solidi (a)*, 200(2):215–296, December 2003.

[71] K.M. Kim, A.B. Dreeben, and A. Schujko. Maximum stable zone length in float-zone growth of small-diameter sapphire and silicon crystals. *J. Appl. Phys.*, 50:4472, 1979.

[72] S.S. Kim. Thermodynamic modeling of the Sc_2O_3-MgO phase diagram. *Journal of Alloys and Compounds*, 488:479–481, 2009.

[73] P.L. King, T.-K. Sham, R.A. Gordon, and M.D. Dyar. Microbeam X-ray analysis of Ce^{3+}/Ce^{4+} in Ti-rich minerals : A case study with titanite (sphene) with implications for multivalent trace element substitution in minerals. *American Mineralogist*, 98(2000):110–119, 2013.

[74] W. Kleber, H.J. Bautsch, and J. Bohm. *Einfuerung in die Kristallographie*. Verlag Technik Berlin, 1998.

[75] D. Klimm, S. Ganschow, D. Schulz, R. Bertram, R. Uecker, P. Reiche, and R. Fornari. Growth of Oxide Compounds under Dynamic Atmosphere Composition. *J. Crystal Growth*, 311:534–536, 2009.

[76] L.M. Kobva, L.N. Lykova, M.V. Paramova, and T.A. Kalinina. . *Dokl. Akad. Nauk SSSR*, 260:924–927, 1981.

[77] F.A. Kroeger and J. Bakker. Luminescence of cerium compounds. *Physica*, 8(7):628–646, 1941.

[78] F.A. Kroeger and H.J. Vink. Relations between the Concentrations of Imperfections in Crystalline Solids. *Solid State Physics*, 3:307–435, 1956.

[79] K. Kurosaki, T. Tanaka, T. Maekawa, and S. Yamanaka. Thermophysical properties of SrY_2O_4. *Journal of Alloys and Compounds*, 398(1-2):304–308, August 2005.

[80] W. Kweestroo, H.A.M. van Hal, and C. Langereis. Compounds in the system BaO-Sc_2O_3. *Mat. Res. Bull.*, 9:1623–1630, 1974.

[81] W. Kwestroo, C. Langereis, and H. Nabben. Alkaline Earth Scandates. *Mat. Res. Bull.*, 17:641–646, 1982.

[82] C. Lan. Radial dopant segregation in zero-gravity floating-zone crystal growth. *Journal of Crystal Growth*, 132(3-4):578–591, September 1993.

[83] H. Li, S. Zhang, S. Zhou, and X. Cao. Chemical bond characteristics, thermal expansion property and compressibility of AR_2O_4 (A = Ca,Sr,Ba; R= rare earths). *Materials Chemistry and Physics*, 114(1):451–455, 2009.

[84] C.H. Liebscher, J. Preussner, R. Voelkl, and U. Glatzel. Atomic site location by channelling enhanced microanalysis (ALCHEMI) in γ-strengthened Ni- and Pt-base alloys. *Acta Materialia*, 56(16):4267–4276, September 2008.

[85] H. Luo, J. Liu, X. Zheng, L. Han, K. Ren, and X. Yu. Enhanced photoluminescence of Sr_3SiO_5:Ce^{3+} and tuneable yellow emission of Sr_3SiO_5:Ce^{3+}, Eu^{2+} by Al^{3+} charge compensation for W-LEDs. *Journal of Materials Chemistry*, 22(31):15887–15893, 2012.

[86] D. Maier. *Segregation effects in single-crystal fibers grown by the micro-pulling-down method*. PhD thesis, Humboldt-Universiät zu Berlin, 2009.

[87] V. Manivannan. Nature of luminescent centers in Cerium-activated materials with the $CaFe_2O_4$ structure. *Journal of Luminescence*, 102-103:635–637, May 2003.

[88] M. Mansmann. Die Kristallstruktur von Tribariumpentaoxometallaten(IV) und isotyper Verbindungen. *Zeitschrift für anorganische und allgemeine Chemie*, 339(lV):52–56, 1965.

[89] H. Manuspiya. *Electrical Properties of Niobium Based Oxides - Ceramics and Single Crystal Fibers grown by the Laser-Heated Pedestal Growth (LHPG) Technique*. PhD thesis, The Pennsilvania State University, 2003.

[90] T. Miyoshi, S. Masui, T. Okada, T. Yanamoto, T. Kozaki, S. Nagahama, and T. Mukai. 510-515 nm InGaN-Based Green Laser Diodes on c-Plane GaN Substrate. *Applied Physics Express*, 2:062201, May 2009.

[91] H. Müller-Buschbaum. Zur Kenntnis von SrY_2O_4. *Zeitschrift für anorganische und allgemeine Chemie*, 358:138–146, 1968.

[92] H. Müller-Buschbaum. The crystal chemistry of AM_2O_4 oxometallates. *Journal of Alloys and Compounds*, 349(1-2):49–104, February 2003.

[93] H. Müller-Buschbaum and H.G. Schnering. Über Oxoscandate I — Zur Kenntnis des $CaSc_2O_4$. *Zeitschrift für anorganische und allgemeine Chemie*, 336(1963):295–305, 1965.

[94] S. Nakamura, T. Mukai, and M. Senoh. High-Power GaN P-N Junction Blue-Light-Emitting Diodes. *Japanese Journal of Applied Physics*, 30:1998–2001, 1991.

[95] M. Okrusch. *Mineralogie - Eine Einführung in die spezielle Mineralogie, Petrologie und Lagerstättenkunde*. Springer Berlin Heidelberg, 2005.

[96] M.P. Oxley and L.J. Allen. ICSC: a program for calculating inelastic scattering cross sections for fast electrons incident on crystals. *Journal of Applied Crystallography*, 36(3):940–943, May 2003.

[97] J.K. Park, C.H. Kim, S.H. Park, H.D. Park, and S.Y. Choi. Application of strontium silicate yellow phosphor for white light-emitting diodes. *Applied Physics Letters*, 84:1647, 2004.

[98] A.D. Pelton. *Thermodynamics and Phase Diagrams of Materials*, chapter 1, pages 1–80. Wiley-VCH Verlag GmbH & Co. KGaA, 2005.

[99] W. G. Pfann. Principles of zone-melting. *J. Met. Trans. AIME*, 4:747, 1952.

[100] W. G. Pfann. *Zone melting*. Wiley, New York, 1958.

[101] J. Philippen, C. Guguschev, R. Bertram, and D. Klimm. Laser-heated pedestal growth of cerium doped calcium scandate crystal fibers. *Journal of Crystal Growth*, 363:270–276, 2013.

[102] J.M. Porras-Vázquez, E.R. Losilla, L. León-Reina, M. Martínez-Lara, and M.A.G. Aranda. Synthesis and Characterization of a New Family of Mixed Oxide-Proton Conductors Based on Tristrontium Oxysilicate. *Chemistry of Materials*, 20(5):2026–2034, March 2008.

[103] V.V. Prokofiev, J.P. Andreeta, C.J. Lima, M.R.B. Andreeta, A.C. Hernandes, J.F. Carvalho, A.A. Kamshilin, and T. Jaaskelainen. The influence of temperature gradients on structural perfection of single-crystal sillenite fibers grown by the LHPG method. *Opt. Mater.*, 4(March):521–527, 1995.

[104] M.N. Rahaman. *Ceramic Processing*. CRC Press, 2006.

[105] P. Rudolph. *Profilzüchtung von Einkristallen*. Akademie-Verlag Berlin, 1982.

[106] C. Schmidt, M. Rittmeier-Kettner, H. Becker, J. Ellert, R. Krombach, and G.M. Scheneider. Differential thermal analysis (DTA) and differential scanning calorimetry (DSC) at high pressures. Experimental techniques and selected results. *Thermochimica Acta*, 238:321–336, 1994.

[107] D. Schwabe. Some evidence for the existence and magnitude of a critical marangoni number for the onset of oscillatory flow in crystal growth melts. *Journal of Crystal Growth*, 46(1):125–131, January 1979.

[108] D. Schwabe. Marangoni instabilities in small circular containers under microgravity. *Experiments in Fluids*, 40(6):942–950, March 2006.

[109] A.A. Setlur. Phosphors for LED-based Solid-State Lighting. *The Electrochemical Society (Interface)*, 18:32–36, Winter 2009.

[110] R.D. Shannon. Revised Effective Ionic Radii and Systematic Studies of Interatomie Distances in Halides and Chaleogenides. *Acta Cryst.*, A32:751, 1976.

[111] J.H. Sharp, T.P.J. Han, B. Henderson, R. Illingworth, and I.S. Ruddock. Dopant incorporation in single-crystal fibre growth by the laser-heated miniature pedestal growth technique. *Journal of Crystal Growth*, 131:457–464, 1993.

[112] G.M. Sheldrick. A short history of SHELX. *Acta Cryst.*, A64:112–122, 2008.

[113] Y. Shimomura, T. Kurushima, and N. Kijima. Photoluminescence and Crystal Structure of Green-Emitting Phosphor $CaSc_2O_4$:Ce^{3+}. *Journal of The Electrochemical Society*, 154(8):J234, 2007.

[114] P.J. Spencer. A brief history of CALPHAD. *Calphad*, 32(1):1–8, March 2008.

[115] L. Spiess, G. Teichert, H. Behnken, C. Genzel, and R. Schwarzer. *Moderne Röntgenbeugung: Röntgendiffraktometrie für Materialwissenschaftler, Physiker und Chemiker*. Vieweg Teubner Verlag Wiesbaden, 2009.

[116] D.Y. Tang, R.K. Route, and R.S. FEIGELSON. Growth of Barium Metaborate (BaB_2O_4) Single Crystal Fibers by the Laser-Heated Pedestal Growth Method. *J. Crystal Growth*, 91:81–89, 1988.

[117] Agilent Technologies. CrysAlis PRO. *Agilent Technologies, Yarnton, England*, 2012.

[118] S.G. Tresvyatskii, L.M. Lopato, A.E. Kushchevskii, and A.V. Shevchenko. . *Izv. Akad. Nauk SSSR, Neorg. Mater.*, 10:1808–1811, 1971.

[119] S. Uda and W.A. Tiller. The influence of an interface electric field on the distribution coefficient of chromium in $LiNbO_3$. *J.Crystal Growth*, 121(1-2):93–110, June 1992.

[120] L. van Pieterson, S. Soverna, and A. Meijerink. On the Nature of the Luminescence of Sr_2CeO_4. *Journal of The Electrochemical Society*, 147:4688, 2000.

[121] K.-T. Wilke and J. Bohm. *Kristallzüchtung*. Verlag Harri Deutsch Thun Frankfurt/Main, 1988.

[122] D.B. Williams and C.B. Carter. *Transmission electon microscopy IV - Spectrometry*. Plenum Press, New York, 1996.

[123] D.-H. Yoon and T. Fukuda. Characterization of $LiNbO_3$ micro single crystals grown by the micro-pulling-down method. *Journal of Crystal Growth*, 144:201–206, 1994.

[124] L. Zhou, J. Shi, and M. Gong. Red phosphor SrY_2O_4:Eu^{3+} synthesized by the sol-gel method. *Journal of Luminescence*, 113:285–290, 2005.

[125] Liya Zhou, Jianxin Shi, and Menglian Gong. Preparation SrR_2O_4:Eu^{3+} (R=Y, Lu) phosphor and its photoluminescence properties. *Materials Letters*, 59(16):2079–2084, July 2005.

List of Figures

List of Tables

Acknowledgement

A multitude of people supported me on my way to finish this thesis. My gratitude to my friends, my family, and Sarina for their ongoing support and sympathy.

I am extraordinary grateful for the help I got from my supervisor Dr. Detlef Klimm, who spent plenty of hours on advices, discussions, corrections, and introduction into thermal analysis and thermodynamic calculation. In the same way, I want to express my gratitude to Dr. Martin Lerch, who supported me to finish and submit my thesis at Technische Universität Berlin. Dr. Reinhard Uecker provided a pleasant and diversified working environment within the group oxides/fluorides at the IKZ. All members of the this group supported me in the last years. Dr. Christo Guguschev introduced HTMS measurements to me and, beyond that, supported me as an excellent climbing mate. Dr. Rainer Bertram did ICP-OES elemental analysis. Dr. Zbigniew Galazka introduced tristrontium silicate growth. Steffen Ganschow explained mPD growth. Andreas Tauchert introduced LHPG growth to me. Elvira Thiede, Isabelle-Mercedes Schulze Jonack, and Martina Rabe supported me in preparation and laboratory work of all kinds.

I want to express my gratitude to my further colleagues at IKZ: Toni Markurt did TEM analysis. Dr. Martin Albrecht introduced and performed SEM. Dr. Uta Juda, Manuela Imming, and Kerstin Banse supported me in crystal machining. Dr. Klaus Irmscher, Martin Naumann and Mike Pietsch supported me in optical spectroscopy. Albert Kwasniewski performed XRD and HR-XRD. Dr. Wolfram Miller elaborated numerical investigation of the LHPG melt zone.

Furthermore, Matthias Kage executed cold extrusion of ceramic feed rods. Dr. Dieter Rhede performed EMPA analysis. Dr. Matthias Fechner did laser experiments and pioneered my work with his thesis on oxide laser materials. Dr. Klaus Petermann encouraged the investigation of cerium doped calcium scandate. Daniel Marzahl and Philip Metz performed laser experiments. Paula Nixdorf did single crystal XRD and Dr. Elisabeth Irran performed single crystal structure refinement. Dr. Saurenz performed CGHE.

I will always remember my scientific exchange at Instituto de Pesquisas Energéticas e Nucleares São Paulo. My thanks to Dr. Sonia Baldochi, who enabled this opportunity to me and to Dr. Laércio Gomes, who did optical spectroscopy. I got crucial advices from Dr. Dietrich Schwabe concerning fluid mechanics and from Dr. Robert Feigelson concerning LHPG growth. Nicolai Nagler and Rita Labonté-Philippen proof-read my thesis. I want to express my special thanks to all of them.